LRP 689/01 January 2001

Segregated Copper Ratio Experiment On Transient Stability (SeCRETS) Final Report

P. Bruzzone, Editor

EU Task M29
ITER Task N11TT03

ISSN 0458-5895

CENTRE DE RECHERCHES EN PHYSIQUE DES PLASMAS
ASSOCIATION EURATOM - CONFÉDÉRATION SUISSE
CRPP - Technologie de la Fusion, CH - 5232 Villigen PSI

ÉCOLE POLYTECHNIQUE
FÉDÉRALE DE LAUSANNE

*Se*gregated *C*opper *R*atio *E*xperiment on *T*ransient *S*tability

(SeCRETS)

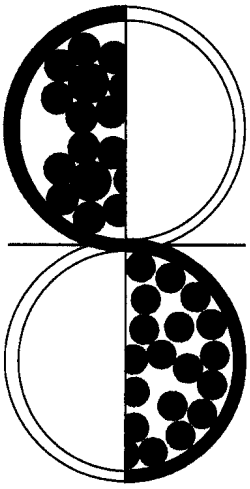

EU Task M29
ITER Task N11TT03

Final Report

December 2000

Table of content

Executive Summary

Two Nb_3Sn, steel jacketed, cable-in-conduit conductors have been manufactured with identical non-Cu cross sections and the stabilizer either included in the Nb_3Sn composite or partly segregated as copper wires. The two conductors are series connected and wound as a bifilar, single layer solenoid, assembled in the high field bore (11 T) of the SULTAN test facility. The operating current is up to 12 kA (400 A/mm^2). A transverse pulsed field is applied with ΔB up to 2.7 T, field rate up to 180 T/s and field integral up to 530 T^2/s.

In the dc test, a good agreement is found between the I_c and the T_{cs} results, both correctly scaling according to the parameters derived from the strand tests. The n-value from the V-I curve is in the range of 15. The current sharing at the high field section is correlated with a local current re-distribution, observed by arrays of miniature Hall sensors, detecting the self-field around the conductor.

The ac losses results in the range of 2 to 9 Hz by gas flow calorimetry indicate coupling currents constant, $n\tau$, in the range of 1.5 ms at high field, increasing by a factor of 2 with 12 kA transport current. Loss extrapolation to 0 frequency suggests that the loss curve may be not linear outside the test range, with higher $n\tau$ at lower field rate. The calorimetric loss estimation at the fast field transient (f = 15 Hz) indicates $n\tau \approx 2$ ms.

The ITER plasma disruption transients have been reproduced by the pulsed coils. Due to the very low ac losses, no quench could be generated in either conductor even reducing the temperature margin below 0.2-0.3 K.

Very large field transients, with integral above 100 T^2/s, are required to quench the conductors. In that range, the conductor without segregated copper has superior performance. Due to the large interstrand resistance (very low ac losses), the segregated copper has marginal contribution to the stability. No evidence of current re-distribution is observed during the field transients.

No inflection due to the limiting current (calculated at h = 1000 W/Km^2) is observed for either conductor in the stability curve as a function of the operating current, with dm/dt = 3.5 g/s. Computer simulations confirm that the limiting current is substantially higher than predicted.

The stability, i.e. the ability to withstand large transverse field integral with 65 ms time scale, increases linearly with the mass flow rate for both conductors, in the investigated range of coolant speed, 0.3 - 1.3 m/s. No evidence of induced flow is observed.

The temperature margin to be allocated for the ITER field transients (plasma disruption) is marginal, < 0.2 K, both with and without segregated copper. The amount of copper to be included in the strand cross section for ITER stability is by far smaller than predicted by the "limiting current" criterion with h = 1000 W/Km^2. To make effective the segregated copper for transient stability, a lower interstrand resistance is desirable, what can be safely tolerated for the transient field ac losses.

A. Introduction, Scope and Timescale of the Task

Plasma disruption and temperature margin

In the ITER design criteria, a temperature margin of 2 K on top of the highest operating temperature is originally selected for the conductor design. From the temperature margin, the energy margin per cubic centimeter of strand is derived according to the void fraction and the specific heat of Helium. The disturbance energy in the worst case of operating conditions must be smaller than the energy margin.

The most important source of disturbance which raises the strand temperature above the coolant temperature is the transient transversal field change during plasma disruption (other events which may raise the coolant temperature together with the strands are outside the scope of stability). The time scale of the field transient at the conductor is of the order of few hundreds milliseconds. The amount of energy (ac losses) deposited in the cable is predicted to be low, but the energy from the coupling loss is dissipated non homogeneously across the cable cross section, with larger power density at selected strand crossovers. Moreover, the interstrand coupling currents alter the current distribution and may cause substantial current sharing and partial saturation at high field, turning into additional loss.

Few experimental data are available for the behavior of cable-in-conduit conductors under relevant operating parameters (high background field, very fast transverse field transient, relevant conductor size and length, high DC current density, forced flow of supercritical Helium). To cover the incertitude on the overall loss and stability behavior under plasma disruption, a very conservative value of the disturbance energy is assumed.

A major aim of the SeCRETS task is to investigate experimentally, under relevant operating conditions, the minimum temperature margin necessary to withstand a transverse field transient simulating an ITER plasma disruption.

Copper segregation and Nb_3Sn conductor cost

In the transient stability models, the transport current switches from the superconducting to the stabilizer cross section as soon as the superconductor temperature exceeds the current sharing temperature, T_{cs}. Most models assume that only the copper included in the cross section of the superconducting composite can be accounted as stabilizer. This assumption, together with homogeneous current distribution boundary, provides a formidable simplification of the stability analysis, as the cable stability is assessed at the level of an individual strand. Solving the balance of generated-to-removed power (e.g. setting the Steckly parameter to 1), the designer finds immediately the required copper ratio in the composite.

It's qualitatively clear that the copper placed outside the superconducting composite ("segregated copper" in cable-in-conduit conductors) contributes less effectively to the transient current transfer, mostly in the case of high interstrand resistance. Any designer could conclude that it is "preferable" to place all the stabilizer straight in the composite and not account the segregated copper for stability.

On the other hand, interstrand current sharing effectively occurs in the CICC, despite the high interstrand resistance, e.g. to re-distribute the current from the joint to high field. It is then reasonable to investigate how far the segregated copper contributes to stability.

The issue of the stabilizing Cu distribution has a very large cost impact in the ITER conductors, where the cost of the Nb_3Sn strand is independent on the Cu:non-Cu ratio. Originally, in the TF strand, the Cu:non-Cu ratio is 1.75, and in most of the CS is 2. If segregation of copper is allowed by adding Cu wires in the strand bundle, e.g. reducing the Cu:non-Cu ratio in the strand down to 1 (what would be welcome for manufacturing reasons by all the strand suppliers), the overall amount of strand would drop by 1/3, maintaining the same non-Cu cross section, with a cost saving in the range of 300 M$ and a more realistic procurement schedule.

A major aim of the SeCRETS task is to investigate by straight comparison how far the segregated copper in a Nb_3Sn cable-in-conduit conductor contributes to the stability, under relevant operating conditions(simulation of plasma disruption), as well as under very fast field transients.

The SeCRETS task

Two Nb_3Sn CICC, ø = 14.5 mm, are prepared with identical overall cross sections but different location of the copper stabilizer: either fully included in the composite cross section or partly segregated as copper wires. Two conductor sections, each about 13 m long, are series connected and wound as a bifilar, single layer solenoid on a ø = 400 mm cylinder. A set of pulsed coils is attached to the winding to provide a transverse field.

After heat treatment, the instrumented winding is inserted in the high field bore of the SULTAN facility, with dc background field up to 11.3 T. The dc current in the winding sample is up to 12 kA (400 A/mm^2 non-Cu). The temperature and mass flow rate of supercritical Helium can be adjusted independently in the two conductors, in the range of 4.5 to 10 K and 1.5 to 10 g/s. The superimposed, transverse pulsed field has amplitudes up to 2.7 T and field rate up to 180 T/s.

The test program includes

- extended dc measurements of both conductors (I_c vs. B and T, T_{cs} vs. B and I), in two different operating load conditions
- calorimetric ac losses of both conductors under steady state sinus sweep, as a function of the background field and operating current
- transient stability of both conductors as a function of the temperature margin, mass flow rate, operating current density and transient duration (32 and 65 ms)
- stability for simulated plasma disruption transients as a function of the temperature margin
- current distribution measurements by arrays of Hall sensors at 6 selected locations during dc and transient operation

The ability to withstand plasma disruption is assessed comparatively for the two conductors, in order to qualify the use of segregated copper in the ITER conductors. The stability curve for fast field transients is compared with the analytical models to quantify the contribution of segregated copper to the current sharing process.

The ac losses, current distribution and dc results provide the required boundary conditions for the interpretation of the stability results. Moreover, conclusions are drawn on the scaling of strand-to-cable performance, interstrand current sharing, coupling loss in operation and heat transfer coefficient.

Time scale of the SeCRETS task

The task proposal was approved by the EURATOM Fusion Technology in May 1998 and filed as EU Task M29 (ITER Task N11TT03). A summary of the major steps is gathered in the chart below.

During the initial phase of the task, several contracts have been placed by CRPP with industrial and university partners, including the Nb_3Sn conductor procurement (VNIINM, Moscow, RF), the winding manufacture (OSWALD, Miltenberg, D), the heat treatment (Ansaldo, Genova, I), the pulsed field coils (University of Twente, Enschede, NL) and the bipolar power supply for the pulsed coils (EEI, Vicenza, I). All the contractors fulfilled their duty on schedule.

Compared to the original plan, the task has been completed with a delay of about six months, partly due the availability of the SULTAN facility. On request of the NET Team, the facility was held back in the short sample testing mode (July-September 1999) to complete the test program of the European Joint samples.

Two months delay (February-March 2000) are due to the need to warm-up SULTAN, after the initial cool-down, to modify the path of the cooling circuit for the current leads.

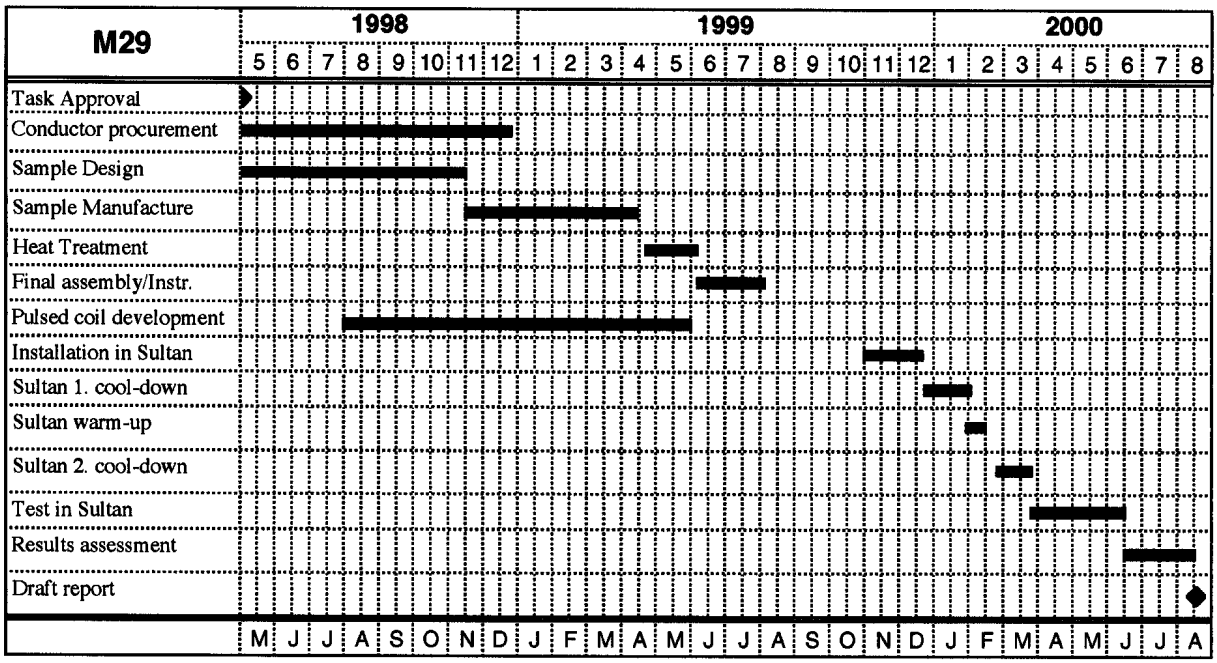

B. Sample Description

B.1 Conductor Layout and Procurement

The layout of the two cable-in-conductors to be used in the experiment is driven by a number of boundary conditions. The radius of the winding limits the size of the conductors. The SULTAN bore has a free diameter of 577 mm, but a generous gap had to be allocated for the pulsed field coils (see section B.3) protruding from the winding. This led to a winding diameter of 400 mm and hence to a maximum conductor diameter in the range of 15 mm to avoid crinkling at bending.

The Nb_3Sn strand coating (2.5 μm electroplated Cr) and the void fraction (37%) are maintained identical to the ITER design. On the other hand, the internal cable wraps and the central hole have been omitted because they are not significant to the object of the experiment. To speed up the procurement, as well as to reduce the cost and risk of the manufacture, the jacket material is stainless steel, AISI 316L.

The conductor without segregated copper (conductor A) uses the same strand developed for the Model Coils, for reasons of relevance and economy too (spare amounts of strand were available at reduced cost from all the strand suppliers in 1997). The conductor A is a typical ITER, high grade, last but one cable stage, with all the stabilizing copper included in the superconducting strand cross section, Cu:non-Cu = 1.5. The cable pattern is 3x3x4x4, compared to 3x4x4x4 in CS1 and 3x3x4x5 in CS2 and TFMC conductors.

The layout of the conductor with segregated copper (conductor B) is driven by the requirement to have the same overall Cu and non-Cu cross sections as in conductor A. The Cu:non-Cu ratio in the superconducting strands is reduced down to 1, but the strand diameter, 0.82 mm, is almost identical to conductor A (0.81 mm). The first cable stage of conductor B consists of a ring of 7 strands around a 1.1 mm diameter copper core. The number of cable stages is three instead of four, see Fig.1. The first cable stage of conductor B has the same overall cross sections as the second stage of conductor A. The design aimed to obtain the same critical current for the two conductors, to be connected in series and exposed to the same background and pulsed field. The amount of segregated

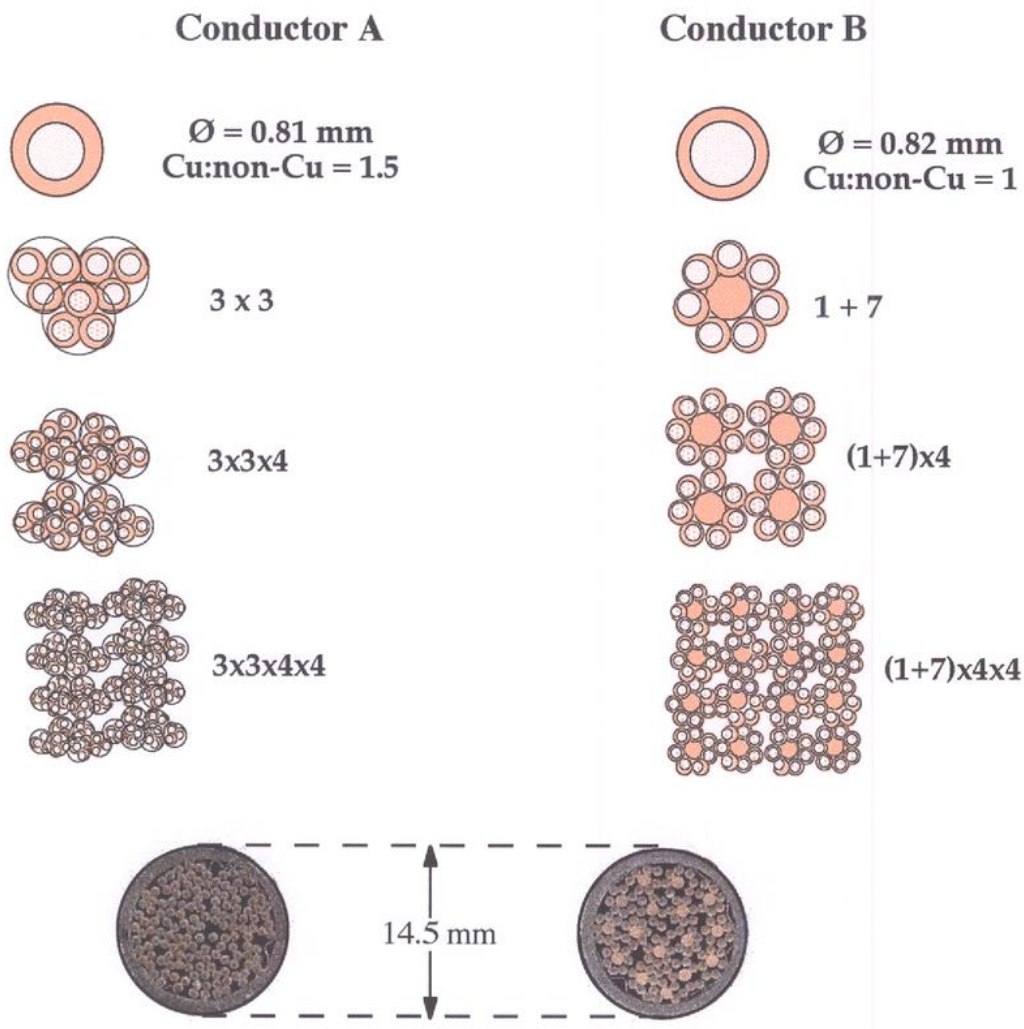

Figure 1. Layout of conductors A and B, with segregated copper. The first cable stage of conductor B has the same cross sections as the second stage of conductor A

copper in conductor B is selected large enough to offer a significant cost advantage, but the Cu:non-Cu in the superconducting strand is still close enough to the original value and no major manufacturing process modifications are required.

An international call for tender was sent to the major companies involved world-wide in the manufacture of superconductors for the ITER Model Coils. Only three companies bid for the jacketed conductors. Two more companies offered the cables without jacket. The procurement contract was awarded in May 98 to the best bidder, VNIINM (Bochvar Institute, Moscow), with a delivery time of 7-8 months.

VNIINM used for conductor A the standard ITER strand, from the same production batches as for the CSMC-TF insert, qualified in the ITER strand bench mark action. For conductor B, a new production was started, using the same matrix-filament-barrier layout as for the ITER strand, in order to achieve the same J_c.

The Cr plating of the superconducting and copper wires was done by VNIIKP (as subcontractor of VNIINM), with the same process used for the ITER strand and qualified in the ITER Cr vendor comparison action. Cabling and jacketing was also done by VNIIKP as subcontractor of VNIINM. A pre-production using copper wires was used to qualify the processes. A thin steel foil is wrapped around the final cable to protect it during the pull-through. For jacketing, the same site of the ITER long length jacketing was used. The steel pipes are seamless section, 6 m long, produced by SANDVIK (Sweden). For the dummy conductor, the pipe material is 304L, for the superconductors, 316L. The steel pipes have 16 mm diameter and are butt welded to a straight section, over 50 m long and compacted, after insertion of the cable, down to the diameter of 14.5 mm.

The production was completed on schedule and the conductor sections delivered to CRPP-Villigen in the first week of January 99. The supply includes two sections of conductors (A and B), each 51 m long, wound on a 2 m diameter, wooden drum. At this diameter, no significant ovalization is measured on the conductors. However, after bending under tension to 200 mm radius, the conductor size in radial direction is reduced by about 0.15 mm.

Six additional straight conductor sections, each 2 m long (3 x A and 3 x B) are delivered for preparation of AC loss and $I_c(\varepsilon)$ specimens, see section C.1. Strand sections are also included for I_c specimens, used as heat treatment witness samples. The main actual conductor data, as measured on specimens of the delivered sections, are gathered in Table 1. The void fraction measured at UT is slightly higher than predicted by the cable geometry. The conductor sections fulfil the specifications. For the superconducting performance, see section C1.

Table 1. Conductor Data

	Conductor A	Conductor B
Strand type	Nb_3Sn	
Strand surface	Cr coating, 2.5 – 2.9 μm	
Strand diameter	0.810 – 0.813 mm	0.818 – 0.820 mm
Cable configuration	3 x 3 x 4 x 4	(1+7) x 4 x 4
N of superconducting strands	144	112
N of Cu cores	Ø	16
Cu-core diameter	-	1.1 mm
Cu:non-Cu in superconducting strands	1.45 – 1.54	1.02
Non-Cu cross section (non-twisted)	29.68 mm^2	29.57 mm^2
Cu Cross section (non-twisted)	44.52 mm^2	44.77 mm^2 (34% segregated)
Overall wet perimeter	0.366 m	0.343 m
Nb_3Sn strand perimeter	0.366 m	0.288 m
Nb_3Sn strand weight per meter cable	0.66 kg/m	0.52 kg/m
Twist pitches, right hand, mm	10, 51, 76, 136, 167	10, 66, 122,160
Steel wrapping	25 x 0.065 mm	
Steel wrapping pitch	≈ 14 mm	
Jacket wall thickness (after compaction)	1.01 ± 0.02 mm	
Jacket material	316 L	
Conductor diameter	14.54 ± 0.03	
Void fraction	35.5%	36.1 %
Cable space diameter	12.54 ± 0.03 mm	

B.2 Winding Layout and Manufacture

The winding consists of two conductor sections connected at one end into a hairpin joint and wound into a spaced, bifilar, one layer solenoid. The conceptual layout of the winding is sketched in Fig. 2.

The contract for the conductor winding has been negotiated with the company OSWALD (Miltenberg, Germany). The scope of the contract, awarded in September 98, includes the detailed design and manufacture of the coil former and related components, the insulation and winding to the final size.

The coil former consists of an inner, 2 m long 316 L steel cylinder (i.d. = 325 mm, o.d. = 350 mm). Two steel cylinders, 600 mm long, with outer diameter 400 mm, are machined with half circular grooves and shrink fitted on the inner cylinder. The grooves for the bifilar winding are spaced by 30 mm, i.e. the conductors have a winding pitch of 60 mm. In the center of the winding, corresponding to the magnetic center of SULTAN, the winding pitch is changed to obtain for both conductors a straight half turn at 0 pitch, i.e. perfectly perpendicular to the axis and SULTAN field (see Fig. 2).

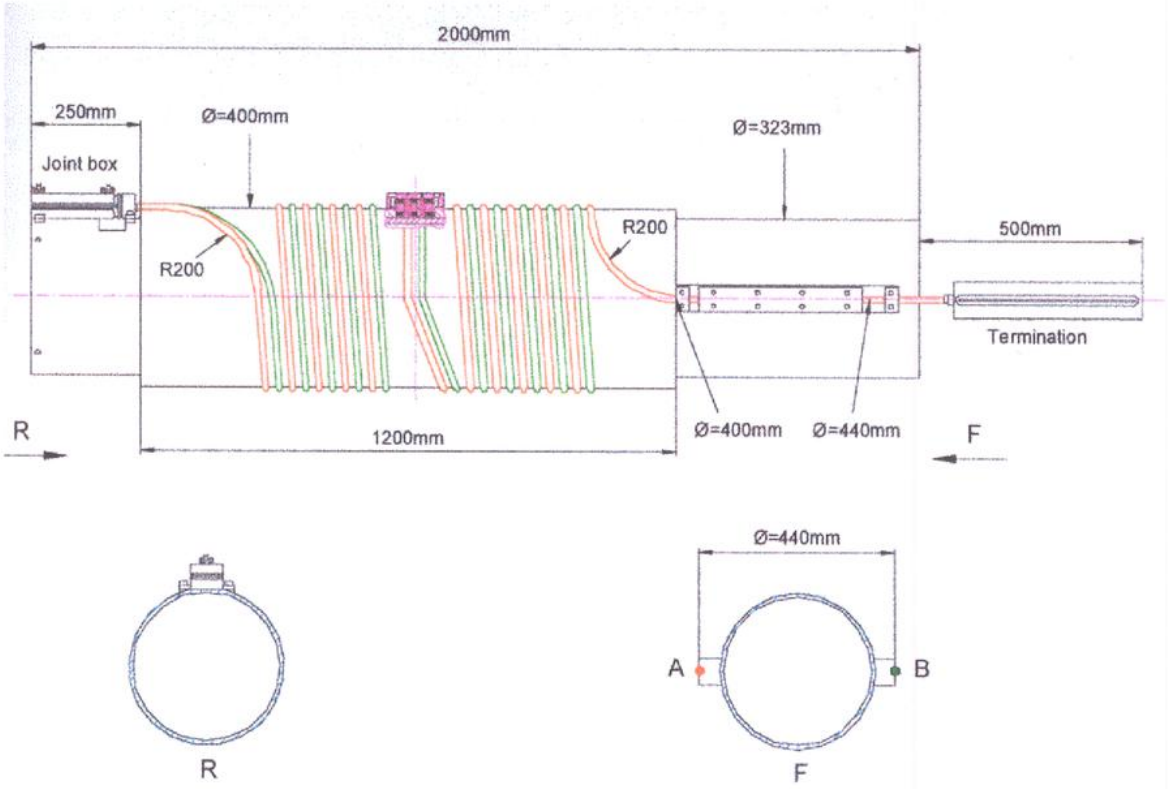

Figure 2 Sketch of the bifilar winding, with the series connected conductors (A and B)

The winding is designed not to be impregnated to allow easy access for instrumentation. The conductors are bolted to the cylinder by a number of steel clamps with machined circular groove. The clamps are 128 mm long and are spaced by a gap of 29 mm, where the voltage taps and temperature sensors are attached. Due to the bifilar layout of the winding, the two conductors carry current in opposite directions and the magnetic forces in the high background field act respectively inward and outward on the two conductors. Each turn of the winding is fixed to the cylinder by 8 clamps for a total of 24 M8 bolts/turn. The maximum operating load, at a background field of 11.5 T and 12 kA current is $2\pi RIB$ = 17.3 t, i.e. 0.7 t/bolt. To avoid that the conductor with inward load becomes loose in its groove, a pre-load of 0.7 t (10 Nm) is applied to each bolt. The cool-down may increase marginally the pre-load. Including the pre-load and neglecting the contribution of the conductor jacket, the maximum load from the hoop forces on the M8 steel bolts is in average 1.4 t/bolt.

Before starting the winding, the two conductor ends, which will be joined together into a hairpin, are dismantled and encased into a welded steel box, consisting of an eye-glass piece and two shells (see Fig.4 top left). The conductor turns are insulated by an overlapped, 0.1 mm thin, glass-mica ribbon, which withstands the heat treatment (wind & react method). The ribbon is manually wrapped on the conductors just before being nested in the cylinder grooves. Starting from the joint box, the conductors are wound under tension into the machined grooves. After each turn, the clamps are bolted to the cylinder. At the straight half turn, a special, temporary clamp replaces the pulsed field coils during the heat treatment. The conductor ends to be connected to the current leads

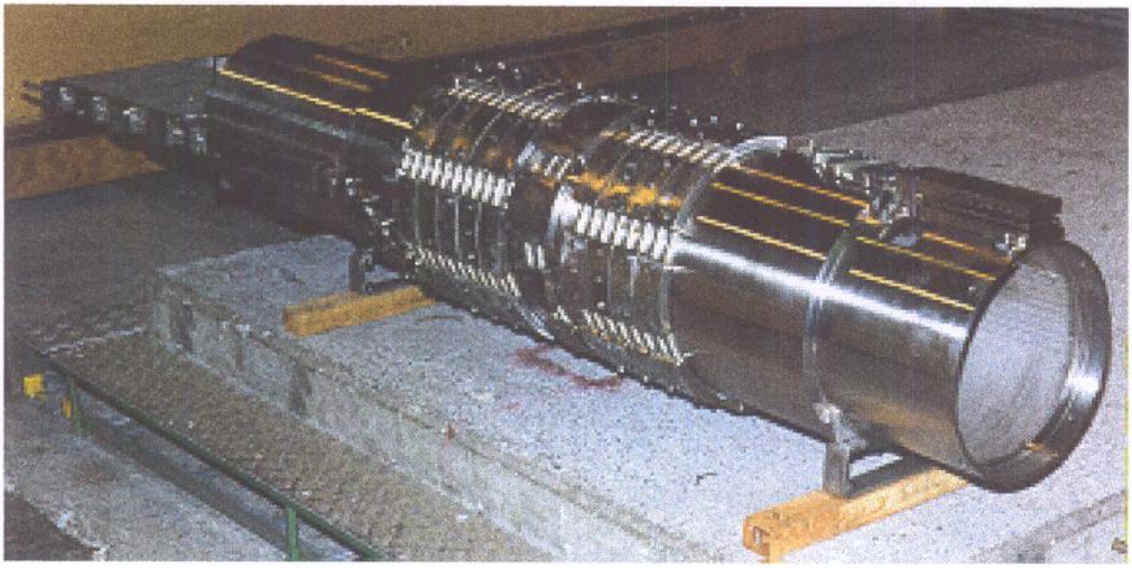

Figure 3 The winding, prepared for the heat treatment

are not prepared before the heat treatment. The straight, protruding conductor sections are temporarily bolted to a support structure, see Fig. 3.

The winding was delivered to CRPP in April 99 and, after leak test, forwarded to Ansaldo (Genova, Italy) to be heat treated in the same furnace built for the TFMC. Four witness I_c strand specimens and the conductor sections for ac losses and $I_c(\varepsilon)$, see section C.1, have been attached to the winding. The heat treatment is carried in Ar atmosphere, with a continuous flow of 50 l/h Ar gas (99.99%) in the conductors. The winding is first flushed five times at room temperature, then heated up to 107 °C and flushed again twice. The temperature is then raised up to 575 °C (126 hrs) and 650 °C (200 hrs). The temperature ramp is in the range of 6 °C/h (up) and 12 °C/h (down). The residual content of O_2 (3-5 ppm), H_2O (< 1ppm) and organic composite (< 10 ppm) is monitored at the gas outlet during the heat treatment. These figures are in agreement with the guaranteed purity of the Ar gas (< 10 ppm O_2). The heat-treated winding was back at CRPP by the end of May 1999.

The joint box was opened after the heat treatment, see Fig. 4. The two steel shells are

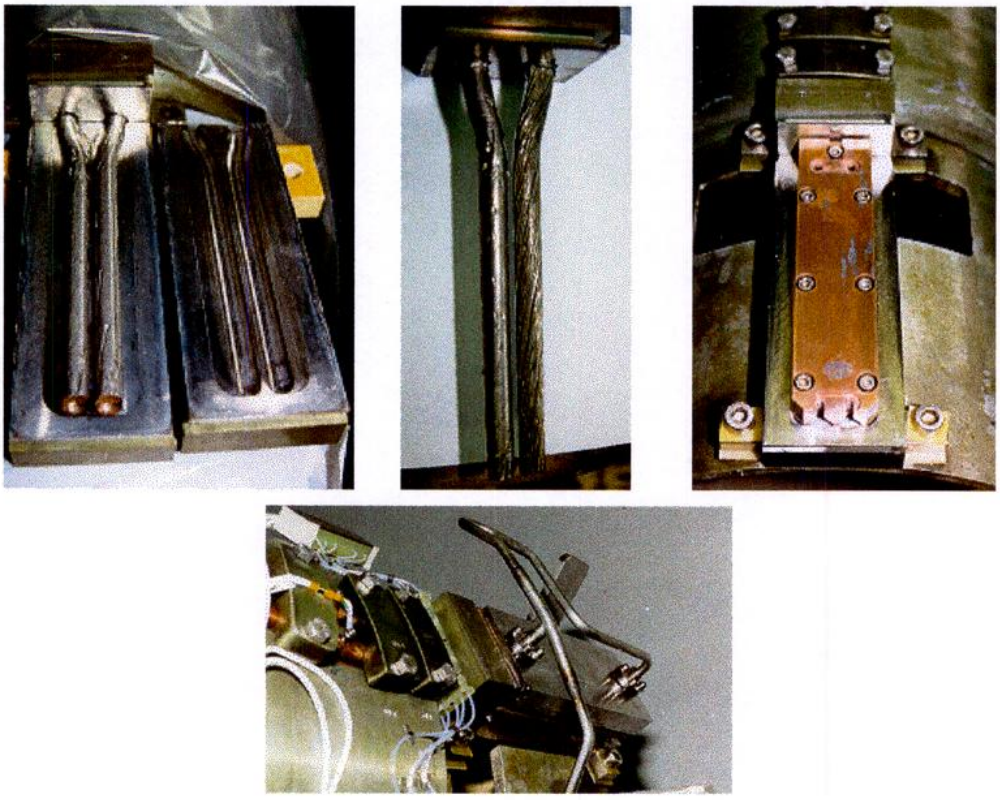

Fig.4 Assembly phases of the joint after the heat treatment

removed to access the two bent cable ends. The cable wrap is removed and the Cr plating is brushed from the cable surface. Solder is applied at the exposed strand surface and the tinned cable ends are encased and bolted into two pre-tinned copper shells, with an interleaved solder foils. The bolted assembly is heated to bond the components and two new steel shells, with the same outer size as the former ones, are welded to the eye-glass piece to build the final joint box. Two parallel He inlets are bolted with Indium seal in the upper steel shell. The coolant streams splits in the joint box between the two conductors. Insulating spacers are applied to the bolts fixing the joint box to the cylinder.

A steel flange, to be bolted to the SULTAN coils assembly as the main structure supporting the winding, is welded to the end of the inner steel cylinder, see Fig. 5. The winding terminations are prepared after the heat treatment. The jacket is dismantled in the last 0.5 m of conductor protruding from the winding flange. The Cr plating is brushed from the cable surface. After solder coating the outer cable surface, the cable ends are inserted in the tinned slot of a vacuum brazed copper-steel box, with an interleaved solder

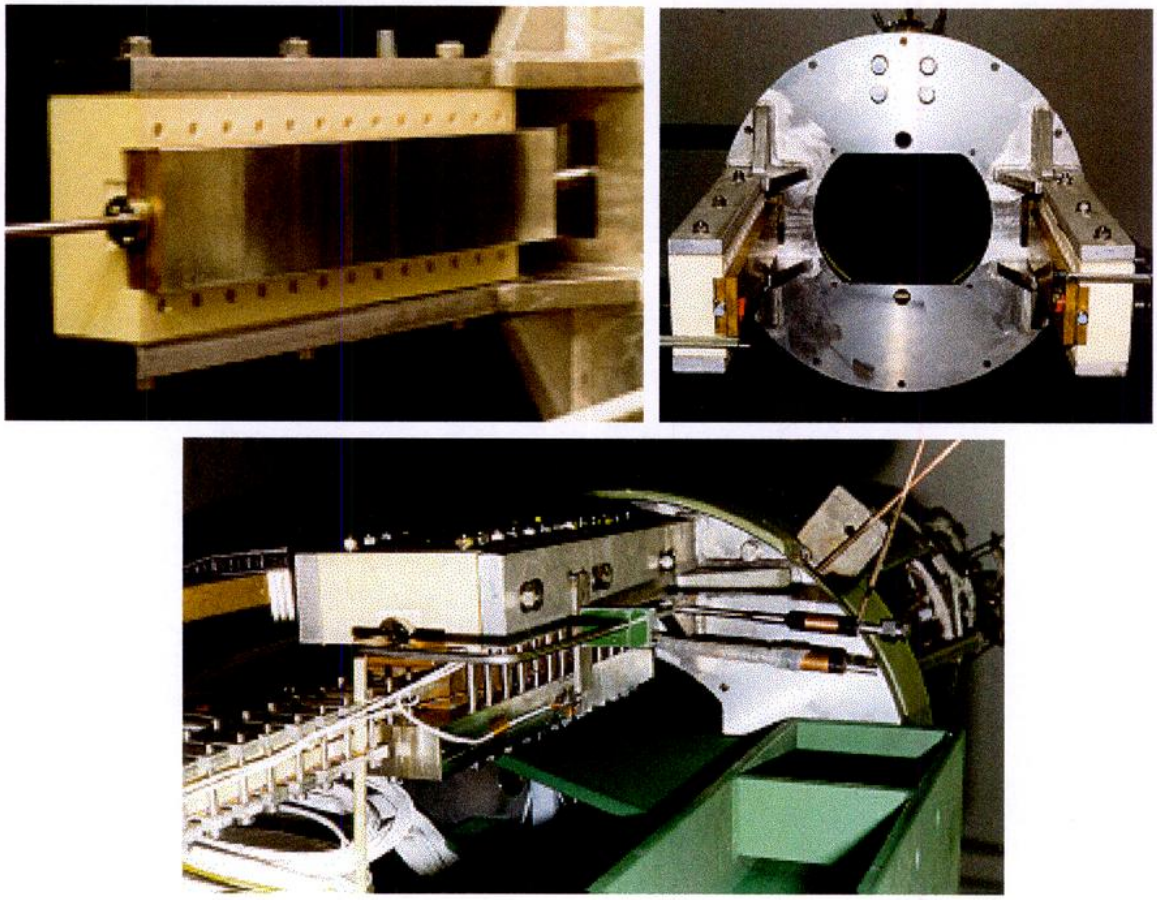

Fig. 5 Assembly steps of the winding terminations

foil. The cable is pressed by a steel lid into the box and heated to bond the cable to the copper. The lid is welded to the upper (steel) side of the box without releasing the pressure. The coolant flows in series from the wound conductors through the termination and the outlet pipes are bolted with Indium seal at the end of the copper-steel boxes. The termination is eventually electrically connected by bolts to a NbTi busbar (recovered from the QUELL experiment) with an Indium foil interleaved at the contact surface, see Fig. 5 bottom.

All the bolts of the conductor clamps were replaced after the heat treatment. In spite of the graphite coating applied to the bolts, about 20% of the bolts broke in their thread and re-drilling and re-cutting of the threads was necessary. After the heat treatment, the conductors with the mica-glass insulation had a resistance to ground in the range of 10 MΩ. Resistance variations have been observed as a function of the moisture: this can be explained assuming that the binder of the mica-glass tape was carbonized during the heat treatment and weak, high resistance paths are built at the cracked folds of the mica layer. Due to the low inductance of the bifilar winding (about 16 μHy including the current leads), the voltage in operation is very low, < 10 V, even at large current rate, e.g. during the fast discharge following a quench. As no significant voltage is applied in operation, the poor insulation could have been accepted. However, to avoid risks of ground loops in the instrumentation, the mica insulation was replaced by a half overlapped kapton tape with identical thickness. To replace the insulation, it was necessary to unbolt the joint box and "unscrew" the winding to lift the conductor from its slot in the winding cylinder. The bending strain at the cable during this operation is estimated ± 0.15 %.

B.3 The Pulsed Field Coils

The pulsed field coils are a key component for the SeCRETS task. They provide a transverse pulse field in the same direction as the background field: either a small amplitude ac field at variable frequency for quasi steady state ac losses test, or a large amplitude, single shot, field transient for stability test.

For symmetry reasons, the pulsed coils are placed at the straight half turn in the middle of the winding, which corresponds to the center of the SULTAN split coils system. The voltage induced by the pulsed field in the SULTAN coil pairs is balanced and no trigger from the quench detection bridge is expected by operating the pulsed coils. The stray field of the pulsed coils at the nearest SULTAN coils is in the range of 3% of the nominal pulse field amplitude. A passive screen (e.g. an Aluminum plate) to reduce the ac losses

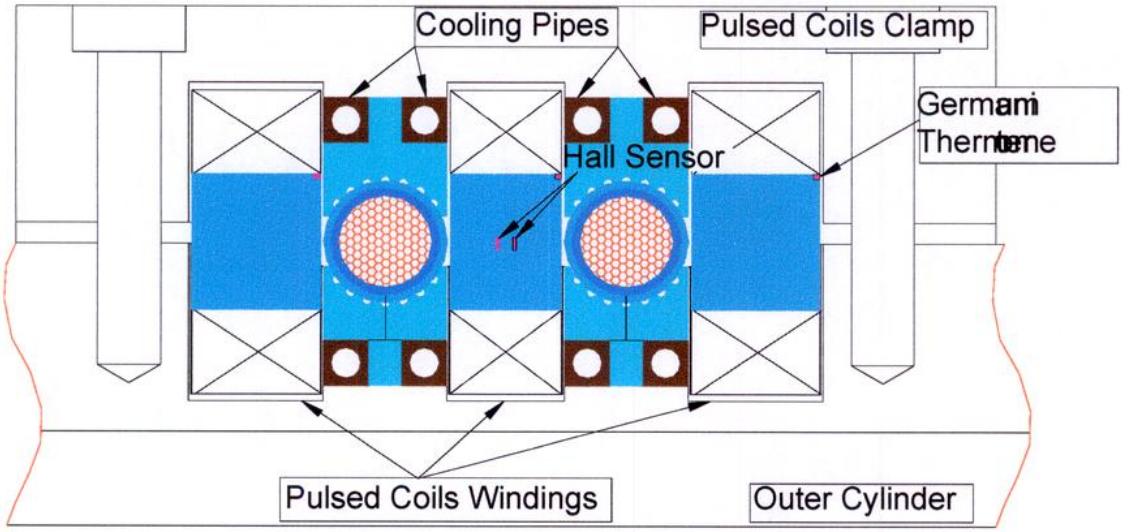

Fig.6 Cross section of the pulsed coils area in the final assembly after heat treatment

in the dc SULTAN coils was first considered, but then discarded due to the poor effectiveness and the large mechanical load in case of a SULTAN coil dump.

To save space and improve the homogeneity of the pulsed field, three series connected windings have been selected. The three planar race track coils are bent (banana shape) at the radius of the winding and cover 90° (about 320 mm of conductor length, i.e. two cable pitches). Cooling pipes have been laid out, attached to the copper windings, to reduce the re-cool time after a pulsed field shot and to limit the conduction heat load to the superconductor. A schematic cross section of the two conductors at the pulsed coil location, including the cooling pipes and instrumentation, is shown in Fig.6.

The design and manufacture of the pulsed field coils has been contracted to the University of Twente, The Netherlands. The coils are layer wound from a varnish insulated rectangular copper wire (1 x 2 mm). The middle coil, to be encased between the conductors, is thinner (13.4 mm) than the two outer coils (15.6 mm). At the inner radius, a Germanium thermometer is attached to the each of the three coils to monitor the temperature after a pulse. In the center of the middle coil, at R= 200 mm, two Hall sensors are embedded to sense the transverse field (both background and pulsed fields).

The three windings have been individually potted with Stycast and glued to the upper steel clamp, see Fig. 7 left. The series connections among the three coils are embedded in slots machined in the steel clamp. The coils terminals and the instrumentation leads are accessible at the outer surface of the clamp. The pulsed field coils, pre-assembled in the

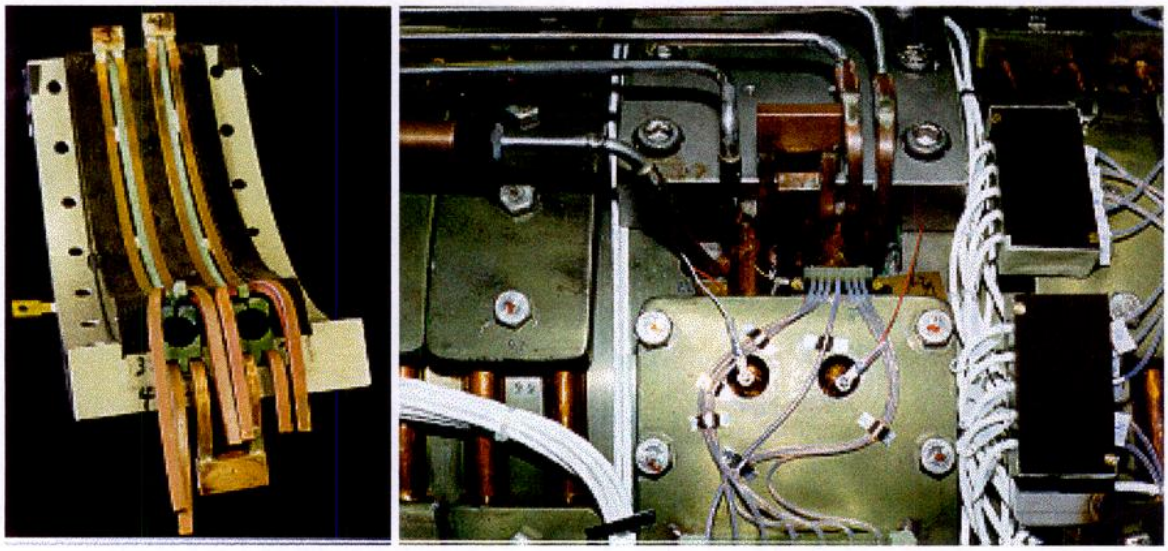

Fig. 7 The pulsed field coils potted in the steel clamp, with matching cooling pipes and spacers (left). Final assembly, with wiring and piping, on the SeCRETS winding

steel clamp, have been delivered to CRPP in July 1999. The correctness of the series connection between the three windings has been checked moving a compass over the steel clamp, with a small current supplied to the system.

Before heat treatment, the conductor is supported in the pulsed coils area by removable steel profiles. After the heat treatment, the supporting profiles are removed without displacing the conductors. The conductor insulation is also removed. Then the cooling pipes, the glass epoxy profiles and the pulsed coils with the steel clamp are assembled in the final position and tightened to the steel cylinder by 16 M10 bolts. A trial pre-assembly of the pulsed coils in the steel clamp with the cooling pipes and the glass-epoxy spacers is shown in Fig. 7, left. The electrical connections to the current leads are potted to allow high voltage operation in vacuum. As the cooling pipes built a loop for pulsed field, bushing insulators are inserted at the hydraulic connections to avoid ground voltage loops and screening of the pulsed field, see Fig. 7, right, upper corner left.

The pulsed field homogeneity over the conductor cross section is ± 15%. The ratio of the pulsed coils operating current to the average field across the conductors is 641 A/T (1.56 mT/A). The coils self-inductance is 2.67 mHy. The low temperature resistance is ≈ 9 mΩ. Two power supplies can be connected to the pulsed coils. With the four quadrants, ± 500 A, ± 100 V power supply, a field can be generated with maximum amplitude ± 0.78 T and maximum frequency ≈ 10 Hz. Using a capacitor bench, a current discharge at the resonating frequency of 15 Hz can be cut by tyristor control after one period (full wave,

65 ms) or half period (half wave, 32 ms). The amplitude of the pulses is limited by mechanical load considerations.

The largest load acting on the pulsed coils comes from the interaction of the pulsed current with the SULTAN background field (up to 11 T). The forces on the pulsed coils are compressive when the pulsed field is anti-parallel to the SULTAN field: in this case the load limit is given by the compressive strength of the winding pack and of the glass-epoxy coil former. For pulsed field parallel to SULTAN, the explosive load, together with the hoop load from the conductor, is taken by the 16 M10 bolts fixing the upper clamp to the steel cylinder. At the assembly, the bolts are pre-loaded with only 0.25 t/bolt (≈ 5 Nm) to increase the operating range. During the actual test, the maximum amplitude of the pulse is limited to about ± 1.6 T (± 1000 A), for an average load up to 3.5 t/bolt. The peak field rate is about 180 T/s. The stray field at the SULTAN coils ± 48 mT, 5 T/s. The re-cool time of the pulsed coils after a capacitor discharge is less than 5 minutes.

The M10 bolts are not insulated. A coupling loop for the pulsed field is built through the upper clamp-bolts-winding cylinder, with an estimated loop resistance in the range of several milliohms. The screening time constant is well below the millisecond range. No evidence of field distortion / attenuation is observed at the Hall sensors embedded in the pulsed coils, at a sampling rate of 1 ms.

The operation of the pulsed coils never triggered a fast discharge of the SULTAN coils. The residual, non-balanced voltage during a pulse on the quench detector bridge is < 50 mV, compared to a quench threshold of 200 mV. The ac losses load of the pulse stray field on the innermost SULTAN coil conductors never caused either a quench or a measurable temperature increase in the coils.

In ac mode, the duration of the pulse is limited by the thermal load to the pulsed coils and depends on its amplitude. A frequently used setting for ac losses measurements is ± 0.35 T (± 224 A) for 7 s duration. The re-cool time (delay between two pulses) is in this case about 25 minutes. The cooling pipes intercept effectively the Joule heat from the pulsed coils and no direct evidence of heat transfer by conduction to the cable-in-conduit conductors is observed during operation.

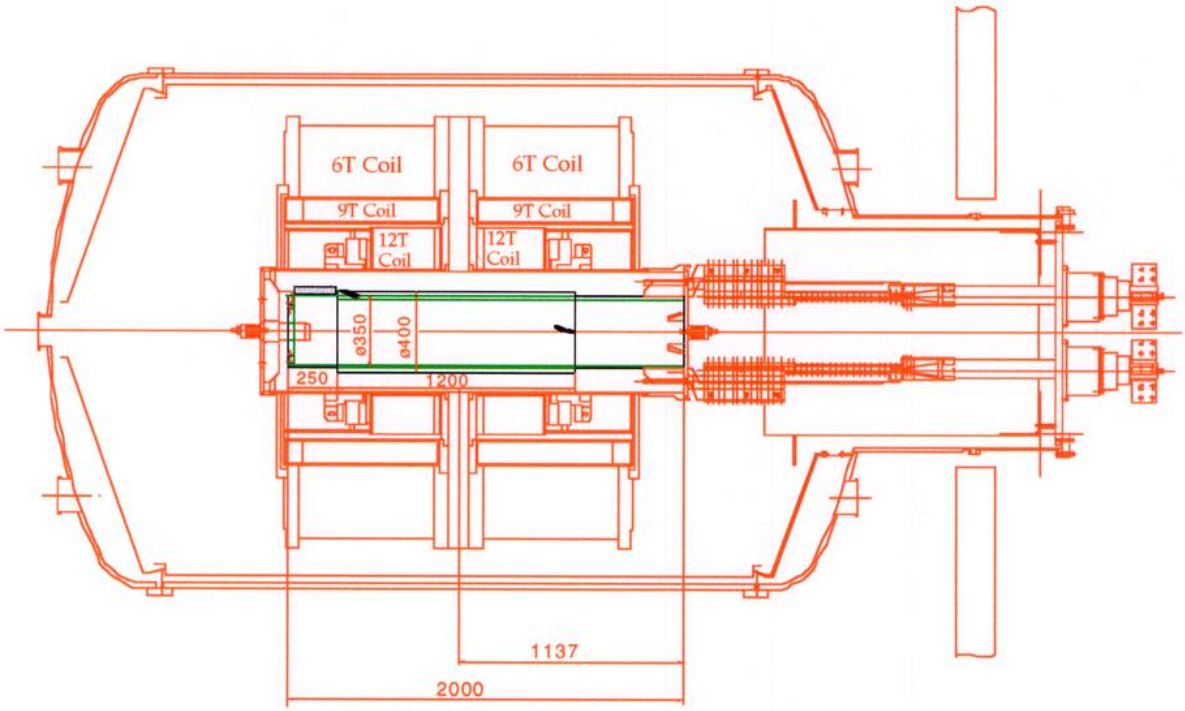

Fig. 8 Top view of SULTAN with the horizontally inserted SeCRETS winding (green contour). The bus bars, current leads and flange are taken from the QUELL assembly

B.4 Cryogenic and Assembly in SULTAN

For the SeCRETS installation, the SULTAN facility had to be re-configured, from the "short sample test" geometry to the "horizontal access", see Fig.8. After warm-up of the facility, the 3.5 m long, rectangular test well for the short samples and the attached set of pulse field coils have been dismantled to free the SULTAN bore. The blind flange of the SULTAN tank for horizontal access has been removed.

The outer flange, the 20 kA feed through and current leads, as well as the straight, 1 m long NbTi bus bar from the QUELL experiment (1996), have been attached to the SeCRETS winding. The termination of the SeCRETS winding is laid out to fit the bus bars of QUELL. The horizontal assembly of winding, bus bar, current leads and flange is shown in Fig.9. As the free-standing assembly is not self-supporting, a large steel bar must be used to displace and lift the assembly before insertion in SULTAN. Eventually, after bolting the winding flange to the SULTAN coils, the horizontal steel bar is removed, while a special tool supports the outer flange. Upon closing the tank, the outer flange is bolted to the large, blue end-cap of the SULTAN tank, see Fig.10.

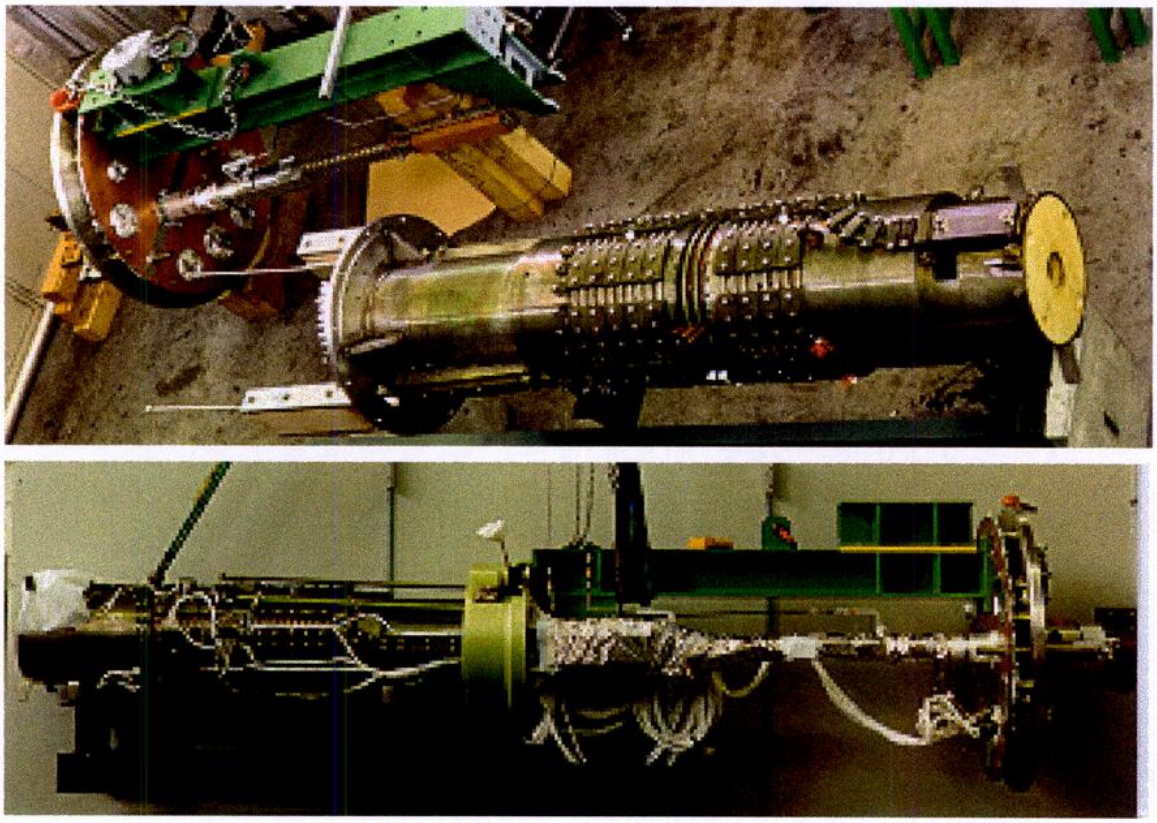

Fig.9 The QUELL components before and after assembly with the SeCRETS winding

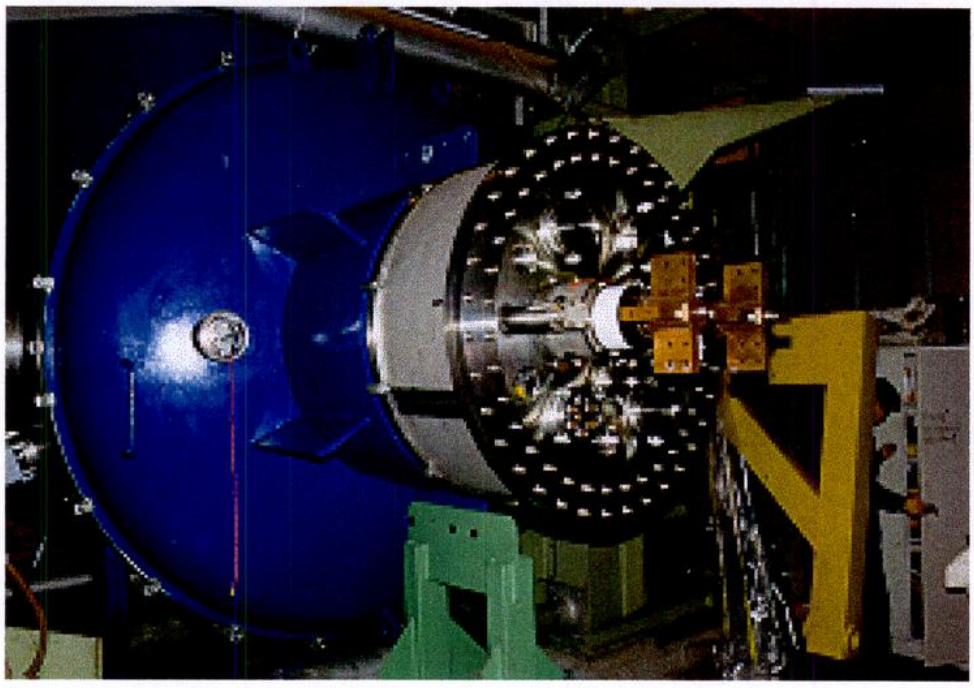

Fig. 10 The flange of SeCRETS after closing the SULTAN tank

A 12 kA, 36 V dc power supply, already used for QUELL, is the current source for the SeCRETS winding. The ramp rate can be set to 50, 100, 200, 400 and 800 A/s. Five sections are independently monitored for quench detection, with individual voltage threshold: the SeCRETS winding, the two NbTi bus bars and the two copper current leads. As the winding is anti-inductive, no compensation has to be done during the current ramp, with residual inductive voltage between the termination < 1 mV at 100 A/s. The current dump is done with an exponential discharge, $\tau = 0.16$ s.

The cooling circuits for SeCRETS are completely separated from the SULTAN coils, with independent cryostat and heat exchanger. The cryostat for the short sample experiment has been modified to service the SeCRETS winding, see Fig.11. The supercritical He supply line (4.5 K, 10 bar) is split in two branches: one branch is led to the SeCRETS joint box were the coolant divides in the two conductors of the winding. Heaters (H0 to H4 in Fig. 11) are attached to the inlet pipe and to the conductors to set-up the operating temperature: H1 to H4 consist each of two series connected resistance foils (MINCO) glued and pressed to the conductor jackets. As the two conductors are fairly good thermally insulated, temperature differences as large as 2 K can be easily set. After passing the SeCRETS termination, the mass flow meters (FI in Fig. 11) and the cryogenic throttle valves, the Helium from SeCRETS is led straight to the cold gas return line.

The other branch of the He supply line passes the pulsed coils (with a by-pass option) and then splits again into two branches: one is led to the JT valve in the cryostat, where the He expands and liquefies. After a pulse field shot, the heat removed from the pulsed coils prevents liquefaction during a short time and may affect the liquid level of the cryostat, which is actively controlled by a 400 W heater. The other branch, with 6 g/s, cools the NbTi busbar and then splits again between a cold gas return line and the copper current leads, with warm gas return. The mass flow rate in the current leads is adjusted by warm valves and flow meters to 1 g/s in each feed-through for full current operation. During the night, the mass flow is reduced to limit the ice build-up at the feed-through.

The mass flow rate is individually controlled in the A and B conductors, in the range of 1.5 to 10 g/s. The operating temperature is mainly controlled by a 80 W heater upstream of the joint. Above 9-10 K and at small mass flow rate, temperature oscillations with a period of 15 - 20 s and amplitude of 0.1 - 0.2 K are observed. With the 0.5 m long, 80 W heater at full power, the density waves turn into a significant He temperature oscillation.

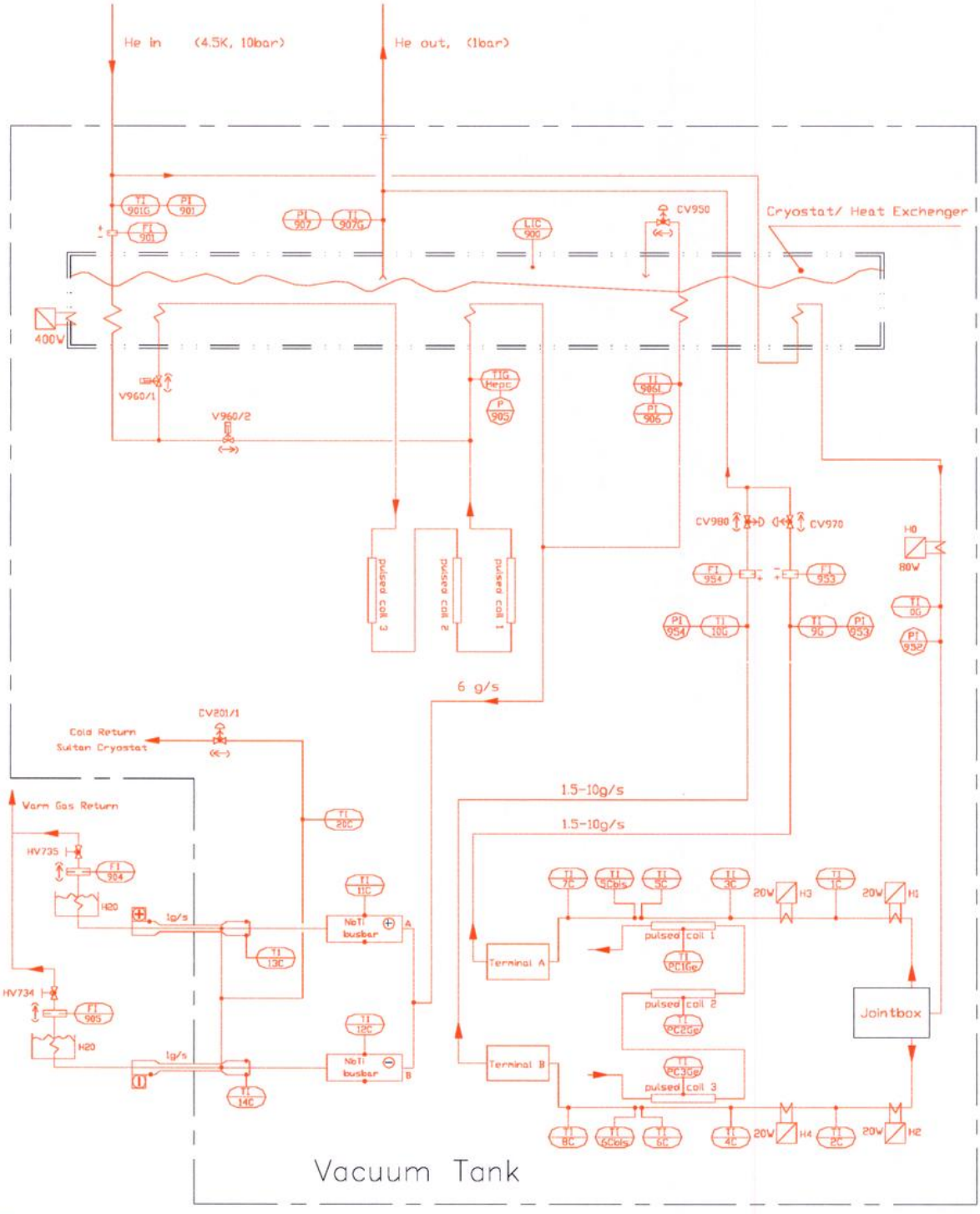

Fig. 11 Cryogenic schema of SeCRETS, with location of temperature sensors (TI), pressure sensors (PI), mass flow meters (FI) and valves

Pressure sensors (PI in Fig.11) are placed before and after the winding. As they also include the joint box and the winding termination, where the conductor cross section is substantially reduced, no reliable hydraulic characterization of the SeCRETS conductors

could be done. The operating pressure at the location of the pulsed coil is estimated as the average of inlet and outlet pressure.

B.5 Instrumentation and Data Acquisition

The location of the instrumentation on the SeCRETS winding, and partly the range of the test program, is dictated by the profile of the SULTAN field. Due to the slight asymmetry of the split coils, the field at R = 200 mm (i.e. on the surface of the winding cylinder) has the shape of an uneven saddle, with the pulsed field coils placed at the center. According to the field plot in Fig.12, the major peak field is at Z = -230 mm and the minor peak is at Z = 220 mm. The field at the saddle is 93.6% of the major peak. With the SULTAN coils at full current (nominal set "11 T"), the major peak is 11.36 T, the saddle is 10.635 T and the minor peak is 11.10 T. Depending on the polarity, the pulsed field may either add or subtract to the SULTAN field at the saddle location. Voltage taps and temperature sensors along the conductors are centered at the two field peaks (which are the test zone for dc performance) and at the pulsed field zone, where ac losses and stability are measured.

The temperature sensors are attached to the cooling pipes and to the conductors to sense

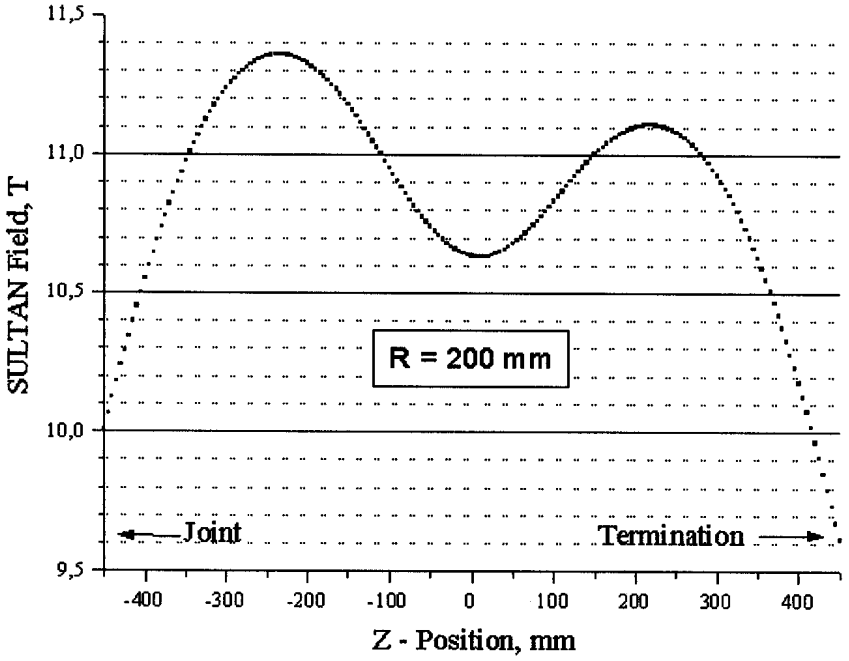

Fig. 12 SULTAN field profile at the surface of the winding cylinder. The plot is done for the nominal set "11 T"

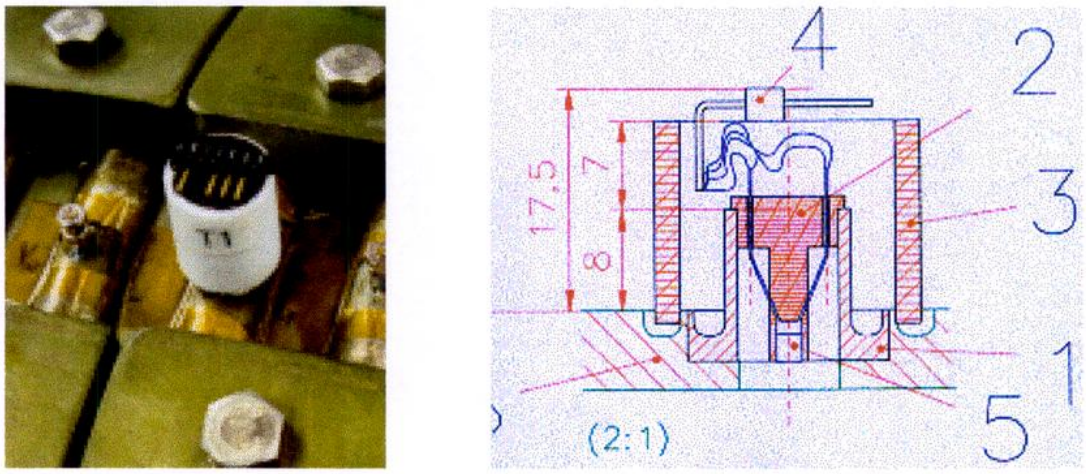

Fig. 13 A CERNOX sensor and voltage tap on the SeCRETS winding. Legend: 1 steel T-piece, 2 glass-epoxy holder, 3 Teflon can, 4 leads connector, 5 CERNOX sensor

the coolant temperature. A hole is drilled in the conductor jacket and a short, steel T-piece is weld over the hole. A glass-epoxy holder with the CERNOX sensor is fitted into the T-piece and sealed by Stycast into a Teflon can, with the sensor leads soldered into a standard, 4-pins connector, see Fig. 13, according to the reliable method always used at CRPP for the short sample test. All CERNOX sensors worked properly, with little noise and good accuracy, providing consisting signals, with accuracy in the range of 0.02 K.

Fifty-two voltage taps (26 voltage pairs) are attached to the conductors, terminations and current leads. A voltage taps, see Fig. 13 left, consists of a M3 bolt spot welded to the conductor jacket. The leads of the voltage pairs are twisted. The location of voltage taps (V), the SeCRETS instrumentation and the heaters is shown in Fig. 14.

Fifty-eight miniature Hall sensors are attached to the SeCRETS conductors. The sensors have been procured in Russia, through the Kurchatov Institute and have been delivered with a calibration sheet. The sensor size is either 1.5 x 1.5 mm or 2 x 2 mm, the active area is 0.2 mm^2 or less. The miniature Hall sensors and their leads need to be handled with great care. During the installation, two sensors are lost due to lead breaking. After cool-down and extensive testing, another four sensors are found out of order. In a couple of cases, a large offset voltage is observed, but the sensors are still working. Fifty-two out of fifty-eight sensors provided useful data. Two sensors are used to monitor the actual field (background plus pulsed field) in the center of symmetry of the pulsed field coils.

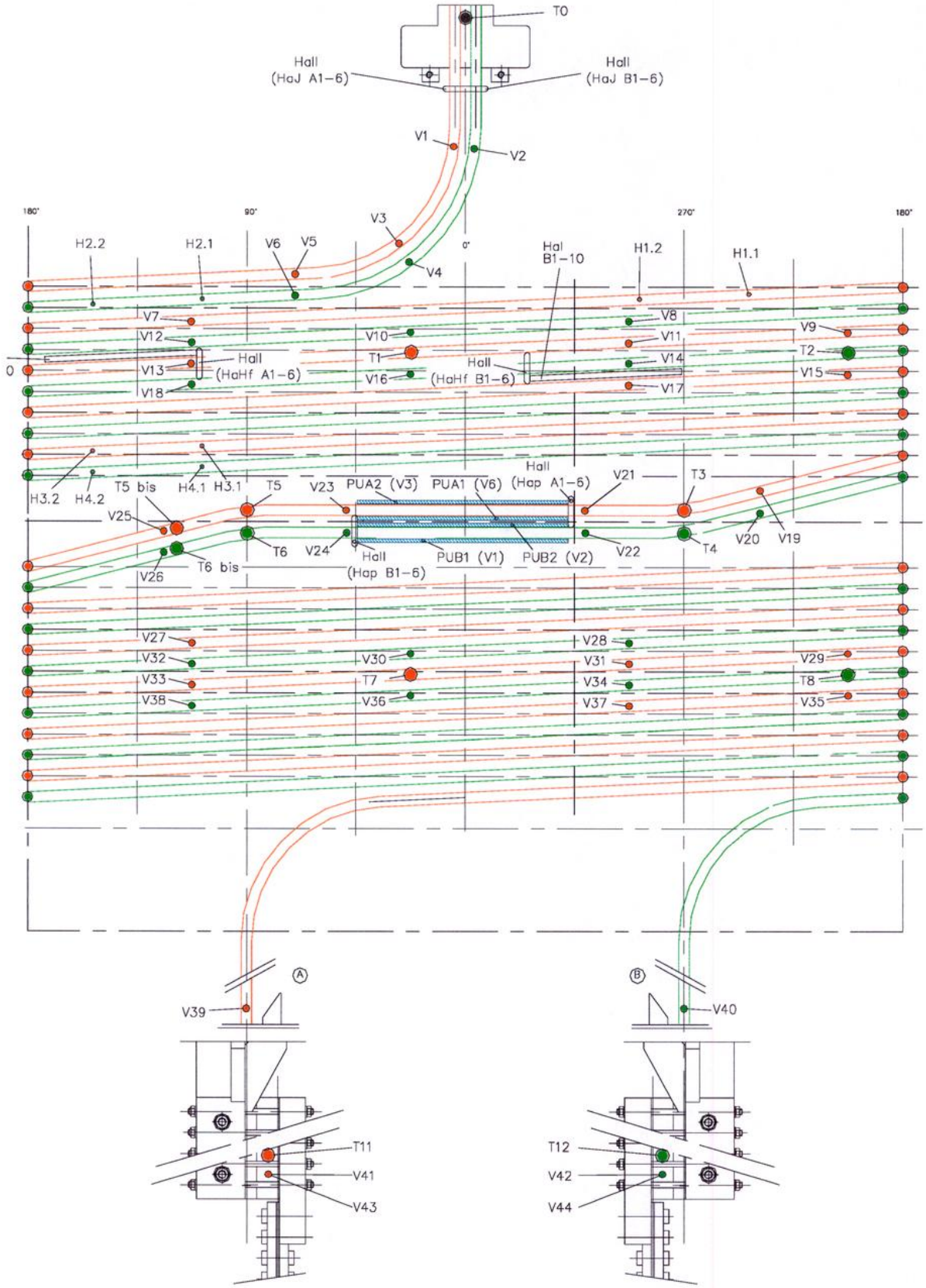

Fig. 14 Instrumentation map of the SeCRETS winding (cylinder surface developed)

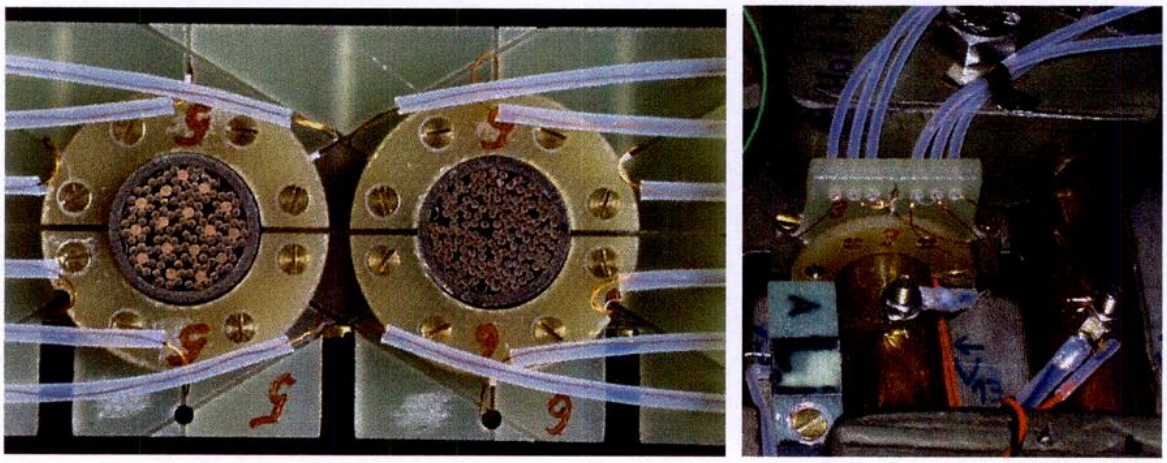

Fig. 15 The annular arrays of 6 Hall sensors, in a mock-up assembly (left) and as built in the winding

Six annular arrays of Hall sensors (three for each conductor) are placed respectively just after the joint (HaJ A1-6 and HaJ B1-6), at the peak field location (HaHf A1-6 and HaHf B1-6) and at the pulsed coil location (Hap A1-6 and Hap B1-6), see Fig. 14, to map the current distribution over the cable cross section. The layout of an annular array, containing six Hall sensors at 60° spacing, just touching the outer surface of the conductor jacket, is shown in a mock-up assembly in Fig. 15. Due to the orientation of the sensors, the background field (up to 11 T) must be subtracted from the signal of the Hall sensors and the accuracy of the self-field measurements (in the range of 0.25 T @ 12 kA) is poor: the background field is first recorded at 0 current and then subtracted from the signal with current. However, the signal to noise ratio is poor after the subtraction.

Two "linear arrays", each containing 10 sensors, are placed along the conductors in the high field. The sensors are spaced by 17.8 mm, i.e. the array covers a full cable pitch of 160 mm, see Fig. 16. In the instrumentation map (Fig. 14) the linear arrays are named *Hal A1-10* for A-conductor and *Hal B1-10* for B-conductor. The sensors are parallel to the cylinder surface and they do not sense the SULTAN background field. As no significant compensation of the background field is required, the sensors in the "linear arrays" have the best signal-to-noise ratio and work only in the low field range, where the linearity of the Hall coefficient is best.

The ac losses on the SeCRETS conductors are measured by gas-flow calorimetry, using the temperature sensors T5 and T6, placed just after the pulsed field coils (another pair of thermometers, T5bis and T6bis are added for redundancy). As a back-up method for ac losses measurements, four saddle shaped pick-up coils are attached to the conductors in

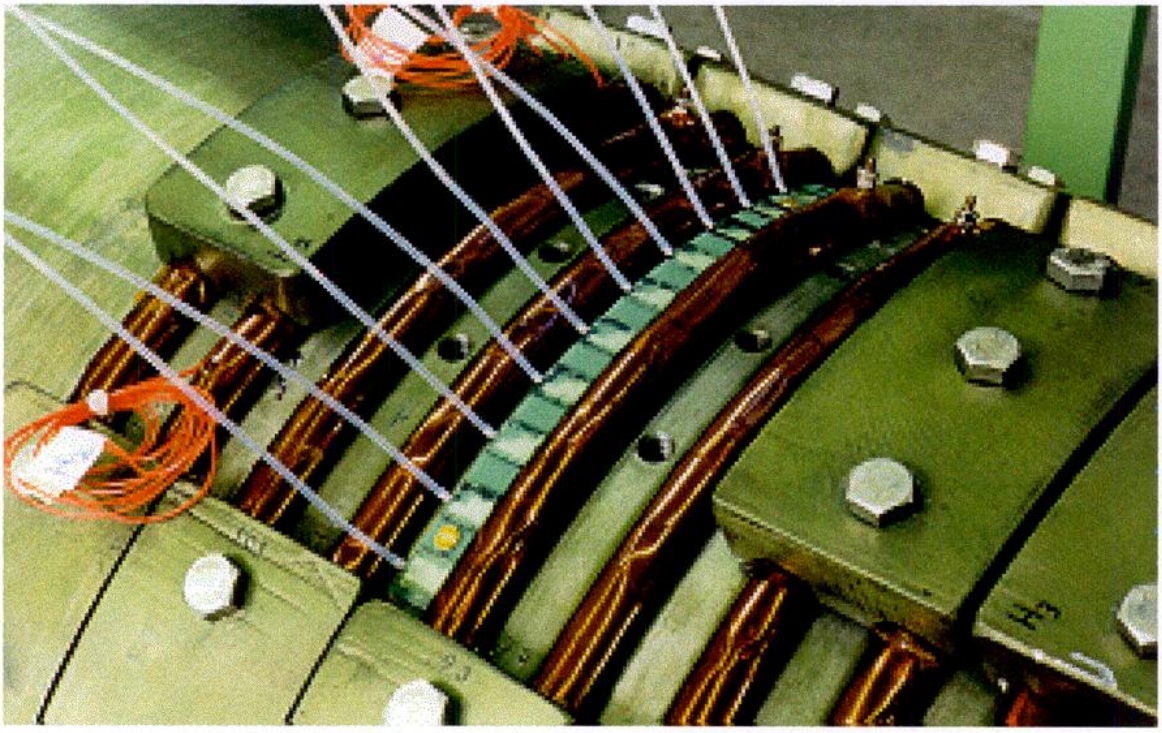

Fig. 16 A linear array of 10 Hall sensors in the glass-epoxy holder (clamps removed)

the pulsed field zone to detect the magnetization. The 8 turns of the pick-up coils are spaced to carry out two-dimensional flux integration. To fit the toroidal surface of the conductors, the pick-up coils are manufactured by high precision machining a copper plated glass-epoxy shell, molded on a section of SeCRETS conductor, see Fig.17.

The two pick-up coils of each conductor, *PUA1 - PUA2* and *PUB1 - PUB2* according to Fig.14, are series connected to enhance the signal. During the experiment, some problem arose with the treatment of the voltage from the pick-up coils, due to non-reproducible

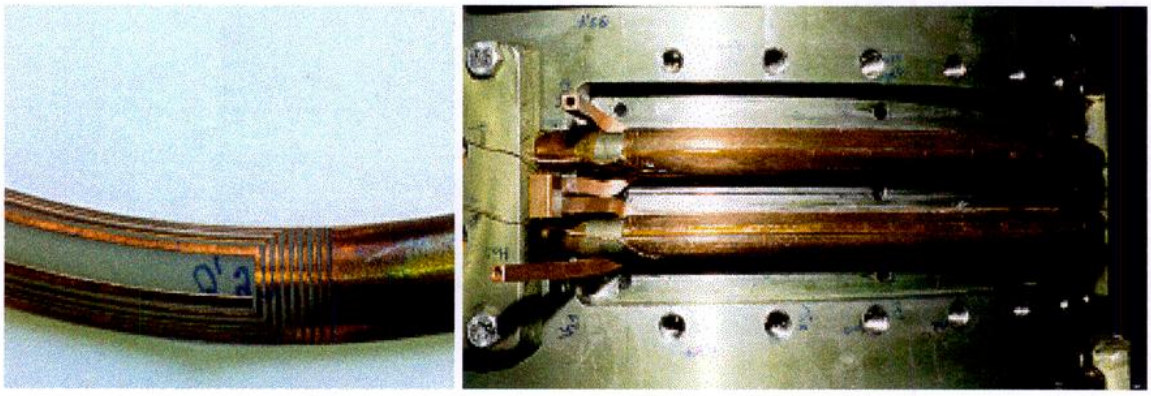

Fig.17 A detail of the pick-up coil during manufacturing (left) and during the assembly on the conductor in the section of the pulsed coils (right)

signals (possibly thermal voltages at the soldered connection, not anchored to a fix temperature) overlapping to the magnetization signals. Eventually, no accurate ac losses results were obtained by the pick-up coils, while the gas-flow calorimetry was very accurate.

The data acquisition system in SULTAN has a total of 80 channels, with sampling rate adjustable up to 1.8 kHz/channel. As the number of sensors and voltage taps exceeds 80, two configurations of the data acquisition channels have been set-up: the baseline configuration, labeled "N", includes all the instrumentation except 32 Hall sensors. A second configuration, labeled "C", mostly used for current distribution investigation, includes all the Hall sensors and excludes pressure sensors, pick-up coils, heaters and about 20 voltage taps.

Each channel has an adjustable low-pass filters and a low noise amplifier. Most of the sensors have 4 Hz filters. During the stability runs, the cut-off frequency of the filters for voltage taps and Hall sensors is raised, with obvious penalty on the noise level.

The dc and most of the ac losses test runs used a low sampling rate, 100 ms/channel: in this mode, on-line monitoring of the sensors on the screen is possible. A typical data file from a test run at this sampling rate has the size of about 700 kB/minute. Stability runs are taken at a sampling rate of 1 kHz/channel and last typically for 4 s, to limit the size of each file to about 1 MB.

The formatted data files are imported in ORIGIN spread sheets, where plots are generated and a basic reduction of the data is done. The identification label of the ORIGIN file includes nine digits. The first digit is acquisition channel configuration: either "N" for normal mode or "C" for current distribution mode. The second digit identifies the runs taken either during the tuning of facility and instrumentation, "O" for Operation Test, or as actual experimental runs, "E". The third digit is for the subcategory of the test: "D" for dc tests, "A" for ac losses, "S" for stability. The 4^{th} to 7^{th} digits are the date (day and month). The 8^{th} and 9^{th} digits are for the sequential number of file in the day (no more than 99 files/day)

Example: NEA090504 Means: the fourth run taken on May 9^{th}, with the data acquisition channels set in normal operation mode, valid experiment on ac losses

C. Test Results

C.1 Conductor Characterization outside SULTAN

The results of geometrical verification (twist pitches, void fraction, diameter) are already reported in Table 1 of Section B. The cryogenic tests include the strand $I_c(B, T)$, the conductor ac losses and interstrand resistance on short samples (carried out at the University of Twente) as well as the $I_c(B, \varepsilon)$, contracted to FzK, Karlsruhe.

C.1.1 Strand Testing

Four I_c strand specimens has been heat treated together with the SeCRETS winding on the standard I_c sample holder (TiAlV alloy) developed during the ITER strand bench mark action. The test sections are taken from the 5 m long, non-plated strand sections delivered by VNIINM for each billet used in the procurement.

2 specimens, labeled B1 and B2, belong to Billet **B – 211**
2 specimens, labeled A1 and A2, belong to Billet **A – II – 1**

The specimens have been attached to the winding at following locations:

A1 at the joint box
A2 at the mid of winding
B1 at the highest field section of the winding
B2 in the bore of the winding cylinder, close to the $I_c(\varepsilon)$ specimens

Three sets of critical current and *n* factor results for the strand A-II-1 and B-211 are listed in Table 1. All the data are at 12 T background field, 4.2 K, 0.1 μV/cm. First are the data from the VNIINM Certificates, with sample holder made of Ti and heat treatment at VNIINM, then the data of UT and last the data measured by VNIINM on the same specimens of UT (sent to Moscow after the test).

Table 1. Summary of I_c test on strand specimens @ 12 T, 4.2 K, 0.1 μV/cm

	A – II – 1		B - 211	
Strand diameter	0.811		0.819	
Cu : non-Cu	1.54		1.02	
I_c from VNIINM Certificate	119		148	
	A-II-1 (A1)	A-II-1 (A2)	B-211 (B1)	B-211 (B2)
I_c / n from UT test	105/31.4	106.6/32.3	130.6/30.5	130.8/31.1
I_c / n from VNIINM test	108/33	110/34	140/34	137/33

Comparing A1 with A2 and B1 with B2, the differences are marginal, suggesting that the heat treatment temperature has been homogeneous over the whole winding sample (as confirmed by the temperature sensors used by Ansaldo). The *n* factor is high. The disagreement between the VNIINM certificate and the UT results is large and may be partly due to the different sample holder and heat treatment. The discrepancy (ΔI_c) between the UT and VNIINM results on the same physical specimens (last two rows of the Table) is about 3% for A strand and 7% for B strand, i.e. worse than in the ITER strand bench mark test.

The critical current results vs. field at 4.2 K, 0.1μV/cm is plotted in Fig.1. The results as a function of field and temperature are shown in Table 2. Assuming an intrinsic strain on

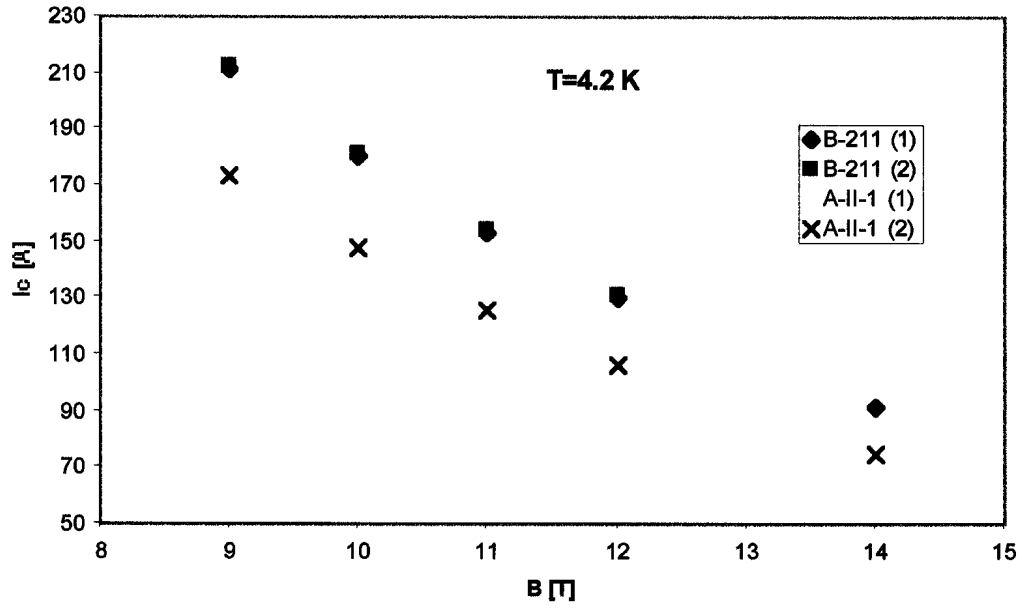

Fig. 1 Critical current results of UT on strand witness samples

Table 2 Critical current results vs. field and temperature

		B-211-1		B-211-2		A-2-1-1		A-2-1-2	
B	T	10E-6V/m		10E-6V/m		10E-6V/m		10E-6V/m	
[Tesla]	[Kelvin]	Ic	n	Ic	n	Ic	n	Ic	n
14	4.23	91.4	29					74.3	30
12	4.23	130.6	31	130.8	31	105.0	31	106.6	32
11	4.23	153.5	31	154.2	32	123.9	33	125.6	33
10	4.23	180.3	33	181.1	33	145.8	34	147.7	34
9	4.23	211.3	33	212.4	34	171.2	35.8	173.2	35
12	6	98.7	30	96.7	30	77.2	29	78.4	32
11	6	119.6	31	117.1	30	93.7	31	94.9	31
10	6	143.2	32	140.8	32	113.1	32	114.3	32
9	6	170.7	35	168.2	33	135.6	33.7	137	34
12	7	75.9	30	75.1	27	59.5	27	60.3	27
11	7	94.7	29	93.4	29	74.4	29	75.3	29
10	7	116.5	28	114.4	35	91.9	30	92.8	30
9	7	141.4	33	139.4	33	112.3	31.1	113.3	33
12	8	*	24	53.1	27	41.6	25	42.2	25
11	8	*	32	69.2	28	54.8	25	55.3	27
10	8	*	*	87.5	26	70.1	27	70.7	28
9	8	*	*	109.9	27	88.4	29.4	89.1	28

the strand ε = -0.25%, a set of scaling parameters is drawn, slightly different for A and B strand, see Table 3, according to the Summer's scaling law. The C_0 parameter in Table 3 is for the critical current criterion of 0.1 μV/cm. If the criterion 1 μV/cm is used, the original C_0 parameter must be multiplied by a factor 1.08, see also section C.3.4. The Table 3 also includes the average RRR results and hysteresis loss from the VNIINM certificates. The lower RRR in strand B is explained with the thinner copper shell due to the lower Cu:non-Cu ratio: the impact of the Cr diffusion layer (about 35 μm according to VNIINM) is larger in B than A. Without Cr plating, RRR is the same, about 130, in both strands.

Table 3 Scaling law parameters for the witness strands and average strand data

	Strand A	Strand B
T_{com} [K]	17.3	17.7
B_{c20m} [T]	32.65	32.80
C_0 @ 0.1 μV/cm [A·T/mm^2]	$6.587 \cdot 10^9$	$6.198 \cdot 10^9$
Average RRR	107	95
Average non-Cu Hyst. Loss, ± 3 T, [mJ/cm^3]	165	158

C.1.2 AC losses and interstrand resistance test

The ac losses were measured on 480 mm long, straight sections of the cable-in-conduit conductors, heat treated together with the SeCRETS winding. The test was carried out in the "virgin state", i.e. without any mechanical and electromagnetic load on the strand bundle. The applied sinus field had ± 0.4 T amplitude (no background field). The ac losses were measured by boil-off calorimetry. The results (loss curves) are gathered in Fig. 2 and Table 4.

The loss curves of conductor A and B, normalized to the superconducting strand volume converge unexpectedly to the same hysteresis loss. In fact, as the non-Cu content is the same, it is expected that the hysteresis loss, normalized to the strand (not to the non-Cu) volume, is higher in B. However, in the range of B = ± 0.4 T, the hysteresis loss is dominated by the Nb diffusion barrier rather than by the filament magnetization. In the VNIINM certificates, the non-Cu hysteresis loss over a ± 3 T cycle is quoted 165 mJ/cm^3 (average of A strand) and 158 mJ/cm^3 (average of B strand).

The slope of B (circle) is smaller than A (square), suggesting smaller coupling currents loss. Normalizing the loss results to the overall cable volume (or to the cable length), the ac losses difference becomes almost a factor of two (see Table 4), mostly due to the effect

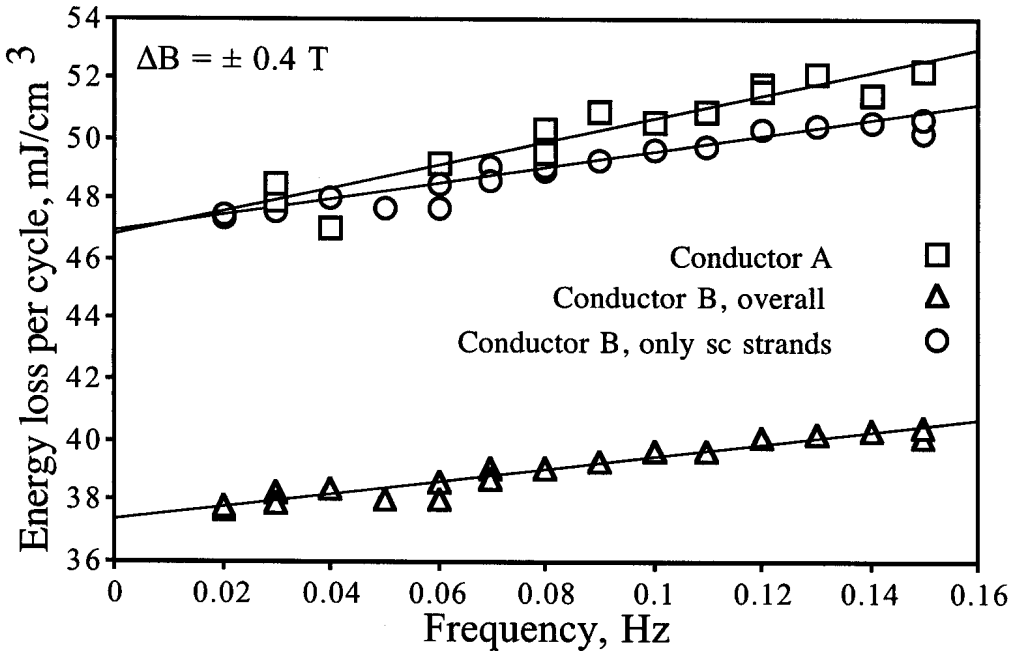

Fig. 2 AC losses of conductors A and B, normalized to the sc strand volume (square and circle) and to overall cable section, strand and Cu core (square and triangle)

Table 4. Summary of coupling loss results on short samples

	Conductor A	Conductor B
nτ (sc strand volume), ms	15.2	10.4
nτ (overall cable volume), ms	**15.2**	**8.3**
$n\tau \cdot A_{cable}$ (loss per unit length), ms·mm^2	0.205	0.112
Average R_c @ 0 T, nΩ·m	210	435
$n\tau \cdot R_c$, 10^{-9} s·Ω·m	3.6	3.2

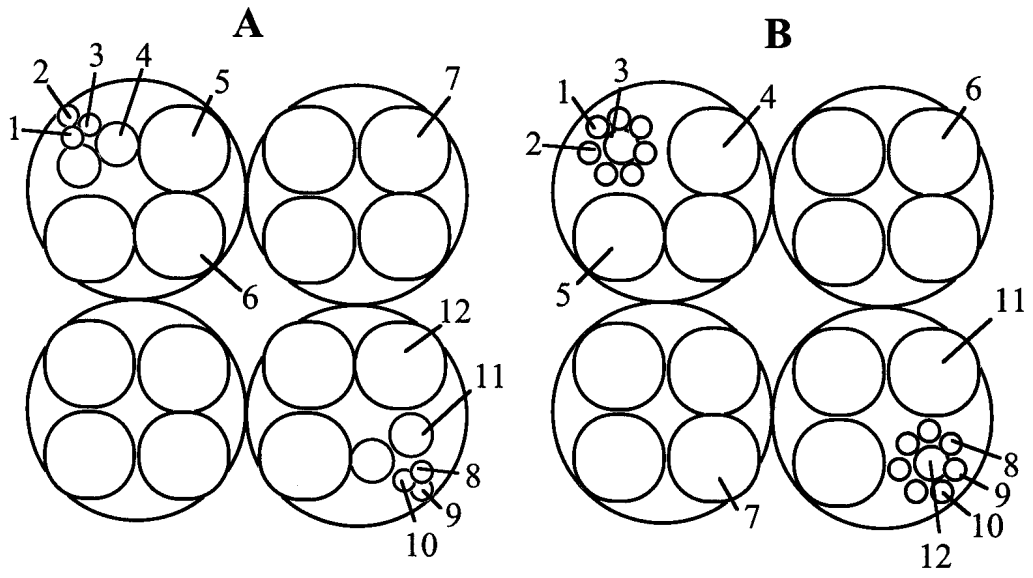

Fig. 3 Wiring schema for interstrand resistance specimens

of the segregated copper in conductor B. The coupling loss in the SeCRETS conductor is smaller than expected in Nb_3Sn cable-in-conduit in "virgin state". In the ITER "Cr vendor comparison" results, the Cr plating of VNIIKP was observed to be the most effective to reduce the coupling loss in "virgin state". A further loss decrease is expected (and observed) in operation, due to the electromagnetic loads affecting the interstrand resistance at the strand crossovers.

The interstrand contact resistance times length, R_c (Ω·m), is measured in 480 mm long, straight sections of conductor A and B. At one end of the jacketed conductor, the cable bundle is opened and a number of strand pairs, see Fig. 3, is wired. The resistance is measured from the V vs. I curve at 0 and 1 T background field, with marginal increase at higher field. The resistance is constant over a broad range of dc current (up to 80 A).

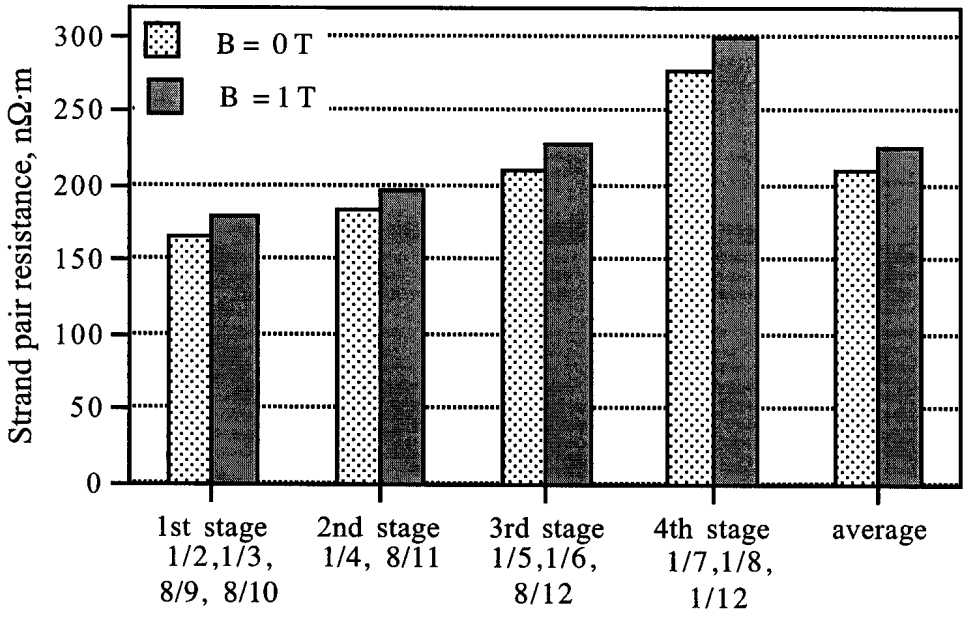

Fig. 4 Interstrand resistance in conductor A

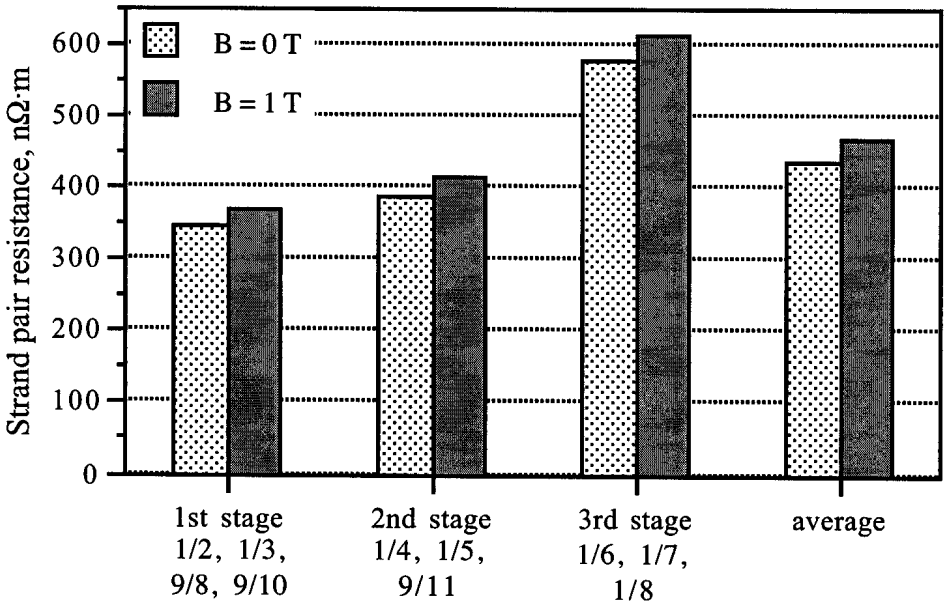

Fig. 5 Interstrand resistance in conductor B

The test results for interstrand resistance are gathered in Fig. 4 and 5. The resistance between adjacent strands in the first cable stage, as well as the average resistance in the bundle, is about a factor of two higher in conductor B. This may be explained considering that the interstrand resistance in a multistage cable is the results of the several zigzag

paths of sc strands with different angle in the bundle: the larger number of sc strands and the larger average angle of strands in bundle in A (due to the larger number of cable stages) correlates with the lower transverse resistance in A. The Cr plated copper wires in conductor B do not contribute practically to the transverse conductance. The contact resistance of an individual sc strand crossover is assumed to be identical in A and B, due to the identical Cr plating. The average interstrand resistance in the bundle correlates well with the coupling loss results. The product $n\tau \cdot R_c$ is identical, within the accuracy of the results ($\approx$ 10%), for conductor A and B, see Table 4.

C.1.3 I_c versus axial strain in CICC specimens

Four straight cable-in-conduit conductor specimens, heat treated together with the SeCRETS winding, have been measured in the bath cooled split coils of the FBI facility at FzK, with field up to 14 T, current up to 10 kA and axial load up to 100 kN (see Report TWO-T405-2/01). The critical current of the steel jacketed conductors was first measured vs. applied field at zero applied strain, see Fig. 6, which includes the strand results at the same criterion of 1 μV/cm (heat treatment witness specimens). The large difference between the results of strand and the steel jacketed conductors is due to the axial thermal strain induced in the Nb_3Sn filaments by the steel shrinkage, in good agreement with

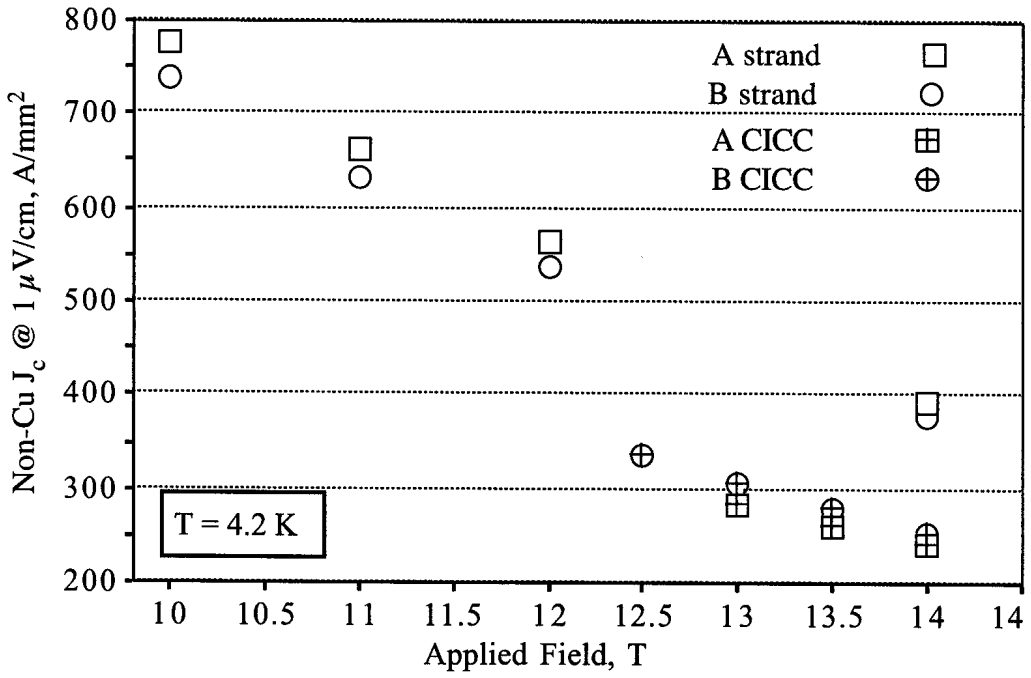

Fig. 6 Critical current density vs. field in CICCs and strands

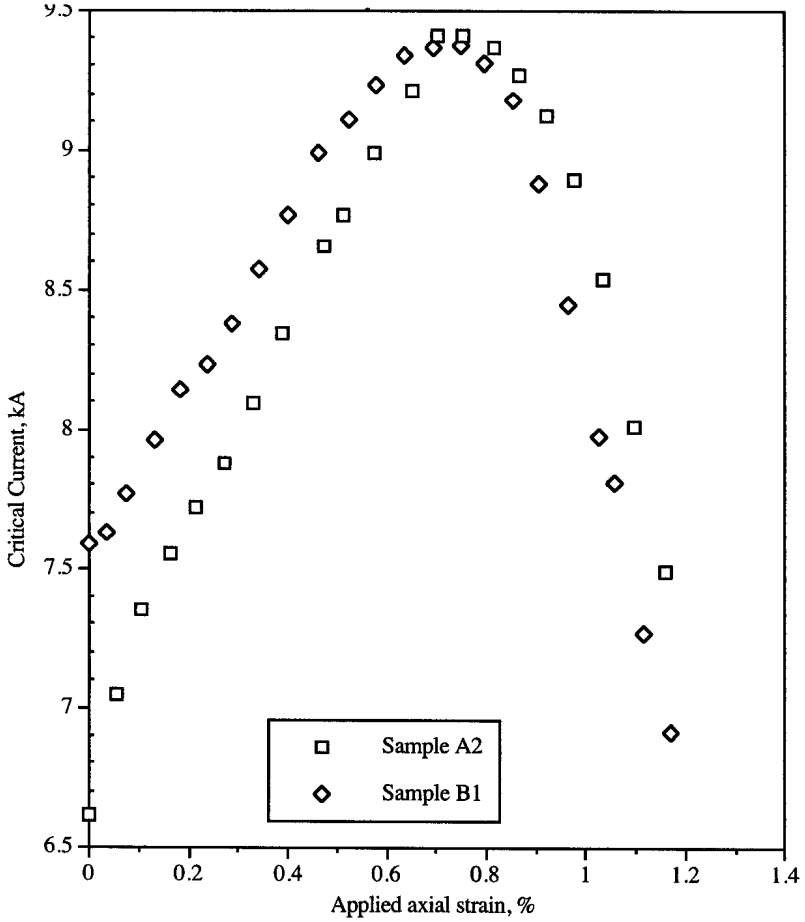

Fig. 7 Critical current vs. applied axial strain at 14 T, 4.2 K and 1μV/cm

former test on similar specimens.

Afterwards, at B = 14 T, I_c was measured as a function of the applied axial strain, see Fig. 7, (two out of four specimens). The electrical field criterion for I_c is 1 μV/cm, with voltage taps spaced by 50 mm. The peak of I_c vs. ε occurs at ε = 0.72 - 0.74 % applied strain, as it is expected in a steel-jacketed conductor. However, the ratio of I_c without applied strain to the peak J_c is much smaller compared to 0.4-0.6 measured on similar cable-in-conduit conductors. The peak current is smaller than expected and the whole curve $J_c(\varepsilon)$ remain, at any strain, much smaller than the J_c measured on the strands. To date, the reason of the missing recovery of I_c after applied tensile strain is not clarified. As this effect was not observed in the SULTAN test, it is likely due to the specimen preparation procedure. The results of Fig.6 and 7 are not further used in the report.

C.2 Objectives of the test in SULTAN

The two major items of the test of the SeCRETS winding sample in SULTAN are described by the following procedures:

- ***Plasma Disruptions***. The conductors carry the highest operating current density (400 A/mm^2) with background dc field. The operating temperature is set for a temperature margin of 1 K at the location of the pulsed coils. A pulsed field shot reproducing the actual shape, amplitude and time scale of a plasma disruption is applied. If no quench occurs in the conductors, the operating temperature is increased and the pulse field is repeated till a quench occurs. This procedure is aimed to find the *minimum temperature margin required to withstand an actual plasma disruption at the highest operating current density of ITER*

- ***Copper Segregation***. The conductors carry dc current with background dc field. The operating temperature is set independently in the two conductors for a temperature margin of 0.5 K. A field transient, 65 ms duration, is applied with increasing amplitude till a quench occurs in one conductor. Then the temperature margin is increased in the quenched conductor and the field transient amplitude is increased till a new quench occurs. The transient amplitude is plotted as a field integral (T^2/s) against the temperature margin, obtaining the stability curve for both conductors. From the comparison of the two curves, *the effectiveness of the segregated copper for transient stability is deduced.*

A pre-requisite for the above stability experiments is the accurate assessment of the current sharing temperature, $T_{cs}(I, B)$. This is obtained, together with the $I_c(B, T)$ results, from the dc test runs. A large dc data base of the CICC allows to verify the ***scaling of the dc performance from the strand to the cable***. Over a limited range, the effect of the current rate on the critical current can be investigated.

The ac losses are measured by gas-flow calorimetry on both conductors. The steady state temperature increase of the coolant due to the ac losses is measured for the same ac field amplitude over a range of frequencies. From the obtained loss curve, the coupling currents loss ($n\tau$) is derived. The procedure is repeated as a function of the background field and operating dc current. The object of the ac losses test is to ***investigate $n\tau$ under operating conditions, provide energy calibration for the modeling of the stability test, verify the occurrence of saturation, assess the effect of segregation on coupling loss***.

The Hall sensors at three locations of the winding measure the average current pattern in the cable cross section. Monitoring the Hall signal during a T_{cs} runs allows to observe, if any, ***current unbalance and current re-distribution approaching the critical current.*** A change of the current pattern after a pulse field shot, close and away from the pulse field zone, would be evidence of ***boundary induced coupling currents.***

A stability curve is taken at constant temperature margin as a function of the operating mass flow rate, i.e. coolant speed. Comparing the experimental curve with the analyses carried out for the same operating conditions, it is possible to ***deduce the heat transfer coefficient as a function of the coolant speed.***

The stability results at constant operating temperature vs. operating current are used to look for evidence of ***limiting current for both conductors.*** The duration of the transient can be set to either 65 ms (one period at 15 Hz) or 32 ms (half period at 15 Hz).

C.3 DC Results

Most of the DC test results are obtained in the first half of April 2000. The main aim of the tests is to establish the data base for stability tests, i.e. to assess the operating temperature to obtain the desired temperature margin. The instrumentation during the dc runs is connected in the "N" mode, i.e. with most of the Hall sensors not connected to the data acquisition channels. Other DC test in the "C" mode have been run in late May 2000 The DC results include:

T_{cs} and T_q results (at four Sultan field setting and three operating current)
I_c and I_q results (at two Sultan field setting and six operating temperature)
I_c vs. current rate (one Sultan field setting, five current ramp rate)
I_c vs. load direction (one Sultan field setting and six operating temperature)

Due to the saddle shape of the SULTAN field along Z, axis of the SULTAN bore, see Fig. 12 in section B-4, the quench location in dc mode should always occur at the major peak field, Z = -230 mm, where T1 and T2 are placed, see Fig. 14 in section B-4. However, a temperature gradient is observed along the conductors, with major peak field temperature lower than minor peak field temperature (T1 < T7 and T2 < T8). Far from the current sharing, the marginal temperature difference, T7 - T1 ≈ 0.1 K, is not sufficient to offset the field difference and the quench occurs at T1 and T2 (major peak field). This is what normally happens during I_q runs, when the current is raised at the rate of 50 A/s.

Table 5 Background field at the crucial conductor locations

Nominal set/location	Z = 0, R = 200	Z = -230, R = 200	Z = 220, R = 200
	Saddle	Major peak	Minor peak
Temperature sensors	T3 and T4	T1 and T2	T7 and T8
11 T	**10.635**	**11.36**	**11.10**
10 T	**9.71**	**10.35**	**10.12**
9.6 T	**9.31**	**9.93**	**9.71**
10.5 T	**10.18**	**10.88**	**10.635**

During the T_{cs} runs, the operating temperature is slowly raised at constant current and the conductors at the "high field" location are in current sharing mode during a time much longer than the travel from T1 to T7 (about 10 s). Under these conditions, T7 - T1 may increase above 0.3 K, offsetting the field difference between T7 and T1. Then the quench during the T_{cs} runs mostly occurs at the minor peak field, but the voltage at the major peak field is large enough to assess T_{cs} at both locations. The dc runs are taken at four setting of the SULTAN field. The actual background field at the relevant locations of the winding are gathered in Table 5. The self-field is always neglected, i.e. the word "field" always means only "background field".

The joint and termination resistance at low temperature (≈ 4.5 - 5 K) and 10 kA operating current is summarized below. The joint (160 mm long) has obviously higher resistance than the termination (420 mm long). The higher resistance of Termination B compared to A is likely due to an accidental manipulation during the dismantling after the heat treatment. At the largest background field, the average field at the joint is 5-6 T, at the termination less than 2 T. The heating power of the joint (about 2 W at the highest field and current) loads twice as much conductor A than B, possibly due to either non-homogeneous heat generation or coolant stream in the joint box.

	0 background field, 10 kA	Highest field, 10 kA
Joint	2.9 nΩ	13.2 nΩ (5-6 T)
Termination A	1.2 nΩ	1.8 nΩ (< 2 T)
Termination B	1.8 nΩ	2.4 nΩ (< 2 T)

C.3.1 Current sharing temperature, T_{cs}

The current sharing and quench temperature, T_{cs} and T_q, are measured at four operating current level (5, 8, 10 and 12 kA), at the four nominal sets of SULTAN field (see above) and two conductors, for a total of 30 runs. At constant background field, the operating current is increased to the set value at a rate of 100 A/s and then the operating temperature is slowly raised till a quench occurs in one of the conductor. Afterward, the run is repeated with unbalanced operating temperature in the two conductors, in order to quench the "other" conductor. The thermal runaway is not interrupted and all the runs always end with a current dump. In most of the runs, the quench occurs at the minor peak field location, but a T_{cs} assessment is made also at the major peak location.

From the voltage taps surrounding the peak field locations, it is observed that the electrical field has very little gradient over 1.5 m, confirming that the field is homogeneous over one turn of the winding. The quench is found to start always at the 63 cm long voltage tap pairs, which enclose the temperature sensors (V11-V13 for T1, V12-V14 for T2, V31-V33 for T7 and V32-V34 for T8), i.e. in good agreement with the predicted location of either major or minor peak field.

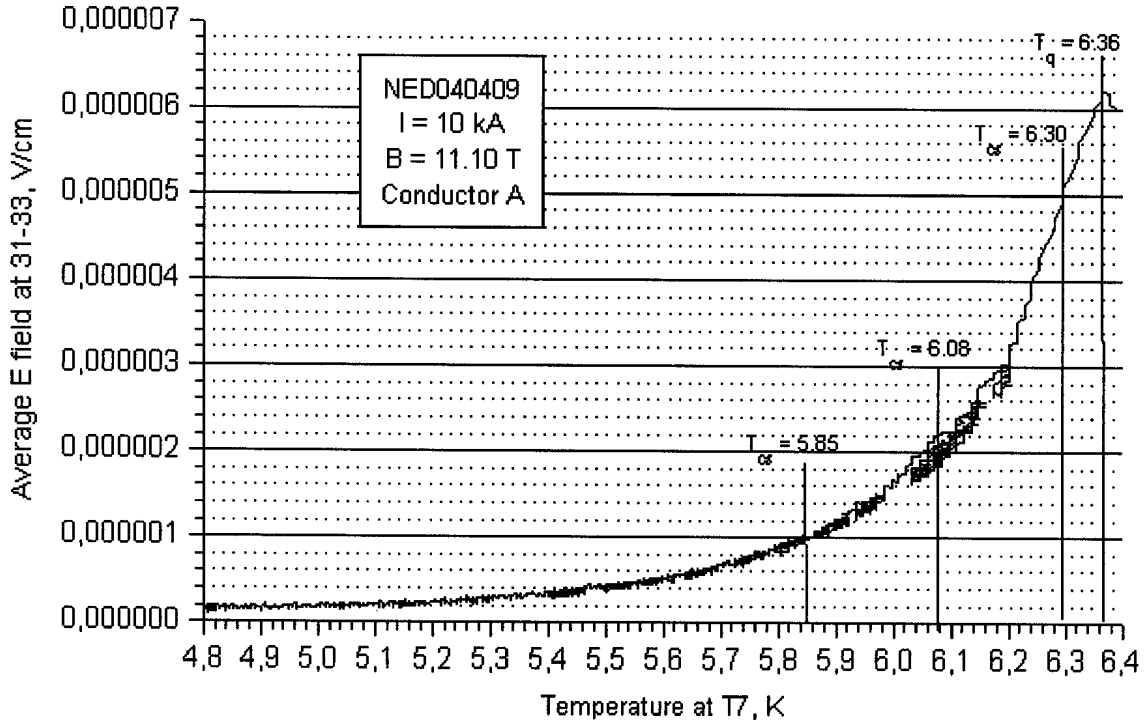

Fig. 8 Assessment of T_{cs} and T_q by electrical field threshold and eventually runaway

The threshold for the runaway depends on the operating current, ranging from ≈ 4 μV/cm at 12 kA up to more than 10 μV/cm at lower current. To assess T_{cs} and T_q, the electrical field at the quench location is plotted against the temperature at the quench location, see Fig. 8. No compensation is done for the voltage offset in the data acquisition channel measuring the electrical field: generally, the offset is < 0.05 μV/cm. Three electrical field criteria (1, 2 and 5 μV/cm) are used to assess T_{cs}, with resolution of the order of 0.02 K.

Both conductors are stable in the investigated range of current. An unstable take-off, at electrical field 0.8 μV/cm, is only observed at the very first charge of the winding (5 kA, 11.36 T, file NED040401), possibly due to a settling of the winding cylinder in the facility. The temperature is raised by powering the main heater H_0 (attached to the pipe before the He inlet) and the high field heater, either H_1or H_2 (attached to the conductor jacket, 1.5 m before the major peak field). The electrical field vs. temperature curve is fully reversible up to 3-4 μV/cm, with negligible hysteresis, see Fig. 8, between 6.0 and 6.2 K. Small temperature oscillations (density waves) are observed, mostly at T > 7 K, with an amplitude in the range of 0.2 K and period of 10 to 20 seconds (see section B-4). The voltage taps react at such temperature waves, which can be treated as micro-slugs, see Fig. 9.

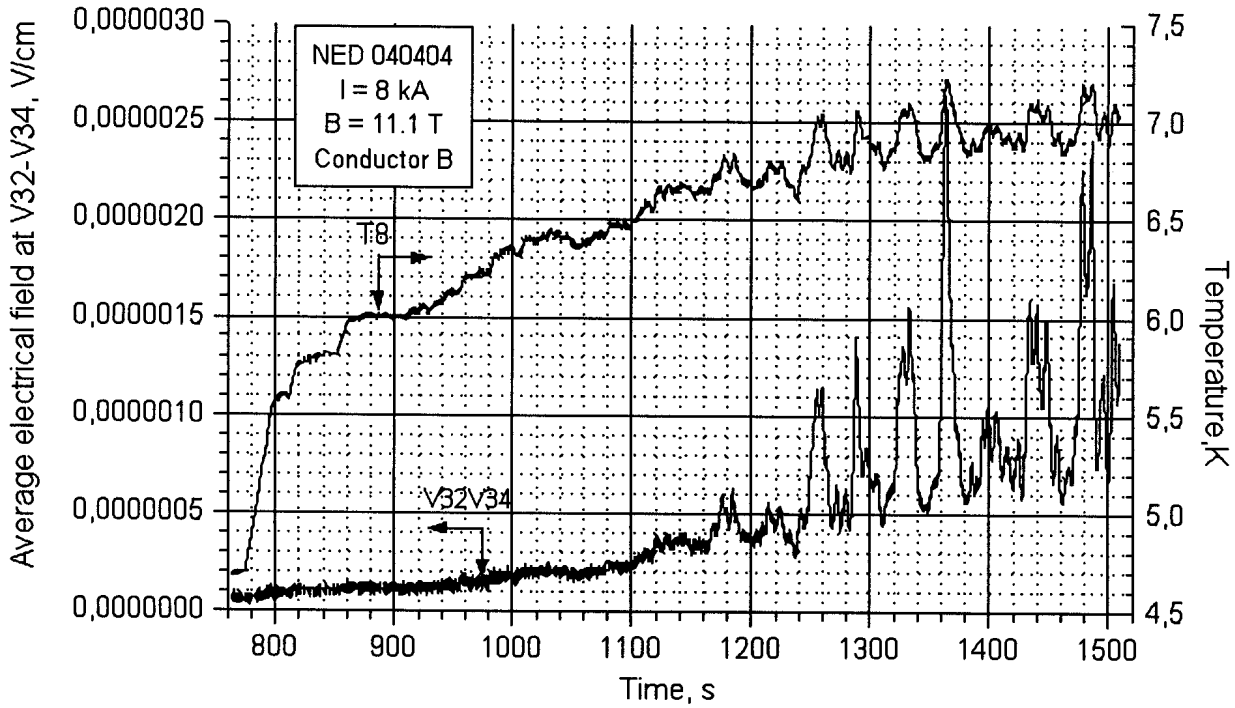

Fig.9 Example of correlation between temperature oscillations (micro-slugs) and electrical field change, during a T_{cs} test run, before quench

The T_q results (start of the runaway) are less accurate than the T_{cs} results. At the runaway, the voltage evolves very fast, but the response of the temperature sensors is slow, with time constant in the range of 1 s, see also section C.3.2. The value of T_q may also depend on the imposed mass flow rate, i.e. heat removal rate, which can slow down the thermal runaway. For T_{cs} measurements, the slow response is not significant as quasi steady state conditions apply: The accuracy for T_{cs} results is in the range of 0.02 K For T_q, the accuracy drops to about 0.1 K.

All the T_{cs} and T_q results are summarized in Table 6. The T_{cs} results for 1 μV/cm criteria are plotted in Fig. 10 (conductor A) and Fig. 11 (conductor B). The quench occurs clearly only at one location (mostly the minor peak field), but the voltage is growing at the same time also at the other field peak and T_{cs} @ 1 μV/cm can be assessed at both locations (major and minor field peaks). The scattering of the T_{cs} results is worse for conductor A (Fig. 10), were the results taken at the major peak field are systematically lower than at the minor peak field.

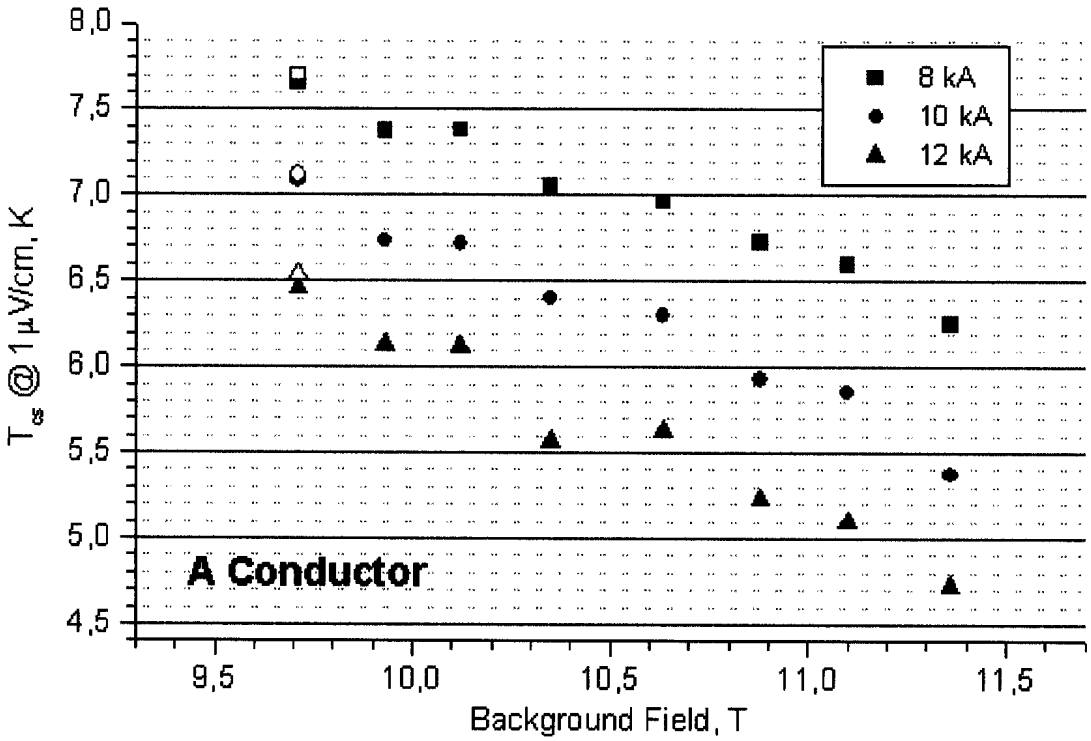

Fig. 10 Current sharing temperature results for conductor A at 1μV/cm

These last results are plotted as empty symbols in Fig. 10 and 11. The agreement with the initial T_{cs} results (after over hundred cycling loads and reversing twice the load direction) is satisfactorily within 0.05 K.

The behavior of T_{cs} as a function of the electrical field criterion is shown in Fig.12 for the B = 11.1 T and I = 10 kA. At first glance, conductor B has superior performance compared to A. However, this turned out to be an effect of the load direction (see section C.3.3).

C.3.2 Critical current, I_c

The critical current is measured as a function of the operating temperature, with a ramp rate of 50 A/s, at two sets of SULTAN background field, 11 and 10 T. The quench occurs always at the major peak field, i.e. 11.36 and 10.35 T. The critical current, I_c, is assessed for three electrical field criteria: 0.5, 1 and 2 μV/cm. The voltage taps signal (V11V13 for conductor A and V12V14 for conductor B) is divided by the length (63 cm) and the inductive signal due to the current ramp (0.14-0.16 μV/cm) is subtracted.

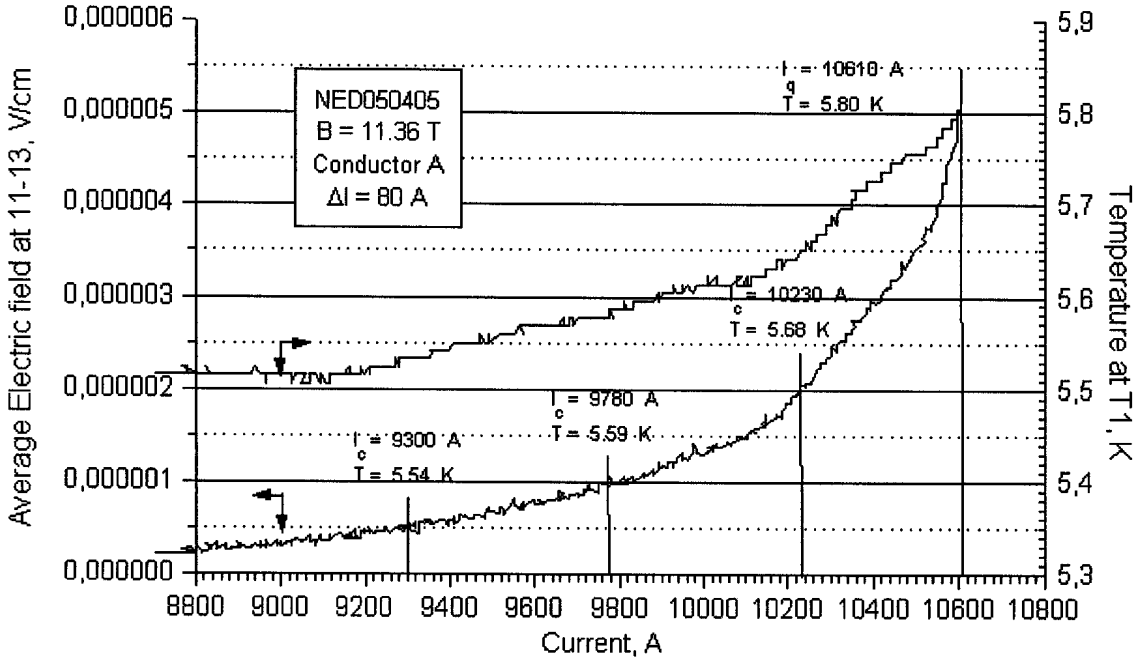

Fig. 13 Assessment of I_c and I_q vs. T for a run with smooth temperature increase

The critical current at the various electrical field criteria is assessed by plotting the electrical field vs. the operating current. The operating temperature drifts from the begin of the ramp because of the joint losses (the joint is cooled in series with the conductors) and, at the end of the ramp, due to the current sharing heating. The temperature of the closest sensor (either T1 or T2) is plotted on the right Y-axis of the graph: an individual operating temperature is associated to each I_c result, see Fig. 13. When the temperature increase is very small and smooth, the "time delay" between voltage and temperature can be neglected. In few cases, when the temperature has oscillations in the current sharing range, a small correction ($\leq 1\%$) must be done on the current to account for the "time delay" between voltage and temperature. For the quench current, I_q, no correction is done. The accuracy of the I_q results (as for the T_q results) is poorer compared to I_c.

All the I_c results are summarized in the Table 7, together with the operating mass flow rate and the operating temperature associated to each I_c results. The summary plots at 11.36 T, with the three I_c criteria and I_q are gathered in Fig. 14 (conductor A) and Fig. 15 (conductor B). The T_{cs} results at 11.36 T (see Table 6) are also added as empty symbols in the I_c charts. The I_c and T_{cs} results for A and B at 1 μV/cm, 10.35 T are summarized in

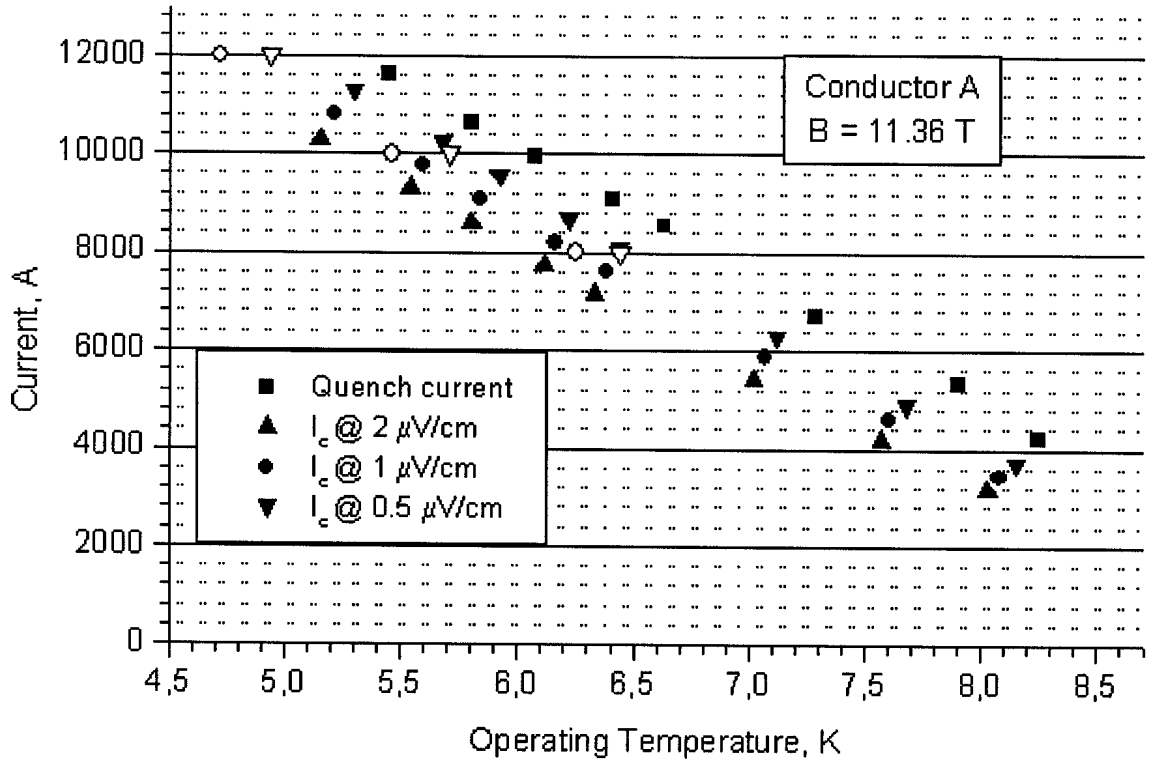

Fig.14 DC results at 11.36 T for conductor A: I_c are full symbols, T_{cs} are open symbols

Fig. 16. The excellent agreement of the two independent sets of results proves that the accuracy is good (the comparison of I_q and T_q in former, short length samples was mostly problematic, possibly due to temperature gradients building in the CICC with central hole). The n factor is assessed from the I_c plots for electrical field < 1 μV/cm. The non-strictly constant temperature limits the accuracy of the evaluation. The range of n for both conductors is 13-15, compared to ≈ 30 in the strand. The lower n in cabled conductors compared to the strands is a consequence of the higher transverse resistance, which opposes the adjustment of the current density to the self-field profile, due to the twist of the cable elements.

Table 7. Critical current results at constant current rate 50 A/s

File name	*Field*	*dm/dt*	*Con*	*I_c @ 0.5 μV/cm*	*I_c @ 1 μV/cm*	*I_c @ 2 μV/cm*	*I_q*
NED 050402	11.36	3.9	A	10280 A / 5.15 K	10800 A / 5.21 K	11280 A / 5.30 K	11610 A / 5.45 K
NED 050403	11.36	3.8	B	11080 A / 562 K	11500 A / 5.69 K	11800 A / 5.80 K	12000 A / 5.88 K
NED 050404	11.36	3.7	A	8600 A / 5.80 K	9070 A / 5.84 K	9560 A / 5.92 K	9960 A / 6.07 K
NED 050405	11.36	3.8	A	9300 A / 5.54 K	9780 A / 5.59 K	10230 A / 5.68 K	10610 A / 5.80 K
NED 050406	11.36	3.5	B	9440 A / 6.18 K	9870 A / 6.23 K	10260 A / 6.33 K	10420 A / 6.46 K
NED 050407	11.36	3.5	A	7160 A / 6.33 K	7620 A / 6.38 K	8080 A / 6.44 K	8540 A / 6.63 K
NED 050408	11.36	3.6	A	7720 A / 6.11 K	8200 A / 6.16 K	8680 A / 6.22 K	9100 A / 6.41 K
NED 050409	11.36	3.2	B	7580 A / 6.79 K	7980 A / 6.83 K	8360 A / 6.90 K	8600 A / 7.08 K
NED 050410	11.36	3.2	A	5410 A / 7.02 K	5880 A / 7.07 K	6290 A / 7.12 K	6720 A / 7.29 K
NED 050411	11.36	2.9	B	5760 A / 7.41 K	6240 A / 7.45 K	6480 A / 7.53 K	6780 A / 7.75 K
NED 050412	11.36	2.9	A	4190 A / 7.57 K	4590 A / 7.60 K	4880 A / 7.68 K	5320 A / 7.90 K
NED 050413	11.36	2.7	B	4340 A / 7.94 K	4900 A / 7.95 K	5080 A / 8.08 K #	5420 A / 8.14 K
NED 050414	11.36	2.7	A	3160 A / 8.03 K	3440 A / 8.08 K	3700 A / 8.15 K	4200 A / 8.25 K
NED 050415	11.36	2.3	B	2850 A / 8.60 K	3310 A / 8.62 K	3500 A / 8.73 K	3750 A / 8.76 K
NED 060409	10.35	3.1	A	10090 A / 6.16 K	10670 A / 6.23 K	11060 A / 6.30 K	11410 A / 6.45 K
NED 060410	10.35	2.9	A	8740 A / 6.60 K	9230 A / 6.66 K	9670 A / 6.73 K	9970 A / 6.85 K
NED 060411	10.35	2.8	A	7520 A / 7.01 K	8020 A / 7.10 K	8480 A / 7.14 K	8690 A / 7.32 K
NED 060412	10.35	2.6	A	6280 A / 7.45 K	6860 A / 7.46 K	7200 A / 7.59 K	7590 A / 7.74 K
NED 060413	10.35	2.5	A	5360 A / 7.82 K	5700 A / 7.85 K	6070 A / 7.93 K	6380 A / 8.11 K
NED 060414	10.35	2.3	A	4240 A / 8.25 K	4650 A / 8.27 K	5020 A / 8.35 K	5270 A / 8.55 K
NED 060415	10.35	2.2	A	3570 A / 8.56 K	3860 A / 8.61 K	4020 A / 8.70 K	4340 A / 8.84 K
NED 060416	10.35	3.0	B	11100 A / 6.49 K	11520 A / 6.56 K	11800 A / 6.65 K	11980 A / 6.75 K
NED 060417	10.35	2.9	B	9750 A / 6.88 K	10220 A / 6.96 K	10460 A / 7.04 K	10650 A / 7.13 K
NED 060418	10.35	2.7	B	8470 A / 7.28 K	8860 A / 7.34 K	9100 A / 7.42 K	9320 A / 7.53 K
NED 060419	10.35	2.5	B	7040 A / 7.68 K	7500 A / 7.76 K	7780 A / 7.85 K	7960 A / 7.93 K
NED 060420	10.35	2.4	B	5630 A / 8.18 K	5770 A / 8.32 K #	6220 A / 8.35 K	6350 A / 8.45 K
NED 060421	10.35	2.3	B	4420 A / 8.58 K #	4860 A / 8.62 K #	4940 A / 8.73 K #	5260 A / 8.73 K
NED 060422	10.35	2.2	B	3660 A / 8.91 K	3780 A / 9.09 K	3890 A / 9.13 K	4200 A / 9.16 K

Large heat slug. I_c assessed on the E raise at the start of the slug

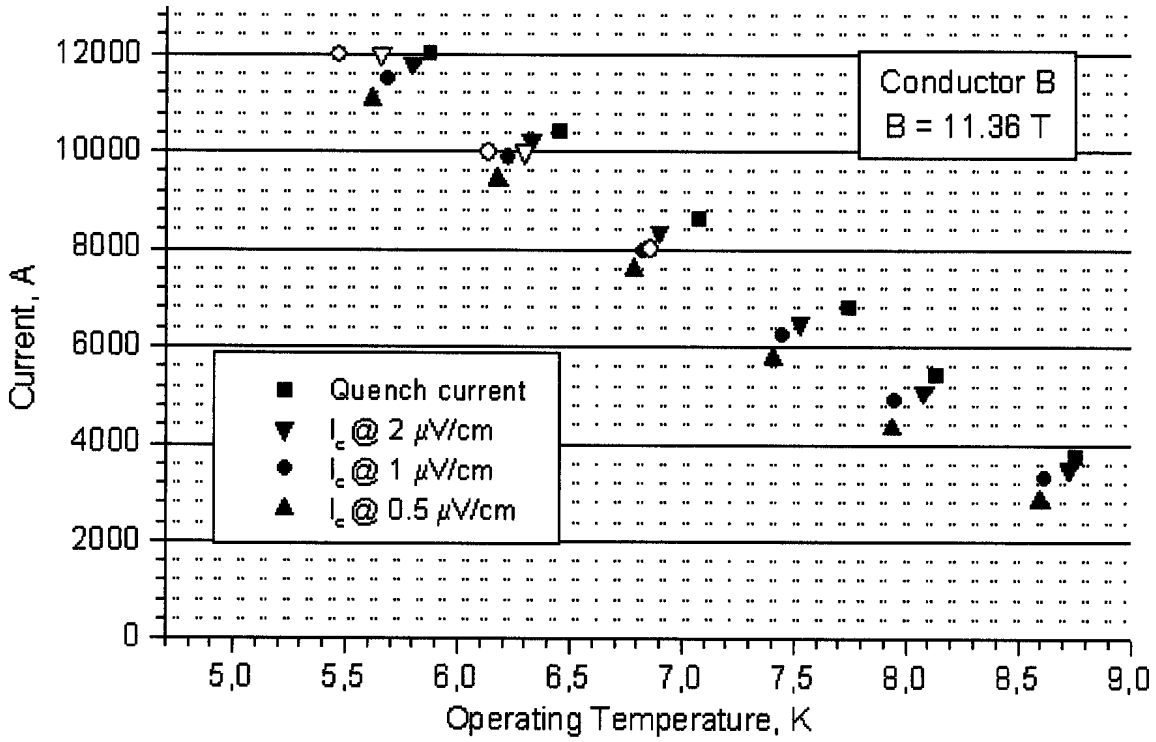

Fig.15 DC results at 11.36 T for conductor B: I_c are full symbols, T_{cs} are open symbols

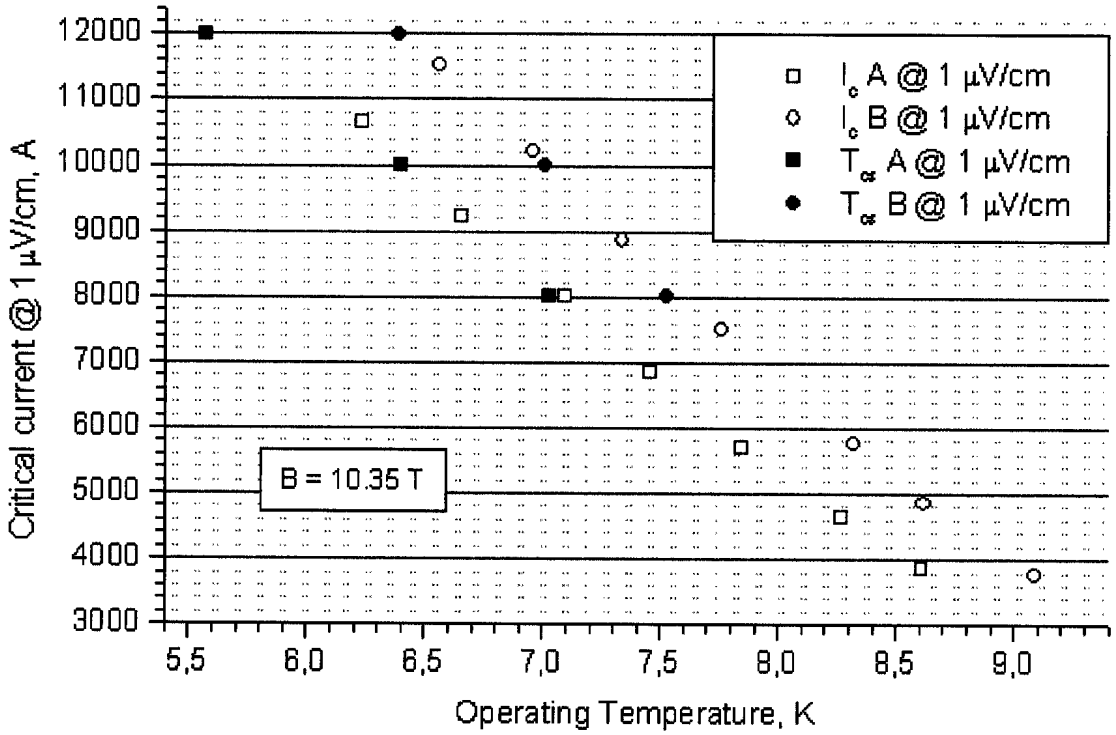

Fig.16 Summary of dc results at 10.35 T, 1μV/cm for conductor A and B: I_c and T_{cs}

C.3.3 Critical current versus load direction

In the standard configuration of the power supply, the conductor A is connected to the positive lead and conductor B to the negative one, see also Fig. 14 section B-4. The magnetic field of SULTAN loads inward the turns of conductor A and outward the conductor B. After completing the above dc characterization, the plus and minus leads of the power supply have been switched and the I_c test vs. temperature has been repeated at the SULTAN setting of 10 T. Due to the geometry of the winding, the conductor A, former loaded in compression, is now loaded in tension. The pre-loaded steel clamps are designed to avoid conductor stretching and maintain the same strain in jacket of both conductors. However, a minor change of the strain state of the strands is possible, due to minor displacement of the center of the cable inside the jacket under the Lorentz forces. For example, a displacement of the cable by 0.1 mm in radial direction turns into an axial strain of 0.05%, which either adds or subtracts to the large compressive strain of the superconductor (range of -0.7%) from the differential contraction of steel and Nb_3Sn.

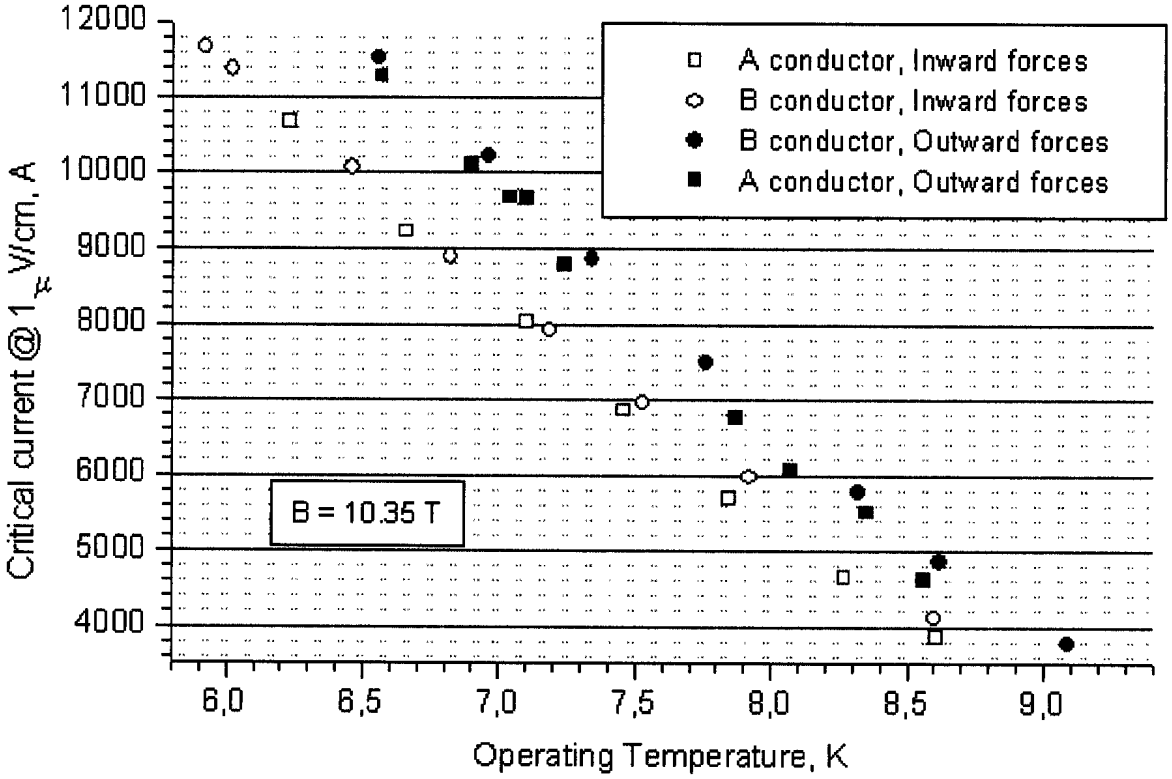

Fig. 17 Summary of I_c results for A and B at 10.35 T, with both inward and outward forces

Table 8. I_c (T) results at Reverse Polarity, B = 10.35 T, current rate 50 A/s

File name	*Con*	*I_c @ 0.5 μV/cm / T*	*I_c @ 1 μV/cm / T*	*I_c @ 2 μV/cm / T*	*I_q / T*
NED140401	B	9590 A / 6.10 K #	10040 A / 6.15 K #	10430 A / 6.21 K #	10660 A / 6.40 K #
NED140402	B	11110 A / 5.86 K	11660 A / 5.92 K	12070 A / 6.02 K	*
NED140403	B	10850 A / 5.95 K	11370 A / 6.02 K	11800 A / 6.11 K	*
NED140404	B	9490 A / 6.40 K	10070 A / 6.46 K	10490 A / 6.55 K	10800 A / 6.69 K
NED140405	B	8460 A / 6.79 K	8890 A / 6.82 K	9330 A / 6.92 K	9710 A / 7.11 K
NED140406	B	7460 A / 7.14 K	7920 A / 7.19 K	8330 A / 7.25 K	8600 A / 7.39 K
NED140407	B	6490 A / 7.49 K	6970 A / 7.53 K	7330 A / 7.71 K	7540 A / 7.87 K
NED140408	B	5500 A / 7.87 K	5980 A / 7.92 K	6300 A / 7.93 K	6450 A / 8.21 K
NED140409	B	3800 A / 8.54 K	4120 A / 8.60 K	4530 A / 8.68 K	4780 A / 8.82 K
NED140410	A	4490 A / 8.48 K	4630 A / 8.56 K	4790 A / 8.67 K	5260 A / 8.75 K
NED140411	A	5240 A / 8.20 K	5510 A / 8.35 K	5860 A / 8.33 K	6030 A / 8.51 K
NED140412	A	5590 A / 8.07 K	6060 A / 8.07 K	6280 A / 8.18 K	6640 A / 8.31 K
NED140413	A	6460 A / 7.79 K	6760 A / 7.87 K	7230 A / 7.92 K	7490 A / 8.09 K
NED140414	A	9580 A / 6.86 K	10120 A / 6.90 K	10480 A / 6.99 K	10760 A / 7.15 K
NED140415	A	9200 A / 6.99 K	9680 A / 7.04 K	10090 A / 7.10 K	10400 A / 7.32 K
NED140416	A	9210 A / 6.96 K	9670 A / 7.10 K	9980 A / 7.12 K	10400 A / 7.32 K
NED140417	A	10760 A / 6.52 K	11280 A / 6.57 K	11650 A / 6.66 K	11930 A / 6.81 K
NED140418	A	8300 A /7.19 K	8800 A / 7.24 K	9100 A / 7.34 K	9440 A / 7.54 K

 # First run of the day. Results clearly lower than later runs. Discarded for plots

** The ramp up to 12 kA was completed without quench. A quench occurred later at the minor peak field location*

The new set of I_c results (named "reverse polarity") is gathered in the Table 8. The results at 1 μV/cm criterion are plotted in Fig. 17 together with the results of Table 7. The critical current with outward load is about 19% higher than in inward direction. For the same load configuration, conductor A and B have very similar I_c results. A quantitative comparison of the dc performance of conductor A and B is done in Fig.18, with the straight ratio of $I_c(B)/I_c(A)$ at both inward and outward loads. The ratio is very close to 1, i.e. the conductor supplier managed to prepare the two cable layouts with the same dc performance. From Fig.17 and Fig.18, it is evident that conductor B has slightly higher performance at higher temperature, as it is expected from the slightly different scaling parameters, see Table 3. How far the conductors have the same dc performance is not

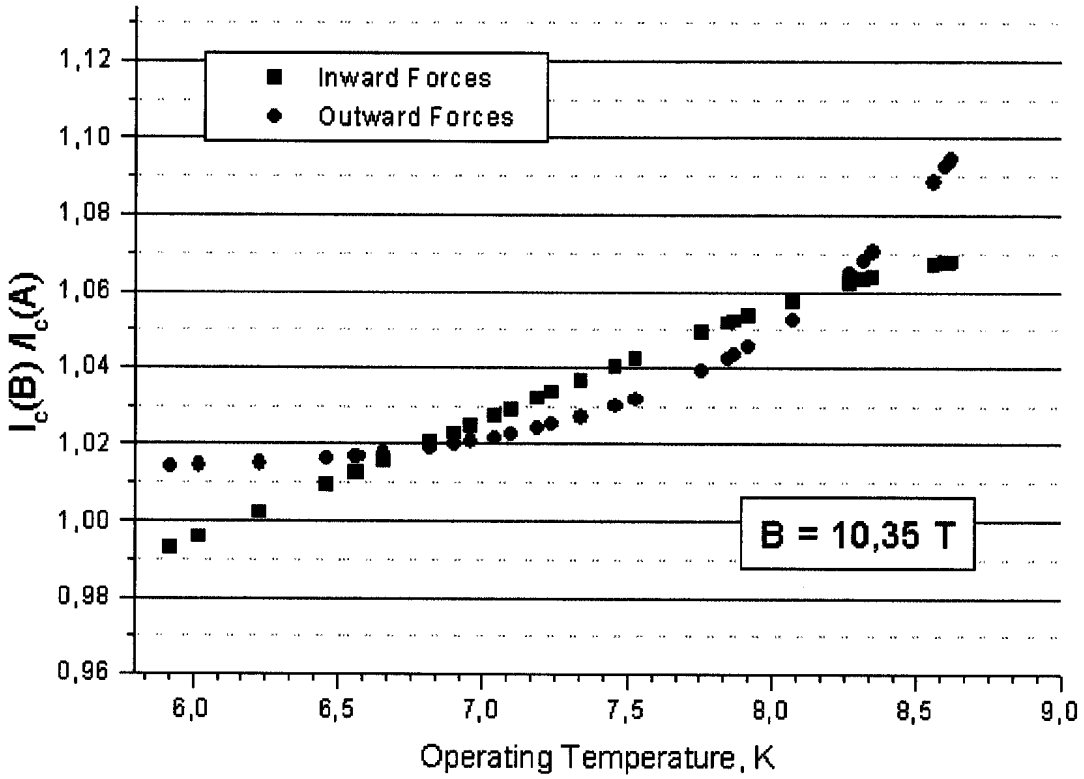

Fig. 18 Comparison of B vs. A dc performance for both inward and outward forces

relevant for the stability experiment as the operating temperature, and hence the temperature margin, is adjusted individually in the two conductors.

The polarity of the winding was reversed once more before starting the stability runs and the I_c test was carried out again to verify that no significant hysteresis occurred after changing the load direction. The results are reported as empty symbols in Fig. 14 and 15. The new results match satisfactorily the curves taken before switching the load direction.

C.3.4 Strand to CICC scaling of dc performance

The scaling law parameters T_{c0m}, B_{c20m} and C_0 from Table 3 can be used to scale the dc performance of the strand to the cable. The strain of the Nb_3Sn filaments, ε, must be reset from the intrinsic strain, $\varepsilon_0 = -0.25\%$ in the strand test, to the operating strain in the cable-in-conduit conductors, which includes the thermal load from the differential shrinking of jacket and cable, as well as the operating strain from the Lorentz forces.

The voltage vs. current characteristic, i.e. the *n* factor, is different in a single strand test compared to a large, cabled conductor, due to the amplitude of the self field, the pitch, the transverse resistance and, whenever applicable, the current distribution. As *n* is different, the result of the performance comparison depends on the retained I_c criterion, e.g. 0.1 μV/cm, 1 μV/cm or "take-off". In the case of SeCRETS, *n* decreases from $\approx$ 30 (strand test) to $\approx$ 15 (CICC test). In the following discussion, the strand-to-cable comparison is done at the fixed criterion of 1 μV/cm, arbitrarily burying the *n* factor differences in a correction of the C_0 parameter. This procedure is a first order approach.

The C_0 of Table 3, assessed for the 0.1 μV/cm criterion, is corrected to the 1 μV/cm criterion according to the *n* factor of the strand: $C_0(1\ \mu V/cm) = C_0(0.1\ \mu V/cm)\cdot k_n$ with k_n = 1.0857 for both A and B. Another correction on C_0 needs to be done to scale the witness strands results to the average strand result, as reported in the quality assurance sheets. In this correction, named k_{av}, we also bury the discrepancy between the VNIINM and UT results, assuming arbitrarily that the strain from the sample holder of VNIINM is ε = -0.25%. Eventually, the C_0 coefficient for the strands in the CICC turns to be the one from the strand test (Table 3) multiplied by $k_n \cdot k_{av}$, i.e. 1.176 and 1.212 respectively for A and B.

The strain of the strands in the CICC is the sum of two terms, one from thermal contraction in the range of -0.7% and the other, proportional to *IxB*, from the operating load: $\varepsilon = \varepsilon_{th} + \varepsilon_{load} I \times B$. As the total strain is a function of the operating current, each test point in Fig. 17 has a different strain. A limited range of variation has been allowed to the terms ε_{th} and ε_{load} (identical for A and B) to fit the experimental results, leading to ε_{th} = -0.68 and $\varepsilon_{load} = \pm 3.86 \cdot 10^{-7}$, see Table 9. The critical current results of conductors A and B with the fitting curves according to the strand scaling law from the parameters in Table 9 are shown in Fig. 19 and 20. No self-field correction has been done, i.e. the reported field B = 10.35 T is the SULTAN background field at the location of the quench.

Table 9 Scaling law parameters for the strands in the CICC

	A	**B**
T_{com} [K]	17.3	17.7
B_{c20m} [T]	32.65	32.80
$C_0^* = C_0 \cdot k_n \cdot k_{av}$ [A·T/m^2]	$7.75 \cdot 10^9$	$7.515 \cdot 10^9$
Operating strain [%]	$\varepsilon = \varepsilon_{th} + \varepsilon_{load} I \times B = -0.68 \pm 3.86 \cdot 10^{-7} IB$	

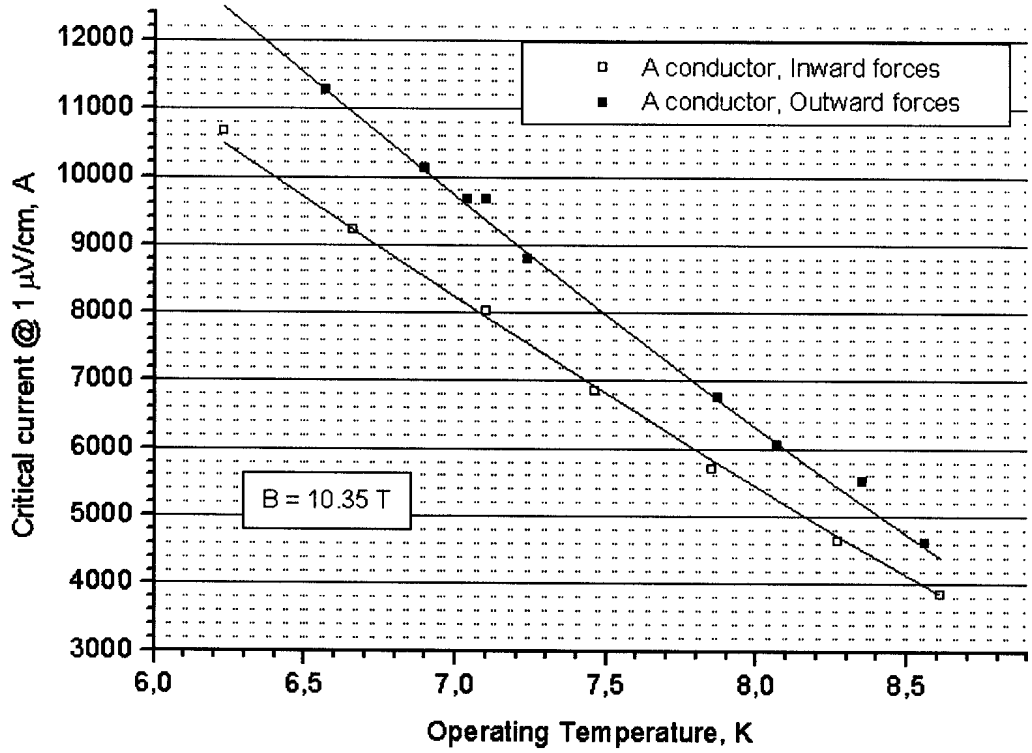

Fig. 19 The A conductor results fitted with the parameters in Table 9

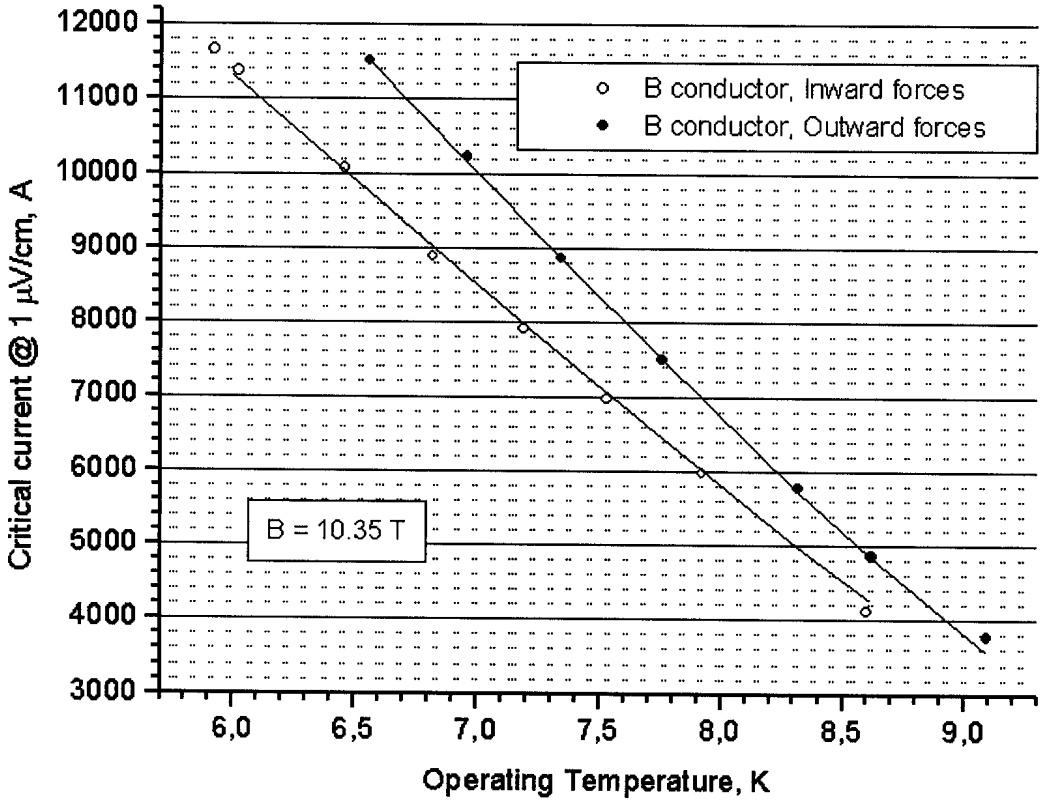

Fig. 20 The B conductor results fitted with the parameters in Table 9

The scaling of the dc performance from strand to CICC is satisfactory, i.e. the critical current of the cabled conductor corresponds to the sum of the critical current of the individual strand, without substantial discrepancy. The availability of two load conditions (outward and inward forces) allows to assess the overall strain with good accuracy, opposite to most of the Nb_3Sn CICC test, where the strain is widely abused as a fitting parameter. The assessment of C_0 is based on the simplifying assumption of identical n factors for cable and strand. If the comparison would be done at another E field criterion, e.g. 0.5 or 2 μV/cm, by adjusting $k_n(E)$, a second order correction may be necessary.

C.3.5 Critical current versus ramp rate

The current rate at the 12 kA power supply can be set in the range of 25 to 1600 A/s. A number of I_c test have been carried out for both A and B conductors, as a function of the current rate, at the same temperature setting. According to the current rate, the electric field from the voltage taps must be compensated for the inductive voltage, $E_{ind} = 2.8 \cdot 10^{-9} (dI/dt)$ *V/cm*. The "delay" (see above) between temperature and electric field signals becomes critical at high current rate, as the current (and voltage) increases in non-negligible way in the time scale of the response of the temperature sensor. However, as the heater and mass flow rate have an identical setting, the temperature is assumed to be identical in all the runs within 0.1 K. The reference temperature is 7 K.

It turns out that up to 400 A/s the I_c threshold can be clearly assessed. At 800 A/s, a quench discharge is triggered before the electric field at the voltage taps achieve the 1 μV/cm threshold. This seems to be due to the quench detection threshold, which includes the inductive fraction of the voltage, rather than to a real conductor quench. Another problem occurring at 800 A/s is the fast signal evolution: the low pass filters at the voltage taps and the 100 ms sampling rate of the DAS become a limiting factor for accuracy. In principle, test at 800 and 1600 A/s could be done resetting the quench detection threshold, using the fast DAS (e.g. 5 ms sampling rate) and removing the filters to the voltage taps. However, this is out of the scope of SeCRETS.

The I_c results vs. *dI/dt* up to 400 A/s (≈13 A/mm^2·s non-Cu) are shown in Fig. 21 for conductor B at 10.35 T, 7 K. The change of I_c is marginal, ± 1.5% and can be buried in the accuracy of the measurement (i.e. the accuracy of the temperature setting). Beside the current rate, Fig. 11 also shows the non-Cu current density rate, which can be easily scaled to other conductor size and applications. For example, the peak non-Cu current density rate in the ITER CS is -27 A/s·mm^2.

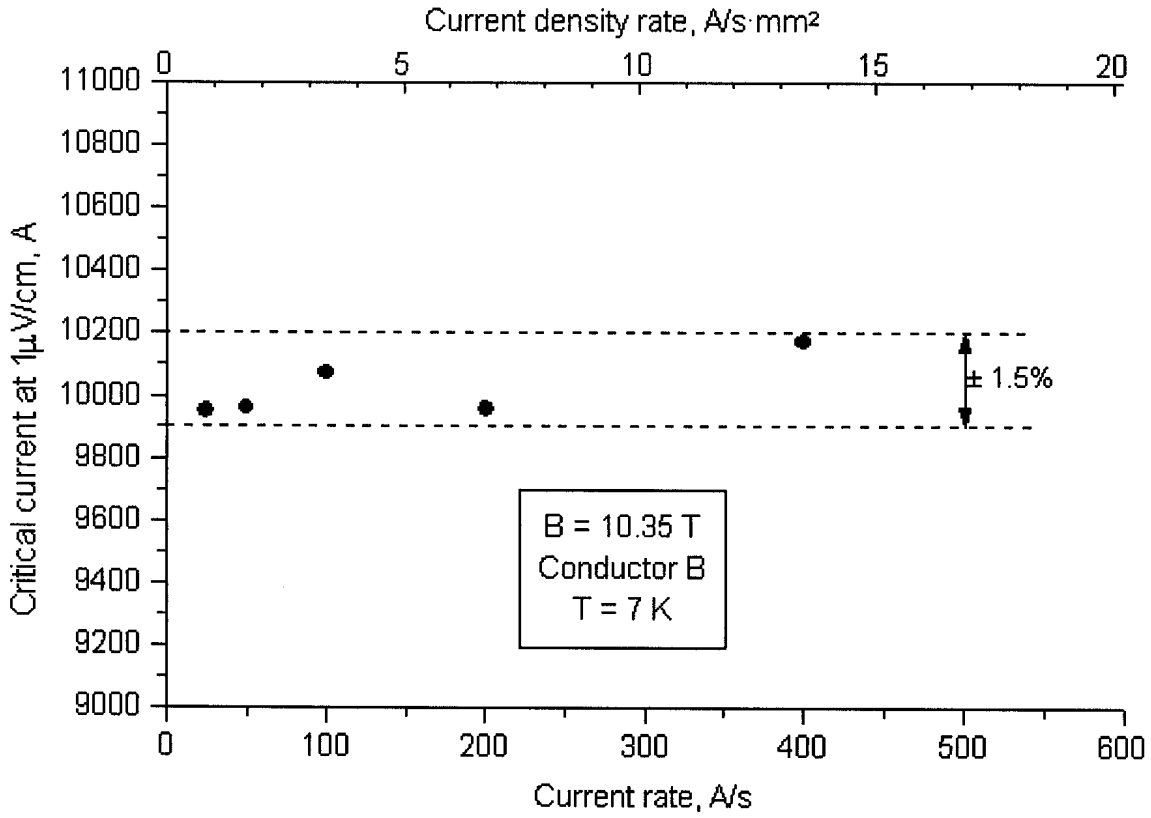

Fig. 21 Critical current vs. current rate

C.4 AC Losses

The ac losses in the SeCRETS conductors are measured by gas-flow calorimetry. The temperature at the sensors placed after the pulsed coil increases up to a "steady state" level on the time scale of 2 - 5 s after the start of the ac field, depending on the coolant velocity. From the temperature increase, the enthalpy change of the coolant is calculated at constant pressure and multiplied by the mass flow rate to obtain the power loss.

The pressure at the location of the pulsed coils is assumed to be the average of the values at the inlet and outlet of the winding, where the pressure sensors are placed. The pressure and the mass flow rate in both conductors are measured at each run. As the temperature rise due to the ac losses is very small (range of 0.1 - 0.3 K) no change is observed during the runs and the assumption of constant pressure for the evaluation of the enthalpy change is justified.

The operating mass flow rate is adjusted in the range of 3 to 6 g/s in order to obtain a reasonable temperature increase, neither too large nor too small. The ac field duration is limited by the self-heating of the pulsed coils and depends on the ac field amplitude, i.e. the ac current, and also on the background field, which affects the magnetoresistance of the pulsed coils. For ac field in the range of ± 0.35 T @ 10 T background field, the duration of the pulse is 7 s. The peak temperature of the windings raises shortly up to 50 K and the re-cool time (with a separate cooling circuit) is in the range of 20 minutes. The temperature traces of the conductors after the pulse decrease to the initial values within 3-5 seconds: there is no evidence of heat transfer from the pulsed coils to the SeCRETS conductors. Only the ac losses load is accounted to reduce the data of the gas-flow calorimeter.

The pulsed field coil spans 30 cm of conductor. According to the table 1 of section B, the strand volume for normalization of the losses is 23.29 cm^3 (A) and 23.12 cm^3 (B). The amplitude of the pulse field is monitored by a current meter on the pulsed coils and two Hall sensor at Z = 0, R = 200 (see Fig. 6, section B). Both amplitude and shape of the pulsed field measured by the Hall sensors agree with the input data at the power supply, with no distortion within the 1 ms resolution of the fast data acquisition. The lack of distortion of the pulse shape is a proof that no screening occurs in the loop built by the steel clamp, the steel bolts and the winding cylinder. The proper (series) connection of the three windings is checked by magnetic sensors at room temperature and is confirmed by the agreement between expected and measured field/current ratio.

Two temperature sensors are placed for redundancy downstream of the pulsed coils on each conductor. The actual, absolute accuracy of the sensors is 0.03 K. The relative accuracy for the assessment of the temperature raise is better, in the range of 0.01 K. The minimum frequency for accurate loss results is 2 Hz (at lower frequency, the temperature raise is in the range of 0.03 K and the error bar dramatically increases). The largest ac field frequency for ± 0.35 T is 9 Hz, limited by the voltage available at the power supply.

For a given set of ac amplitude, background field and operating current, a loss curve is obtained from the energy loss per cycle, normalized to the strand volume, plotted versus the frequency of the ac field. From the slope of the loss curve, the coupling currents loss constant, nτ, is drawn, according to the "low frequency" formula for coupling loss, Q_c, in transverse sinusoidal field, $B(t) = \frac{\Delta B}{2}\sin \omega t$.

$$Q_c = \frac{\pi n \tau \omega \Delta B^2}{4\mu_0(\omega^2\tau^2 + 1)} \approx \frac{\pi n \tau \omega \Delta B^2}{4\mu_0} \qquad (1)$$

From the experimental slope of the loss curve, $\alpha = \frac{Q_c}{f}$, the coupling loss constant, nτ, is

$$n\tau = \frac{2\mu_0 \alpha}{\pi^2 \Delta B^2}$$

The accuracy of the nτ assessment from the loss curves is within ± 10%. In the case of easy geometry, e.g. a multifilament strand, the nτ, measured on a limited range of frequency, can be reliably used in a wide range of frequency, $0 < f < 0.03/\tau$, according to eq. (1). In case of more complexes, multistage cables, e.g. CICC, the nτ should be strictly used only in the measured range of frequency. An extrapolation to higher or lower frequency may be affected by substantial error in case of non-linearity of the loss curve, due for example to the superposition of current loops with different time constant and early screening of cable fractions.

C.4.1 AC Loss results

The loss curve at 0 operating current is measured in the background field of 2 and 10 T, for an ac amplitude of ± 0.3 T. As the loss is smaller at high field, the accuracy is poorer. The test at 10 T was repeated later for ± 0.35 T, improving the accuracy. As expected from the test on short sample, see C.1.2, the loss is smaller for conductor B. The ac losses

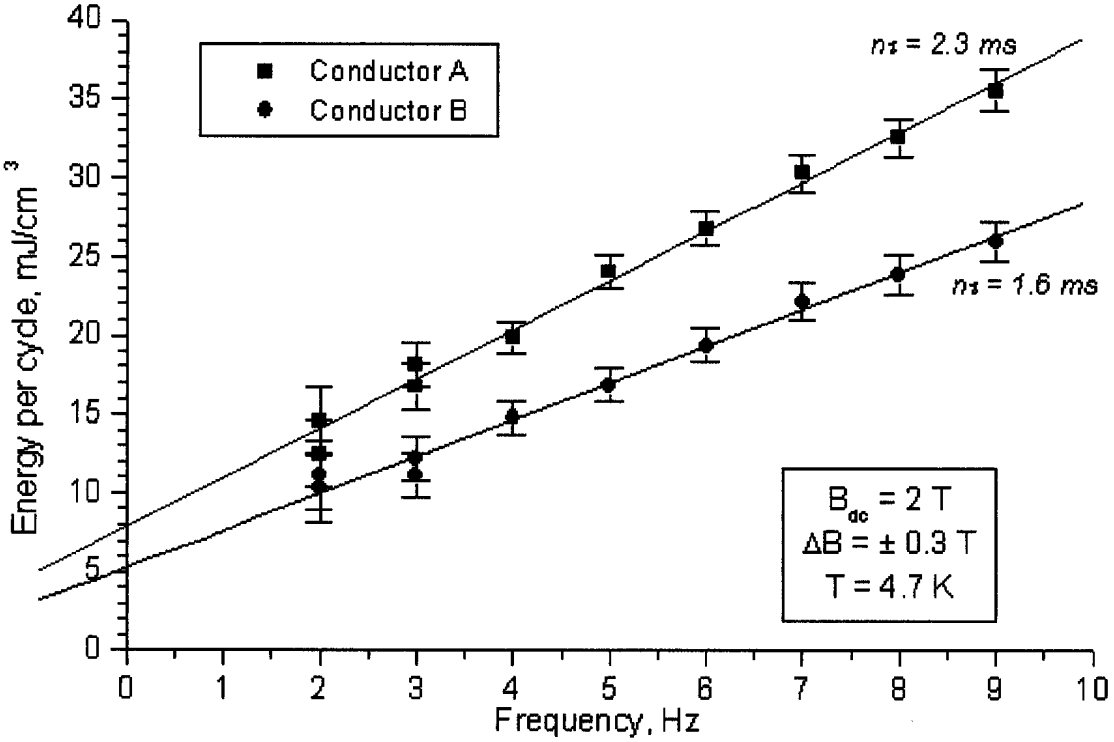

Fig. 22 Loss curve with fitting lines at 2 T background field and 0 transport current

Table 10 Summary of coupling loss results, nτ [ms], at 0 transport current

	A	B
Virgin state, ± 0.4 T, B_{dc}= 0 T (UT test)	15.2 ms	10.4 ms
SULTAN test, ± 0.3 T, B_{dc}= 2 T	2.3 ms	1.6 ms
SULTAN test, ± 0.35 T, B_{dc}= 10 T	1.45 ms	1.14 ms

test is carried out after the dc test, i.e. after about 100 cycles of transverse loading. This explains the drop of nτ compared to the test in the "virgin state". The results at 2 T are plotted in Fig. 22. All the results at 0 current are summarized in Table 10. The contribution of the interstrand coupling currents, if any, is marginal.

At the background field of 10 T, the loss curves are taken also at 6 and 12 kA dc operating current, in the range of 2 to 8 Hz, see Fig. 23. The loss curves are linear in the test range. The loss increase, from 0 to 12 kA (400 A/mm^2) is about a factor of 2.

In the full size CS1 conductor, in the same range of frequency, the loss at high field, 0 transport current was comparable (nτ ≈ 1.5 ms), but the loss increase with operating

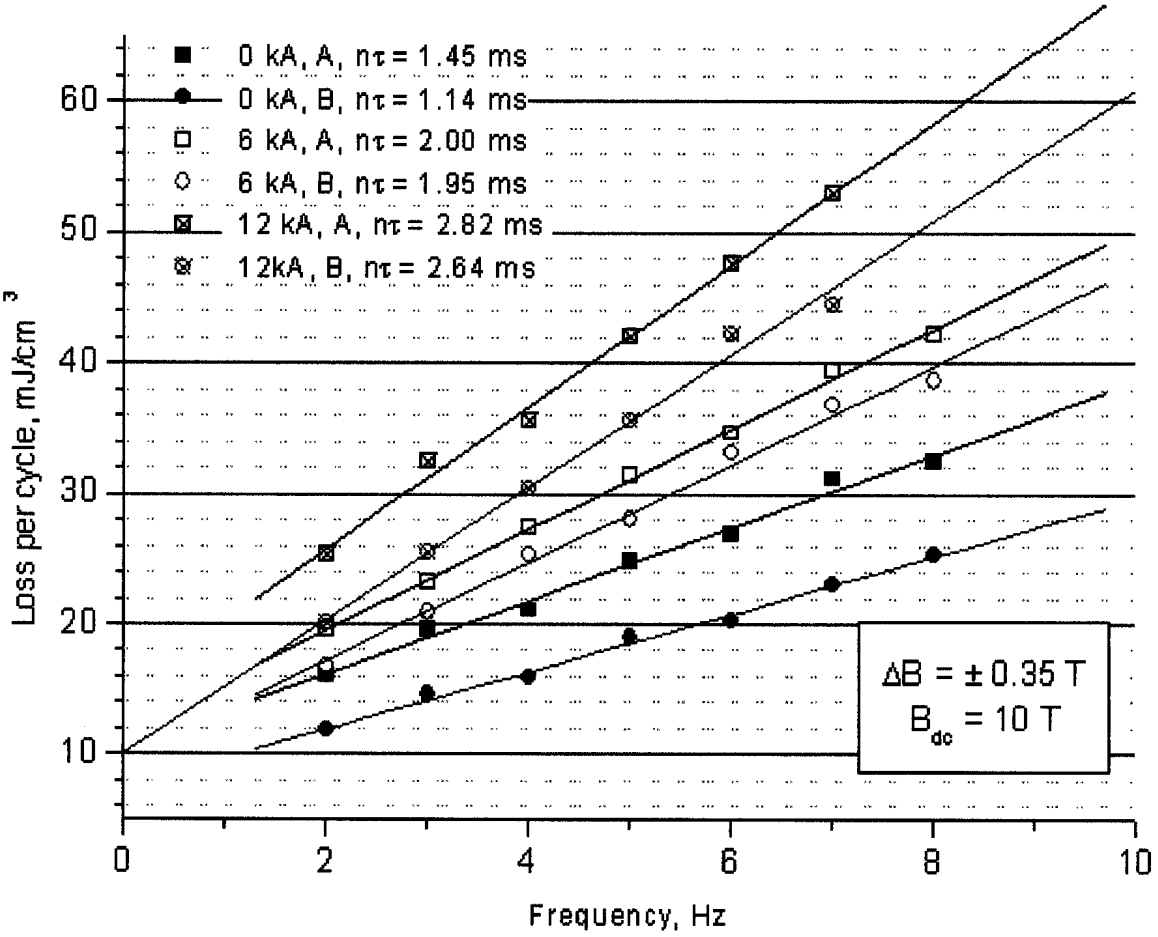

Fig. 23 Loss curves at 10 T background field and various transport current

current (330 A/mm^2, 6 T) was larger by a factor of 7, suggesting the occurrence of saturation loss. For the SeCRETS conductors, the linearity of the loss curve and the moderate loss increase suggest that no significant saturation occurs.

To assess the extrapolability of the loss results to a broader range of frequency, the 0-frequency intercepts of the loss curves are compared with the expected hysteresis loss estimated from the strand characteristics. The results are summarized in Table 11 as mJ/cm^3 ***non-Cu***. The extrapolation of three loss curves is considered. The first one measured at UT without background field, the other two in SULTAN at 2.2 and 9.7 T background field and I_{op}= 0. The average results of VNIINM are also reported (measurement by VSM).

Table 11 Summary of hysteresis loss extrapolation from the loss curves (mJ/cm^3 non-Cu)

	B_{dc}(T)	ΔB (T)	Test range	**A**	**B**	**A/B**
UT	0	± 0.4 sinus	0.03 - 0.15 Hz	116.913	93.890	1.245
SULTAN	2.2	± 0.3 sinus	2 - 9 Hz	19.62	13.145	1.493
SULTAN	9.71	± 0.35 sinus	2 - 8 Hz	26.50	18.875	1.404
VNIINM	0	± 3	dc	165	158	1.044

The hysteresis loss can be predicted according to the $J_c(B)$ and the effective filament diameter.The SeCRETS strands have the diffusion barrier consisting of a Ta foil buffered by a Nb foil. This turns into very high loss in the range ± 0.18 T, when the Nb barrier is superconducting and acts as a big filament, with diameter D ≈ 0.5 mm. Due to the large, non-linear impact of the Nb diffusion barrier, the measurements taken at 0 background field cannot be used to draw the effective filament diameter. For the same reason, the loss in the range around 0 T cannot be predicted by the loss formulae based on the geometric Nb_3Sn filament diameter and no benchmark of the test at UT can be done. The A/B ratio is very close in the two sets of SULTAN test. The lower A/B ratio for the results at 0 background field may be the effect of the superconducting Nb barrier contribution, shadowing the actual differences between A and B strands.

A tentative benchmark of the hysteresis loss at higher field, where the Nb barrier plays no role, is done using the filament diameter assessed by microscopic examination after the heat treatment (D_A=3.25μm and D_B=3.7 μm) and the non-Cu Jc calculated with the scaling parameters reported in Table 9. This approach assumes that no bridging occurs between the heat treated filaments. In fact, from the order of magnitude of the ± 3 T results, it seems that no severe bridging occurs. However, the hysteresis loss in A are always higher than in B (A/B > 1), although the filament diameter is larger in B. If occasional bridging actually occurs (in A more than in B), the following procedure tends to underestimate the loss.

Both at 2.2 and 9.7 T, the applied field variation fully penetrates the filaments, with penetration field $2B_p << \Delta B$. The hysteresis loss formula per non-Cu volume is

$$Q_{\perp} = \frac{4\Delta B D \bar{J}_{c\parallel}}{3\pi}\left(1 - \frac{\mu_o D \bar{J}_{c\parallel}}{\pi \Delta B}\right) \cong \frac{4\Delta B D \bar{J}_{c\parallel}}{3\pi} \; J/m^3 \qquad (2)$$

where J_{cll} is the non-Cu critical current density at the nominal background field. The results of eq. (2) for D_{fil} = 3.25 and 3.7 μm are compared in the tables below with the figures from Table 11, named Q_{test}. The loss is always as mJ/cm^3 non-Cu.

B_{dc}(T)	ΔB (T)	Q_{test} /Q for A	Q_{test} /Q for B
2.2	0.6	8.27	4.95
9.7	0.7	53	32

The procedure to predict the hysteresis loss is very rough as the filament diameter is not deduced from magnetic measurements and the estimate of J_c is also affected by error. Nonetheless, the discrepancy between the predicted figures and those extrapolated from the loss curves in SULTAN is too large to be ignored.

Against any reasonable prediction, $Q_{test}/\Delta B$, is larger at higher field, see Table 11. This could be explained by an "offset" heat in the gas flow calorimetry, given for example by some heat from the pulsed coils, which is not fully intercepted by the cooling channels

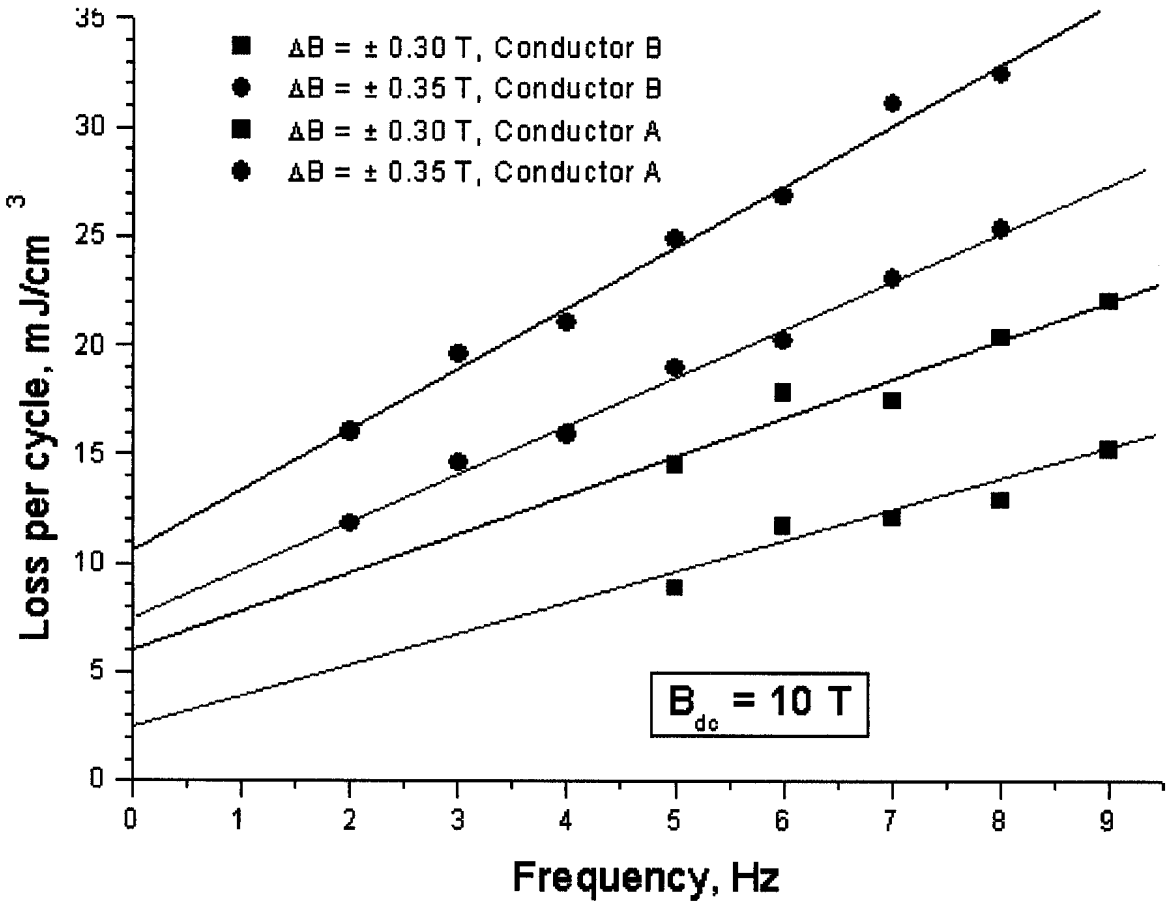

Fig. 24 Loss curves at 10 T, with extrapolation at 0-frequency

and loads the CICCs by heat conduction through the glass-epoxy spacers. At higher field, the pulsed coils develop higher power due to the magnetoresistance and this could explain why the "offset" is larger at higher background field. In the temperature traces, there is no evidence of such a "offset" heat load. After stopping the ac field, the temperature comes back to the initial level within 0.01 K. However, it cannot be excluded that the offset exists during the ac field.

The loss curves at B_{dc} = 9.7 T, I = 0, for $\Delta B = \pm 0.3$ and 0.35 T are plotted in Fig. 24. From eq. (2), the ratio of the intercepts at 0 frequency is expected to be 0.35/0.3 = 1.16, while the ratio of the slopes should be, according to eq. (1), $(0.35/0.3)^2 = 1.36$. Actually the ratio of the slope is 1.58 for both A and B (within 15% from the prediction), giving confidence in the order of magnitude of the coupling loss estimate. On the other hand, the ratio of the intercepts is in the range of 2 to 3, i.e. incompatible with the predicted hysteresis loss behavior, but in agreement with the hypothesis of some heat leaking from the pulsed coils and loading by conduction the CICC.

C.4.2 Energy calibration for stability runs

For transient stability measurements, the pulsed coils are excited with a sinus wave at the frequency of 15 Hz, either full or half period duration and variable amplitude, ΔB. The typical range of ΔB is 1-3 T. The ability of the conductors to withstand field transients is assessed in terms of the field integral $\int (dB/dt)^2 dt$ and it is not necessary to know the amount of deposited energy. However, to analyze the results with thermohydraulic codes, it is desirable to associate an "energy deposition" to the field transient.

Using the coupling loss time constant, $n\tau$, derived from Fig. 23 may be not an accurate procedure to estimate the deposited energy, as the time scale of the stability shots (15 Hz) is above the range of Fig. 23 (2 - 8 Hz). A direct assessment of the ac losses at 15 Hz was not planned in the experiment. A tentative calibration of the energy is done looking at the response of the temperature sensors after the pulsed coils (T5 and T6), for the runs ending with a recovery (no quench).

The transient duration (65 or 32 ms) is much shorter than the residence time of the Helium in the 300 mm long section of conductor exposed to the pulsed field. In the assumption of a perfect heat transfer between strands and coolant, the traveling heat slug caused by the ac losses in the CICC is expected to have the shape of a smoothed

trapezium. The rising time is the coolant speed times the shot duration. The flat top length is the length of the pulsed coils (300 mm) minus the length of the rising front. The flat top duration is initially expected to range between 0.65 s and 0.4 s, according to pulse duration and coolant speed. At the T5 and T6 location, 160 mm away from the pulsed coils, the spreading of the slug reduces the duration of the flat top by a factor of 2-3, according to the simulations carried out with the Gandalf code (see also Appendix).

The CERNOX sensors for SeCRETS are small chips (without case) with fast response, in the millisecond range. The sensor amplifier and the data acquisition system have low-pass filters with a time constant in the range of 250 ms (time required to raise from 10% to 90% of a square input). The way the sensor is placed in the sensor holder (Fig. 13 of section B) also introduces a delay in the response: the active sensor cannot be placed in the He stream, but must be placed in a quasi-stagnant pocket about one millimeter away from the strand bundle. The time required to establish the actual coolant temperature at the sensor location is in the range of 1 s.

The run NES180523, with 2.5 g/s mass flow rate, 65 ms, one-period transient field is discussed as an example of travelling heat slug. The coolant speed is 0.42 m/s, the rising front of the slug is expected to be 27 mm and the flat top 273 mm. The temperature

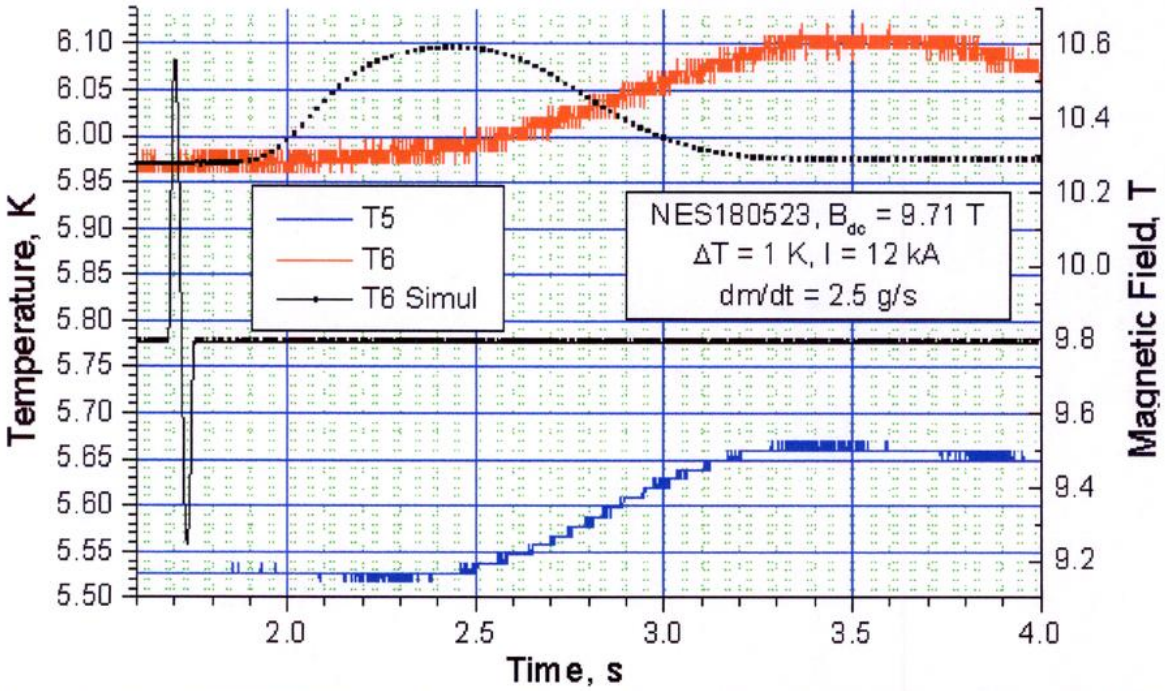

Fig. 25 Temperature traces of the sensors placed after the pulsed coils, showing the heat slug. The black, dotted line is the computer simulation of T6 with the energy input according to the temperature observed at the flat top, $E = \Delta H(\Delta T)\cdot\rho\cdot V_{He\ 300\ mm}$

profile at the sensors T5 and T6, see Fig. 25, starts to increase about 0.7 s after the pulse field shot, although the actual delay for the coolant to travel from the edge of the pulsed coils to the location of T5 and T6 (160 mm) is only 0.3-0.4 s.

From the temperature of the heat slug, ΔT, measured as the flat top of the sensor traces, the enthalpy change ΔH of the coolant is deduced at constant pressure. Multiplying by the density of the coolant and the coolant volume included in 300 mm of CICC, the energy deposited in the conductors is $E = \Delta H(\Delta T)\cdot\rho\cdot V_{He\ 300\ mm}$. This energy is given as an input in the computer simulation (black line in Fig.25): the temperature starts to increase, as expected, after about 0.3 s, the rising time is about 0.4 s due to the spreading of the original slug. The peak temperature is, consistently with the given energy input, the same as the temperature traces. The large delay between simulation and sensor traces is an evidence of the slow response of the sensor.

The time integration of the temperature profile is also a way to estimate the energy of the slug, $E = (dm/dt)\int C_p(T - T_{in})dt$. As long as the flat top is maintained, i.e. the duration of the flat top is longer than the time constant of the sensor, both methods to assess the energy of the slug must be equivalent, i.e. $(dm/dt)\int C_p(T - T_{in})dt = \Delta H(\Delta T)\cdot\rho\cdot V_{He\ 300\ mm}$ (this is the case for the black line in Fig. 25). However, for the T5 and T6 profiles in Fig. 25, $(dm/dt)\int C_p(T - T_{in})dt > 3.5\ \Delta H(\Delta T)\cdot\rho\cdot V_{He\ 300\ mm}$, providing evidence that the slug has been attenuated (smoothed and flattened) compared to the original one. If the coupling loss constant, nτ, would be deduced from the amplitude of the slug, ΔT, according to eq. (1),

$$n\tau = \frac{\Delta H\cdot\rho\cdot V_{He300mm}}{V_{Strand}}\frac{\mu_0}{\int (dB/dt)^2 dt}$$

the result would be in the range of nτ = 0.5 ms, what is hardly acceptable, as it is even less than the interfilament coupling loss (range of 1 ms).

A better guess for the coupling loss constant nτ can be done using the time integration of the slug temperature, i.e.

$$n\tau = \frac{(dm/dt)\int C_p(T - T_{in})dt}{V_{Strand}}\frac{\mu_0}{\int (dB/dt)^2 dt} \qquad (3)$$

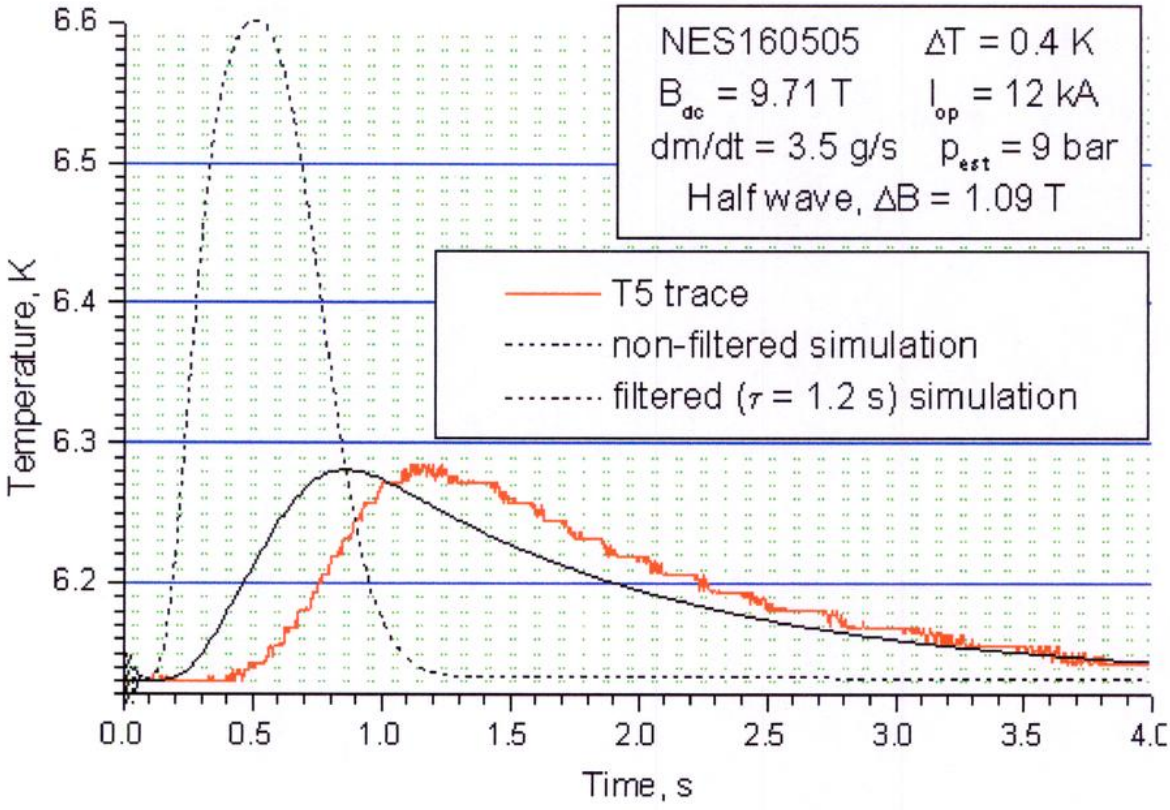

Fig. 26 Temperature profile of the heat slug generated by a half period pulse at T5, including the Gandalf simulation for the same energy, with and without applied filter

The effect of a low-pass filter can be applied to the computer simulation. The result for a half period pulse (run NES160505) is shown in Fig 26. The energy calculated from the time integral of the sensor trace, $(dm/dt)\int C_p(T-T_{in})dt$ = 4.7 J, is used as an input for the simulation. In this simulation, which is just aimed to heat calibration, the operating current is set to 0 to avoid any additional Joule heating when the current sharing temperature is hit. The dashed line shows the expected profile of the slug at the T5 location, without any filter. The solid line, with a low-pass filter with time constant 1.2 s, gives a much better fit of the sensor trace. The amplitude ΔT of the slug is reduced by a factor of 2.2 applying the filter. The integral up to 4 s changes only by -6% from the dashed to the solid line. Extrapolating the simulation beyond 4 s, the difference of the integral becomes marginal.

The match of the solid line and experimental profile is non-perfect. The heat slug simulated in Fig. 26 has duration of 32 ms. The measured temperature profile is taken after a pulse field shot of 32 ms duration. However, as the actual shot is taken with I_{op}= 12 kA, the heat of the slug include both the ac loss generated during the 32 ms of the field

transient and the Joule heating generated afterwards. This is considered the main reason of the mismatch of the experimental and simulation lines in Fig. 26.

The accuracy of the energy assessment by time integration of the heat slug is affected by the short acquisition time. After 4 s, which is the selected duration of the high rate acquisition, the temperature at the sensor is not fully back to the initial value, see Fig. 26 and 27, and the very tail of the slug and its integral must be extrapolated. The temperature profiles at T5 and T5bis (the last one located 10 cm downstream) and their integrals are compared in Fig.27. Eventually, the energy of the slug is estimated with an accuracy of ±10%, including the extrapolation error on the tail of the slug (Fig. 27), the reproducibility with the downstream sensors (T5bis and T6bis) and the accuracy of the mass flow rate.

Most of the slugs available for energy calibration are taken very close to the quench threshold. The energy of the heat slug includes the "deposited" coupling loss and also the Joule heating generated in the current sharing region. Comparing the slug energy for runs at much different distance from the quench threshold, the Joule heating is estimated to be

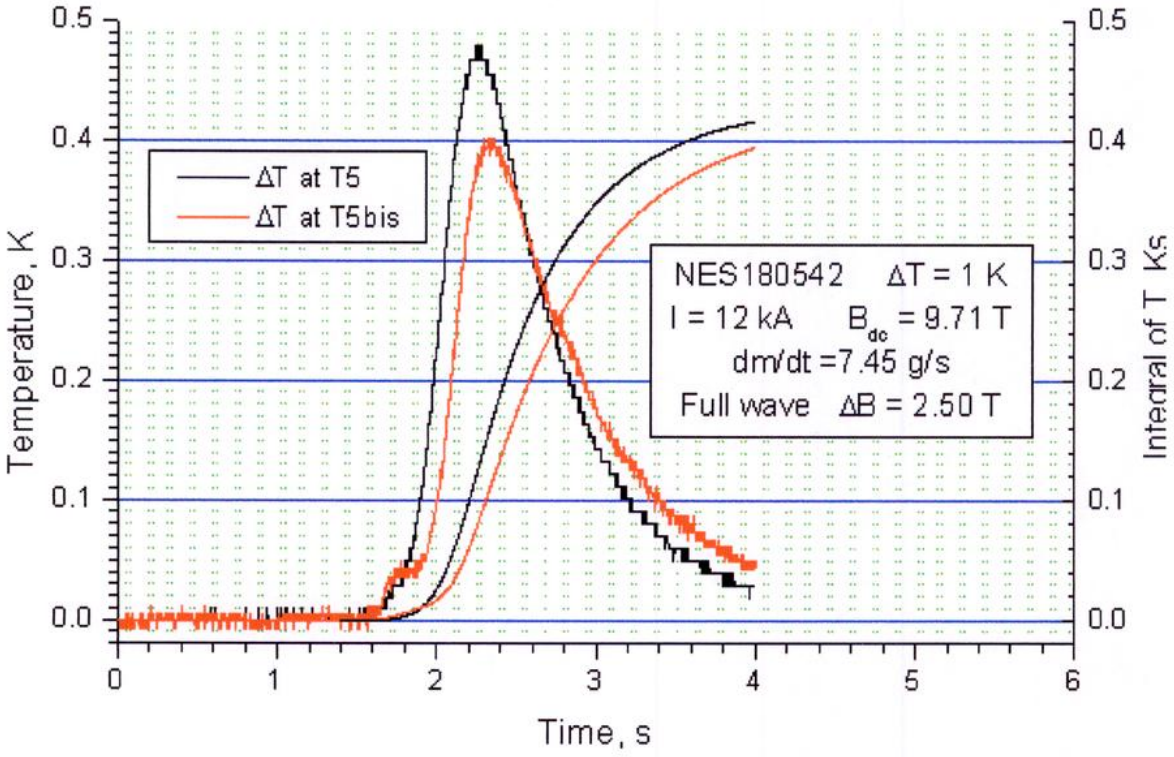

Fig. 27 Temperature increase (left axis) at the two sensorsT5 and T5bis, placed 100 mm downstream, and, on the right axis, the time integral of the temperature profiles up to 4 s.

Table 12. Coupling loss constant, nτ [ms] from the calorimetric calibration of stability runs at 9.71 T background field

	A and B
nτ @ 12 kA, full wave (average of four runs)	1.70 ± 0.20 ms
nτ @ 12 kA, half wave (average of four runs)	1.40 ± 0.20 ms

of 15% of the overall energy.

After subtracting the Joule energy, assumed 15% of $(dm/dt)\int C_p(T - T_{in})dt$, the coupling loss constant nτ is estimated according to eq. (3) for several stability runs where recovery was observed in both conductors, see Table 12. The loss in A is the same as in B, within the results accuracy. The loss @ 12 kA is larger than @ 10 kA. The loss for half wave is smaller than for full cycle due to enhanced screening. However, due to the overall accuracy, the difference of the average values should not be overemphasized.

Beside the ±10% accuracy in the estimate of the slug energy, the amplitude and the reproducibility of the Joule heating is a major issue for the accuracy of the coupling loss calibration at the stability runs. According to the simulations, see also Appendix, the fraction of the Joule heating is much higher in the half-period compared to the full-period shots. The accuracy of the Joule heating is not addressed in the results of Table 12, but should not be forgotten whenever the test results are "converted" in deposited energy.

The level of coupling loss in the stability runs is low, below 2 millisecond. The loss reduction between the "steady state" (2-8 Hz) and the single shot results at 15 Hz is in the range of 30% and is likely due to some screening occurring at15 Hz. As the conductors are multi-stage cables, the coupling currents cannot be properly described by a single time constant and eq. (1) is not strictly valid for large ωτ, i.e. the slope of the curve in the screening range is not proportional to $1/(1+\omega^2\tau^2)$.

The actual energy deposition is likely to be non-uniform over the cable cross section due to the screening effect and (for conductor B) to the copper segregation.

C.5 Plasma Disruption

With the bipolar power supply connected to the pulsed field coils, a broad range of field shapes can be generated. The desired shape is first written into a programmable wave form generator which is used as an input for the power supply, which acts as a current amplifier. The overall amplitude of the pulse cannot exceed ± 0.78 T, corresponding to ± 500 A and the pulse must be "closed", i.e. start and finish with 0 current in the pulsed coil.

The most crucial transverse field variation induced by plasma disruption is at the CS outer radius, with ΔB = -1.4 T and dB/dt = -5.5 T/s and at the CS inner radius, with ΔB = 0.2 T and dB/dt = 0.65 T/s. The last one is by far the most "dangerous" as the operating field at the inner radius is 12.7 T, opposite to 1 T at the outer radius. The field transients selected to simulate the plasma disruption are aimed to:

- reproduce the maximum dB/dt
- reproduce the shape of the pulse in the high dB/dt range
- have the same integral figure of field variation $\int (dB/dt)^2 dt$
- have similar range of field variation amplitude

The main parameters of the pulses are summarized in Table 13. A "large negative" pulse is designed to simulate the disruption at the CS outer radius. It is a half period sinusoidal wave, about 1.1 Hz frequency, with the maximum amplitude allowed by the pulsed field coils. A "small positive" pulse is designed to simulate the disruption at the inner radius of CS: the field is described by three equations:

$B(t) = 5.4\ t^2$ for $0 < t < 0.06$ s

$B(t) = 0.2144 - 0.15\ e^{(t-0\text{-}06)/0.3}$ for $0.06 < t < 0.8$ s

$B(t) = 0.1961 - 0.06(t-0.8)$ for $0.8 < t$ s

Table 13. Main parameters of the plasma disruption simulation

	"Large negative" pulse		"Small positive" pulse	
	Disruption	Simulation	Disruption	Simulation
ΔB, T	-1.4	**0.78**	0.22	**0.197**
dB/dt, T/s	-5.5	**± 5.5**	0.65	**0.648**
$\int (dB/dt)^2 dt$, T^2/s	4.5	**6.5**	0.073	**0.0814**

In the test program, several levels of operating current were foreseen. However, only the test with the highest operating current, 12 kA (400 A/mm^2), was carried out. The operating temperature margin at the pulsed coil location cannot be set below ≈ 0.3 K, as the downstream conductor section, at higher field, is already in advanced current sharing for that operating temperature.

The aim of the test was not achieved, i.e. it was impossible to find the minimum temperature margin necessary to withstand a plasma disruption transient. No quench occurred in any of the test run, with temperature margin as low as 0.3 K. In one run, a pulse field (small positive) was done when the A conductor had only 0.13 K and an irreversible temperature increase was starting at the minor peak field: even in these conditions, no quench was observed at the pulsed field location.

C.6 Transient Stability

When connected to the capacitor bench, the pulsed field coils build a RLC circuit with resonating frequency f = 15.3 Hz. The capacitor discharge can be cut either after one period of 65 ms (full wave) or after half period, 32 ms (half wave). When the half wave pulse is applied, the leads are connected to have the field change anti-parallel to the SULTAN field (compressive load on the pulsed coils). For full wave pulses, the field is initially parallel and then anti-parallel to the background field.

All the stability runs are taken with the field setting "10 T", i.e. with a background field of 9.71 T at the pulsed field location. The data acquisition is set on high sampling rate, 1 kHz/channel. The typical duration of a run is 4 s, largely sufficient to observe the detail of either a quench or recovery. The amplitude of the field pulse is monitored by the Hall sensors and by the current transducer of the capacitor bench. The location of the quench (either A or B) can be clearly solved by the voltage taps, although the inductive voltage on the test section (V21-V23 and V22-V24) saturates the amplifiers for about 20-50 ms after the end of the pulse. The temperature sensors after the pulse coils can also be used to identify the location of the quench, due to the larger heat developed in the quenched conductor. No re-cool time is required for the SeCRETS winding after a quench.

The transient field amplitude is always reported as ΔB, either meant as full swing (peak-to-peak) for the full wave pulse, or 0-to-peak for the half wave pulse. For safety reasons, the ultimate operating limit of the pulsed coils has not been explored. The largest field amplitude for half wave is ΔB_{hw}= 1.88 T (peak current 1206 A). In full wave mode, the

maximum field amplitude, ΔB_{fw}= 2.70 T (peak current ≈ 900 A), is limited by the mechanical load on the bolts of the steel clamp, see section B.3. In the stability plots, the integral of the field change, $\int (dB/dt)^2 dt$, is reported on the y-axis, rather than the field amplitude, ΔB.

$$\int (dB/dt)^2 dt = 72.17 \cdot \Delta B_{fw}^2 \qquad \text{for full wave pulse}$$

$$\int (dB/dt)^2 dt = 144.35 \cdot \Delta B_{hw}^2 \qquad \text{for half wave pulse}$$

The maximum value of field integral achieved in operation is 526 T^2/s, over two orders of magnitude larger than expected from the plasma disruption, see Table 13. The largest field rate, dB/dt = 180 T/s is obtained with the half wave pulse. The "deposited energy" is estimated according to eq. (3), with the nτ from Table 12 (calibration of stability runs).

The current sharing temperature, T_{cs} @ 1 μV/cm, see empty symbols on Fig. 10 and 11, is used as a reference to define the temperature margin, $\Delta T = T_{cs}-T_{op}$. As the conductors can be still operated at 1 μV/cm over a limited length, the stability curve is not expected to cross the 0, i.e. some margin exists also at ΔT = 0. In a larger winding, with longer conductor sections exposed to high field, T_{cs} is referred to the 0.1 μV/cm criterion and a much larger margin would be available for local disturbances at ΔT = 0. On the other hand, when both the high field section is long *and* the disturbance affects the whole high field section, the margin available at ΔT = 0 becomes very thin.

The operating temperature can be adjusted for ΔT ≥ 0.3 K at the pulsed field coils section. At higher operating temperature, a runaway starts at the minor peak field location, about 3 m downstream of the pulsed coils. The operating temperature is adjusted with an accuracy of ± 0.02 K. The reproducibility of the pulse field amplitude is better than 1%. The default mass flow rate is 3.5 - 4 g/s, unless another value is stated.

Most of the tests are carried out with either 12 or 10 kA operating current, corresponding to a non-Cu current density of 407 and 339 A/mm^2. At lower operating current, the range of measurements is drastically reduced, due to the difficult to quench the conductors.

C.6.1 Transient stability vs. temperature margin

A straight comparison of the transient stability for conductor A and B is shown in Fig. 28, with the stability curves at 12 kA operating current. The field transient is a full period, with 65 ms duration. The superior stability of conductor A is clearly measurable for transient integrals above 100 T^2/s. At lower disturbance level, both conductors could not be quenched in the range of available temperature margin.

At lower operating current, the stability improves, but not dramatically, see Table 14, where the stability (both as field integral and deposited energy) at 8, 10 and 12 kA is reported for ΔT = 0.4 K. The results in Table 14 are the average of the largest run with recovery and the smallest run with quench.

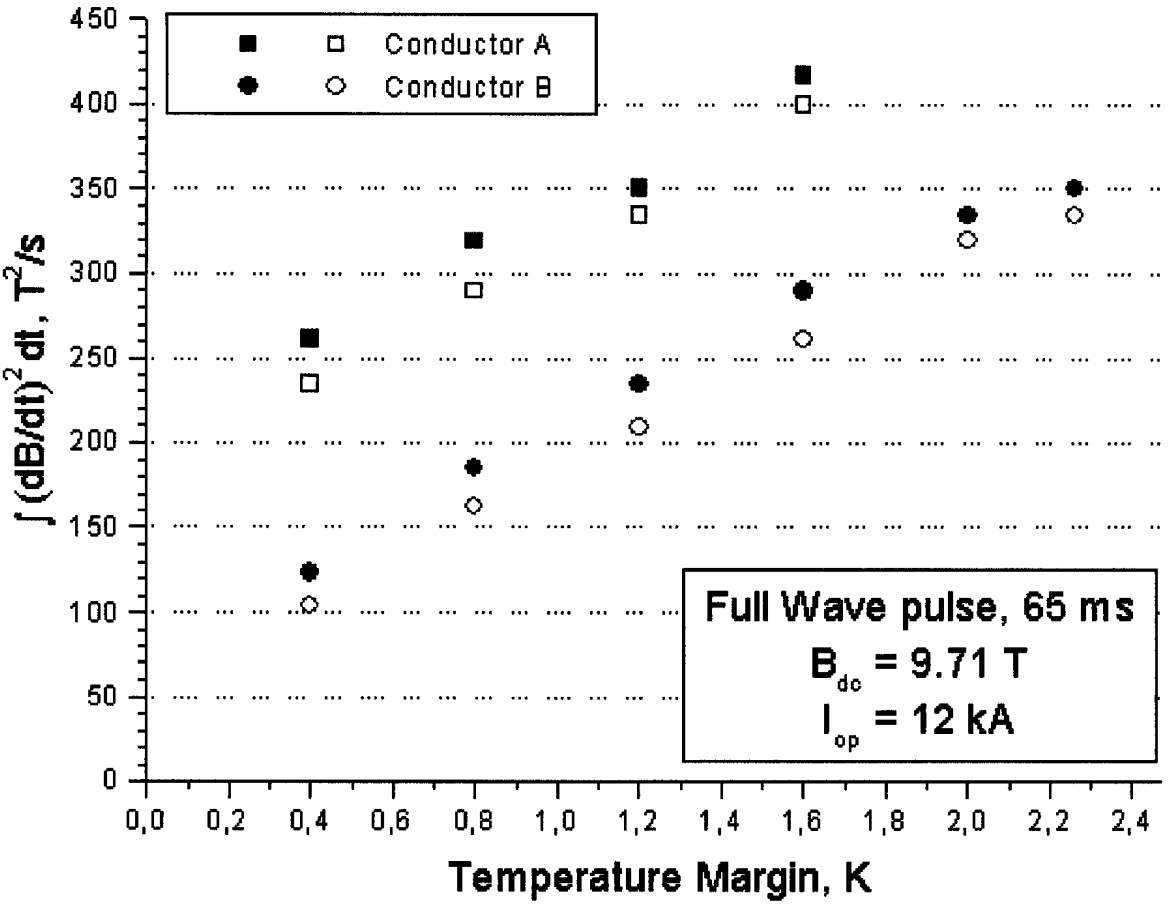

Fig. 28 Transient stability curve for full wave pulse at 12 kA

Table 14. Stability at B = 9.71 T, ΔT = 0.4 K, one-period pulse (65 ms) and different I_{op}

I_{op}	A		B	
	$\int (dB/dt)^2 dt$, T^2/s	Energy Loss, mJ/cm^3	$\int (dB/dt)^2 dt$, T^2/s	Energy Loss, mJ/cm^3
8 kA	375	137	196	50
10 kA	311	113	173	44
12 kA	248	107	113	41

The transient stability results for half-period pulse (32 ms duration) are added in Fig. 29. The performance of the conductor without segregated copper is again substantially better, as it was observed for the one-period field transient in Fig. 28.

On a shorter time scale, 32 ms instead of 65 ms, it is expected that the stability is poorer, because, for the same energy, the peak power is larger, the time available to remove the heat is shorter, and hence the peak strand temperature should be higher. A straight comparison of "full wave" vs. "half wave", in terms of field integral shows the opposite

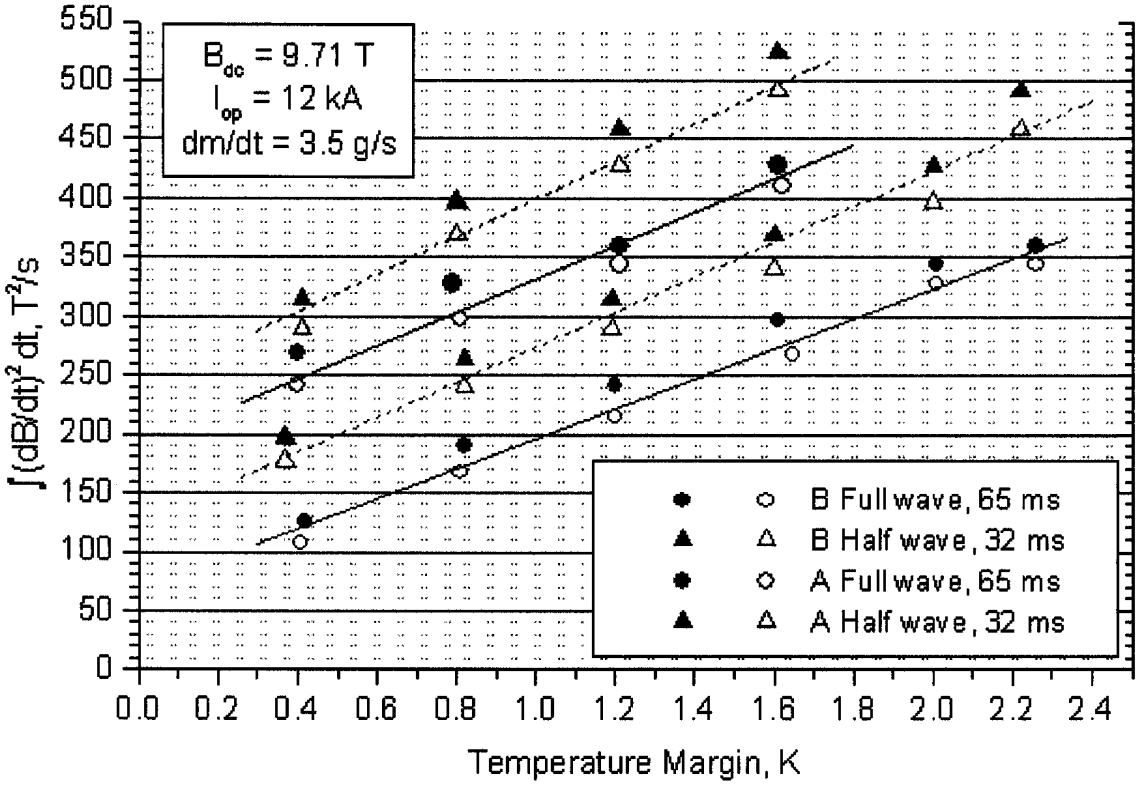

Fig. 29 Stability curves for A and B, half wave and full wave pulses, 12 kA

trend: at shorter disturbances, a larger field integral is tolerated, see Fig. 29. A possible explanation is the direction of the applied pulsed field. For the full-wave pulse, the overall field increases initially and T_{cs} decreases. For the half-period pulse the applied field subtracts to the background field and the temperature margin increases during the transient.

Once the results are "converted" into deposited energy, Fig. 30 for A and 31 for B, using the coupling loss constant in Table 12, the stability seems to be identical for full and half wave, due to the lower loss assumed at half wave.

The stability behavior of the SeCRETS conductors has been simulated with the Gandalf code. The conductor properties, taken from Table 9, give the same T_{cs}. The actual field variation during the transient is also accounted, with $T_{cs} = f(B(t))$. The energy deposition is modulated in time, see Appendix. Due to the higher peak power, the energy modulation has a negative impact on the stability, reducing the threshold energy by ≈ 30% compared to the case of constant (non-modulated) power during the transient.

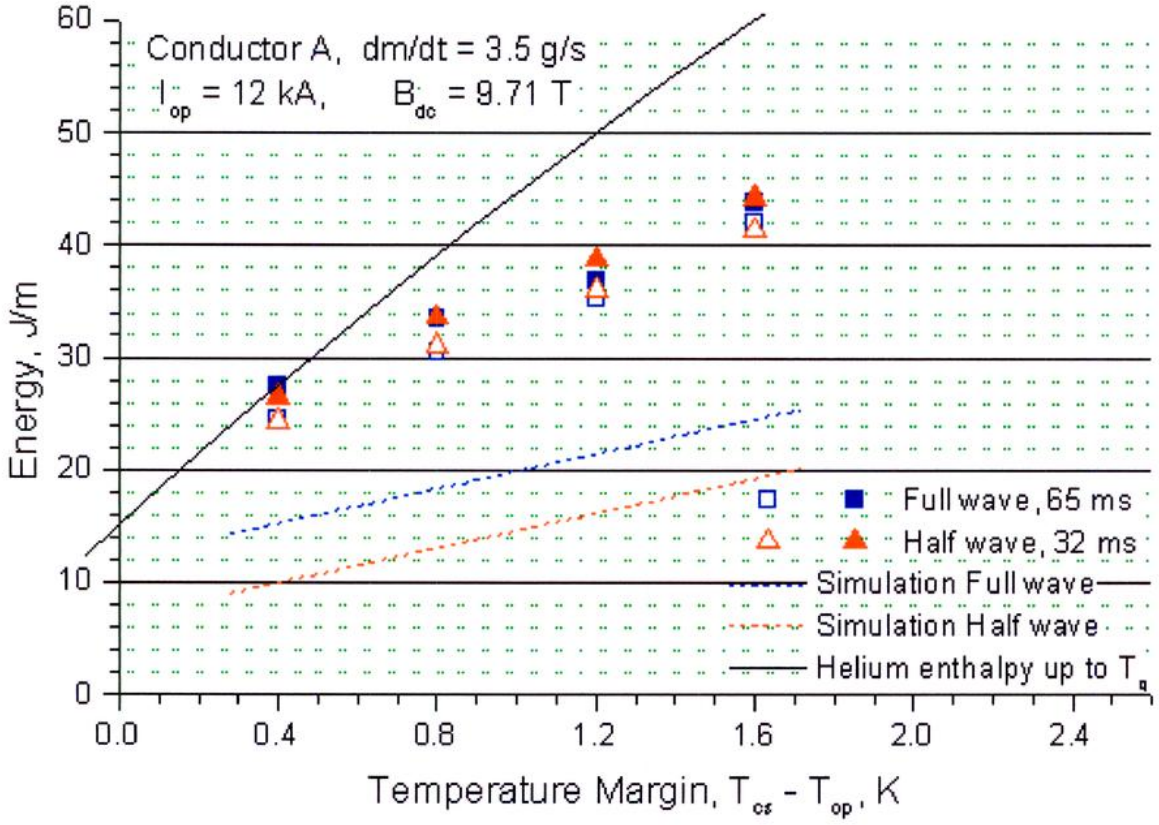

Fig. 30 Stability (J/m) vs. Temperature margin for conductor A: half wave and full wave results, including the He enthalpy and the Gandalf simulation

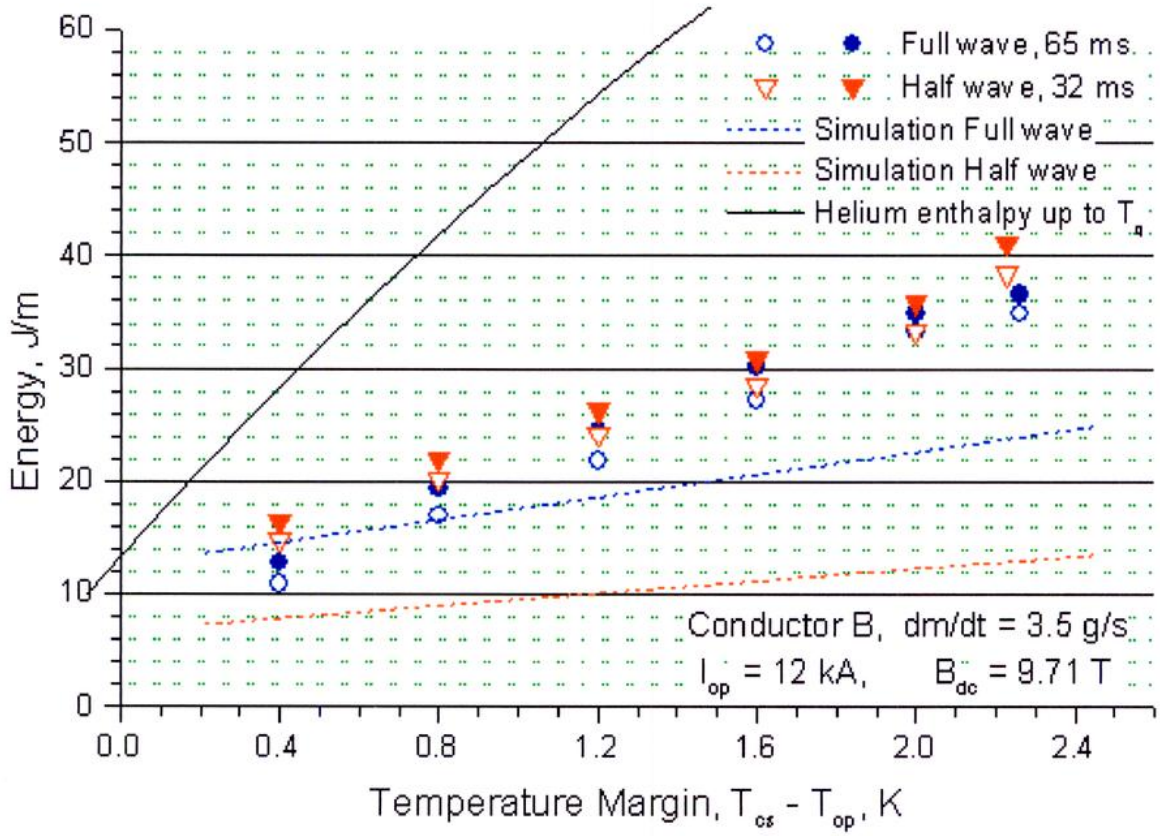

Fig. 31 Stability (J/m) vs. Temperature margin for conductor B: half wave and full wave results, including the He enthalpy and the Gandalf simulation

The Helium enthalpy, calculated from the integral of the coolant specific heat, $\int C_p dT$, and also referred as "energy margin", is also plotted in Fig. 30 and 31. As the conductor can be operated over a short length above T_{cs}, the integral is extended from T_{op} to the experimentally measured runaway temperature, T_q. According to the results in Table 6, T_q is about 0.45 K higher than T_{cs} for conductor A and 0.35 K higher for conductor B. As the length of the pulsed coils (300 mm) is shorter than the length of high field where T_q was measured (2-3 m), the actual runaway temperature and the associated energy margin in Fig. 30 and 31 may be underestimated.

The experimental stability results lay below the energy margin, which is the limiting value in case of perfect heat exchange between strand and coolant ($h \cdot p \rightarrow \infty$). The likely crossing of the trend lines at small temperature margin may be an effect of the systematic error on the estimate of both energy margin and coupling loss. The simulation results indicate higher stability for full wave pulses. Beside the sensitivity to the field modulation, the simulation results strongly depend on the assumptions on power

modulation and the model selected for the heat transfer coefficient, see Appendix. The simulation for conductor B fully neglects the segregated copper: the energy is deposited only in the superconducting strands, only the wet perimeter of the superconducting strands is accounted for the heat transfer to the coolant and only the copper embedded in the superconducting strands participates to the current sharing.

C.6.2 Transient stability vs. operating current

The transient stability is measured at fixed operating temperature as a function of the operating current. The operating temperatures are selected in order to obtain I_c little higher than 12 kA at 9.71 T. For the two conductors, the set of values is

A $T_{op} = 6.2$ K Extrapolated I_c @ 1μV/cm = 13 132 A
B $T_{op} = 6.6$ K Extrapolated I_c @ 1μV/cm = 13 321 A

The limiting current is calculated for both conductors at the operating conditions, using the Table 1 section B and Table 3 section C. The heat transfer coefficient is assumed h = 1000 W/m^{2}K, as in the ITER design criteria. Only the non-segregated copper is

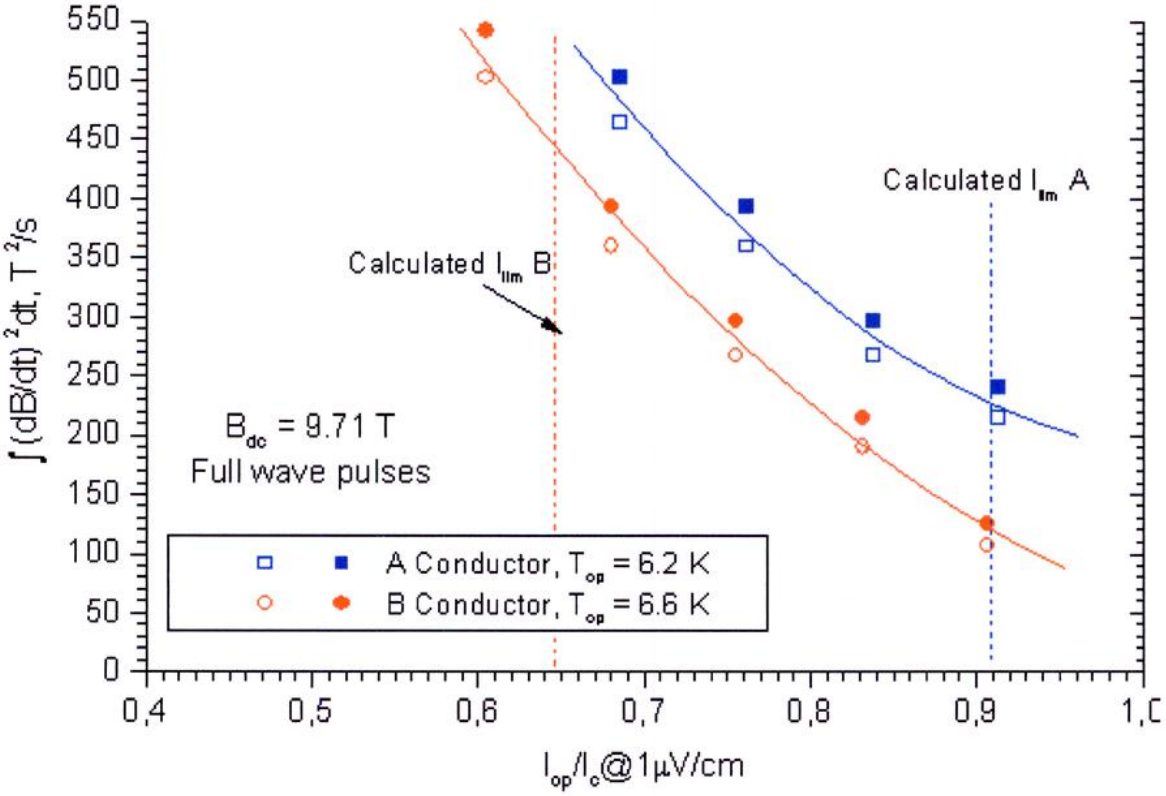

Fig. 32 Stability curves at fixed operating temperature vs. operating current, dm/dt=3.5g/s, with the expected limiting current, calculated for h = 1000.

accounted in conductor B.

$I_{\lim}^{A} = 11\,939$ A $\qquad I_{\lim}^{B} = 8\,576$ A

$(I_{\lim} / I_c)_A = 0.909 \qquad (I_{\lim} / I_c)_B = 0.648$

The test results are shown in Fig. 32, with the field integral plotted against the ratio of the operating current (8, 9, 10, 11 and 12 kA) to I_c. No inflection is observed at the above calculated I_{lim}.

In Fig. 33, the same experimental points are plotted as deposited energy vs. I_{op}/I_c. The same coupling loss constant ($n\tau$ = 1.7 ms) is assumed over the full range of operating current. Here, opposite to Fig.32, I_c is a function of I_{op} because of the small change of the operating strain and the experimental points are slightly displaced. The coolant enthalpy from T_{op} to T_q is plotted as solid lines (almost identical for A and B). The Gandalf simulation for the same operating conditions are plotted as dashed lines in Fig. 33. The simulations are carried out for a range of operating current broader than in the experiment, extrapolating the field modulation from the closest experimental point. For conductor B, the start of the limiting current inflection is visible at $I_{op} \approx 0.95\ I_c$.

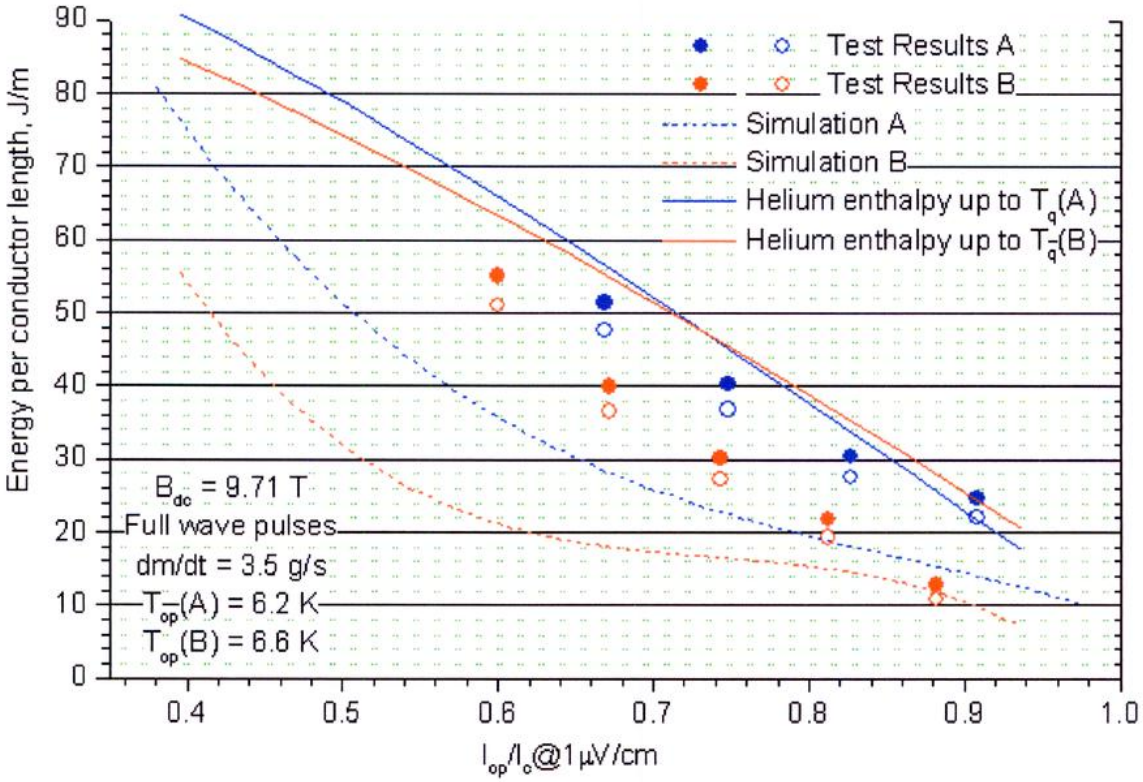

Fig. 33 Comparison of test results and Gandalf simulation for stability vs. operating current (same data as Fig.32). The Helium enthalpy is the solid line

The steady state heat transfer coefficient obtained by Gandalf for the operating mass flow rate of 3.5 g/s (constant for all the runs of Fig.32), is h = 2000 W/m^{2}K. The limiting current, calculated with h = 2000, is higher than the critical current for conductor A and very close to I_c for conductor B, The lack of the expected inflection in the experimental results is explained by a far too conservative assumption on the heat transfer coefficient

C.6.3 Transient stability versus mass flow rate

The dependence of the stability on the mass flow rate has been systematically investigated after noticing that two runs, identical except the mass flow rate, had substantially different stability performance. The operating current is 12 kA and the operating temperature is adjusted to 5.53 K (A) and 5.95 K (B), for a constant temperature margin, ΔT = 1 K, with an accuracy better than 0.05 K. The pulse mode is "full wave".

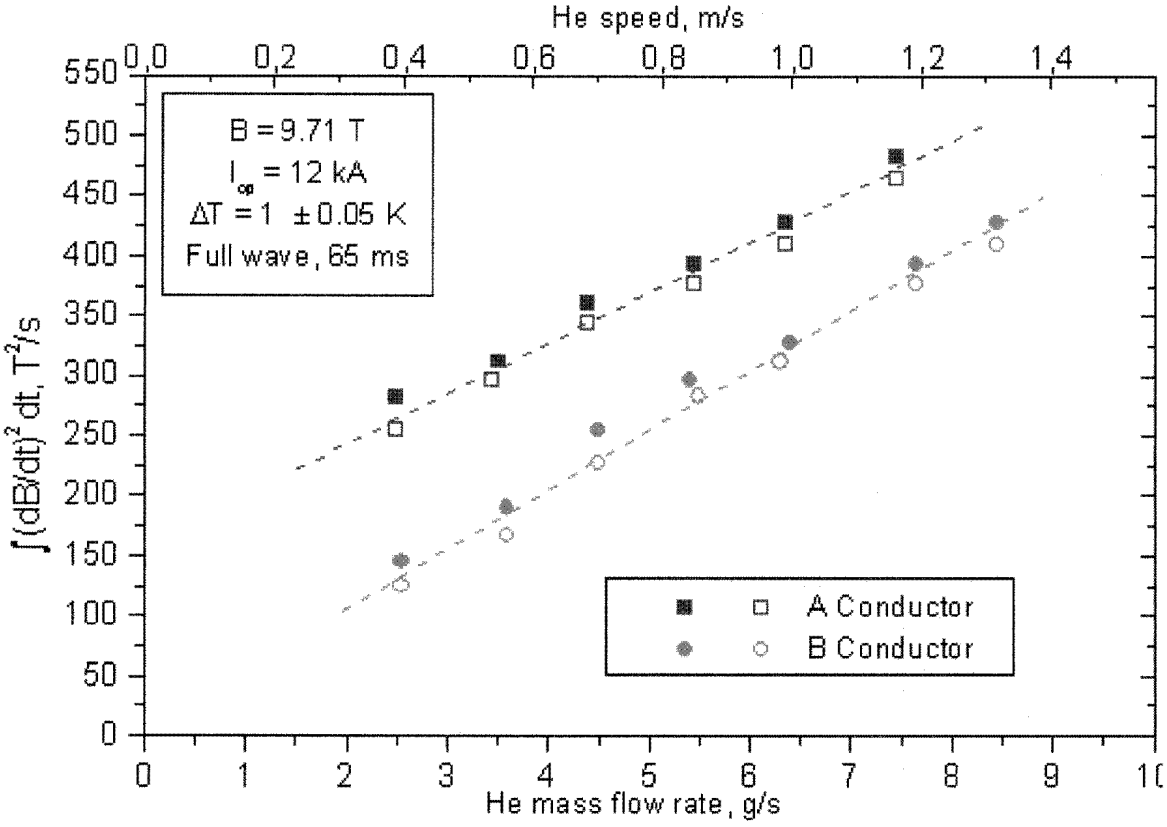

Fig. 34 Stability curves for A and B, versus mass flow rate

The experimental results for A and B are gathered in Fig. 34 as field integral vs. mass flow rate and coolant speed. Doubling the coolant speed, the threshold of the field integral increases by 30-50%. In Fig. 35, the results of the same test runs are plotted as deposited energy together with the Gandalf simulation results (segment lines) and the He enthalpy. Although the temperature margin (ΔT = 1 K) is identical for all the runs, the He enthalpy slightly increases with the mass flow rate due to the decreasing operating pressure. The He enthalpy is slightly higher for B because of the higher operating temperature necessary to obtain the same temperature margin. The improvement of the transient stability with higher mass flow rate is solely due to the enhanced steady state heat transfer coefficient, h, which increases with the coolant speed at the power of 0.9, according to the Dittus-Bölter correlation.

From the code Gandalf, the instantaneous average heat transfer coefficient for the recovery runs of conductor B in Fig. 35 is calculated just before the shot (steady state) and at its maximum value, h_{peak}, achieved during the transient. The evolution of the heat

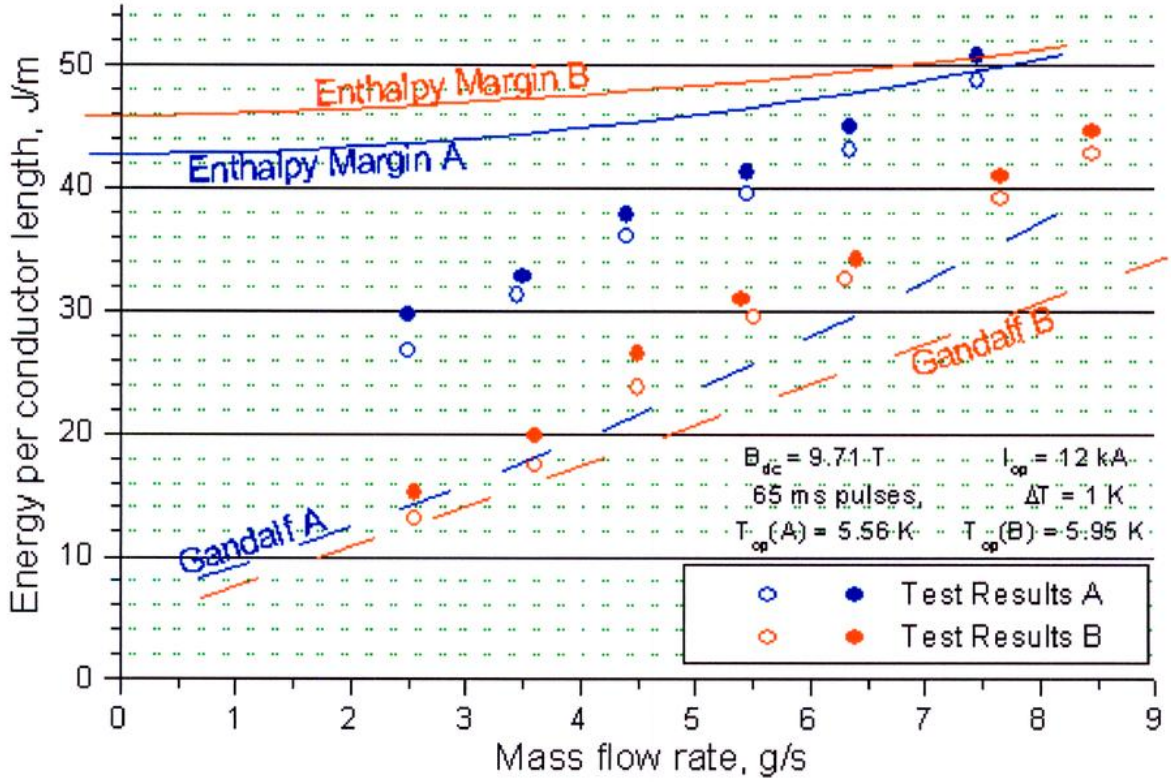

Fig. 35 The same experimental data as in Fig.34 (Stability vs. mass flow rate) plotted as deposited energy per conductor unit length, together with the Gandalf simulation results (dashed lines) and the He enthalpy margin

transfer The results are plotted in Fig.36. The steady state heat transfer coefficient, h_{ss}, increases with the mass flow rate according to the Dittus-Bölter correlation (which is included in the code). The peak value of h, due to the penetration of the boundary layer, see Appendix, is higher than h_{ss} only at mass flow rate smaller than 4.5 g/s: in this range the peak value is not a function of the initial h_{ss}. At mass flow rate larger than 4.5 g/s, the peak value is only marginally higher than h_{ss}, as the boundary layer is thinner and h_{ss} is larger. The peak is achieved in the first milliseconds of the transient. The stability results of Fig.34, i.e. the removed heat, behave like h_{ss} rather than h_{peak}, suggesting that the heat removed by the saturation of the boundary layer does not play any significant role for the range of disturbance energies discussed here.

No evidence of "induced flow" (enhanced, constant h due to the turbulence generated by the initial heat removal) could be observed either in the experimental results or in the simulations. Due to the strong dependence of the heat transfer coefficient on the local coolant speed, the design criteria should not be tied to a constant value, what could turn to be either extremely pessimistic or extremely optimistic.

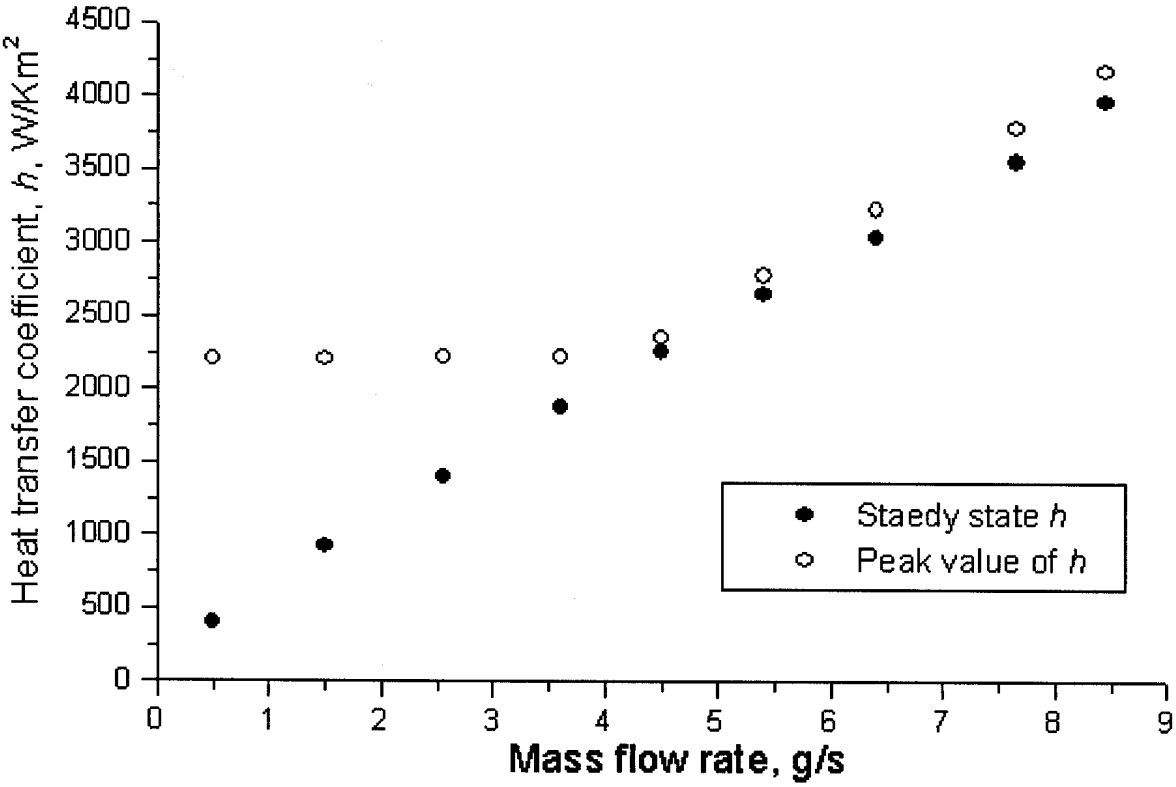

Fig. 36 The heat transfer coefficient, h, as obtained from the Gandalf code simulation of the test run in Fig.33, conductor B. The steady state h is calculated before the transient.

C.7 Current Distribution

A number of dc, ac losses and stability runs have been repeated with the data acquisition channels connected in the "C" mode, i.e. with all the Hall sensors recorded and other instrumentation discarded (pick-up coils, pressure and half of the voltage taps).

In the ac losses runs, the object of the Hall sensors investigations is to detect boundary induced coupling currents. When a short section of superconductor is exposed to an ac field, the induced coupling currents may propagate in the adjacent sections of conductor. This effect has been observed in accelerator cable, leading to severe current unbalance. In the SeCRETS conductors, applying an ac field with the largest operating current, 12 kA, no change of the self-field pattern could be observed in the Hall sensors placed next to pulsed coils section. A weak superimposed ac signal at the Hall sensors was due to the stray field from the pulsed coils at the sensors location. The lack of detectable boundary induced coupling currents is not surprising due to the very low level of coupling loss, likely confined within the strands.

The self-field pattern at the Hall sensors next to pulsed coils has been monitored during transient field shots (full wave), followed by either a recovery or a quench. No detectable change of the current distribution is observed during the quench evolution, i.e. in the ≈ 300 ms between the pulse field and the current dump. Assuming that the local field at the pulsed coils actually exceeds B_c during a full wave shot, the "disturbance" is homogeneous and no detectable current re-distribution occurs.

C.7.1 Analysis of DC runs

The response of the annular array of Hall sensors (evenly spaced by 60°) is represented as a polar plot in which the angle corresponds to the annular position of a sensor. The magnitude of the radius is the magnetic amplitude. In the linear array, the Hall sensors are placed evenly along a length corresponding to the pitch of the last cable stage (160 mm), with the last cable stage making a full turn of 360°. Therefore, the linear Hall sensors can be represented, at least with respect to the last cabling stage, as an annular array of ten, with an angle of 36° between the sensors.

The Hall sensors in any array are sensitive not only to the conductor self-field, but also to the magnetic field from the neighboring conductors, as well as to the background field from SULTAN. Moreover, the conductors are not straight (except for the part near joint), with the field at the inner radius larger than at the outer radius. At 0 current in the

SeCRETS winding, the SULTAN field can be zeroed together with the voltage offset of the sensor (including thermal voltages). The field contribution from the neighboring conductors, proportional to the operating current according to the Biot-Savart expression, is calculated and subtracted at each sensor location. The apparent difference between the signal of sensors in the same array, e.g. up to 30% in the annular arrays, is to large extent due to the non-homogeneous contribution from the neighboring conductors and to the bent geometry.

This section discusses mainly the results of runs CED310501-4 and COH250501, in which the current was raised at 50 A/s from 0 to 12 kA and back to 0, with a flat top of about 80 s. No heater was used and the mass flow rate was about 3.5 g/s.

The response of the annular array of conductor B close to the joint location (HaJ B1-6) is shown in Fig. 37 as a polar plot, at I = 12 kA and different background field. The average noise level increases from ± 0.6 % @ B_{dc}= 0 T up to ± 1.5% @ B_{dc}= 11 T. The maximum deviation of the calculated values from the measured ones at B_{dc} = 0 T is ~ 4 %. Beside the possible non-uniform current distribution, this difference may be due to the accuracy

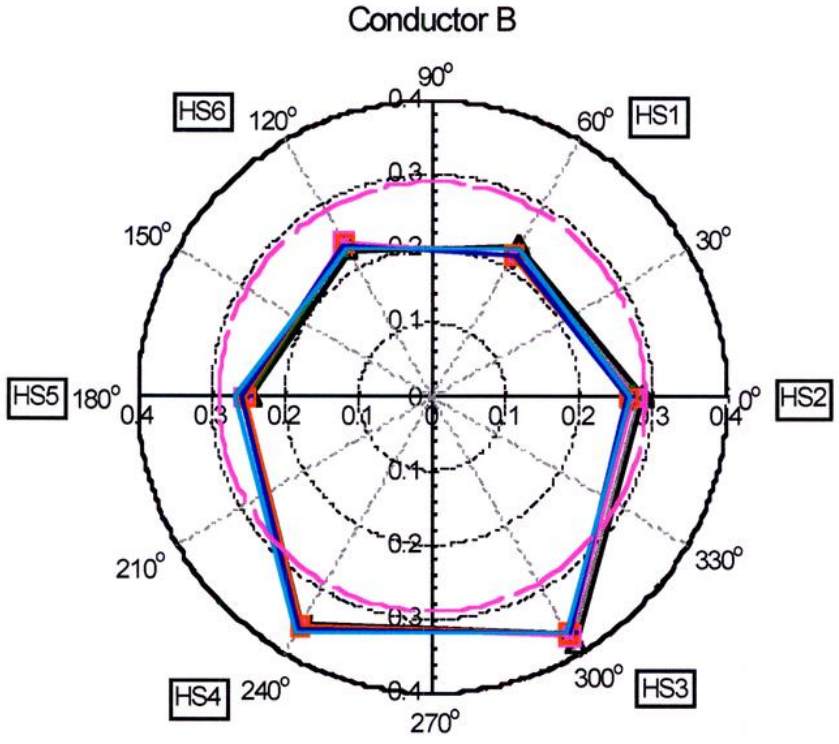

Fig. 37 Polar plot of the annular Hall sensors array close to the joint. The magenta line is for a straight, isolated conductor with balanced current distribution. The cyan line is the prediction for actual geometry and balanced distribution. The other lines are the experimental results at different background field.

of the sensor positioning (at least ± 0.2 mm) and Hall coefficient (linearity deviation ≈ 2% at 2 T). There is no significant change of the self-field values with background magnetic field (and temperature) rise. The maximum deviation between the experimental data at 0 T and 11 T for conductor A amounts to 5% (average 3%) and 3% (average 1.2%) for conductor B.

The result of the annular array placed next to the pulsed field coil (Hap A1-6) is plotted in Fig. 38. These Hall sensors catch a considerable fraction of the background field. The noise-to-signal ratio after subtracting the contribution of the background field is in the range of ±5 %. The maximum deviation between the calculated and measured values of self-field at $B_{d\ c}$= 0 T is within 5%, i.e. comparable to the array near the joint. The difference in Hall sensor signals with magnetic field (and temperature) rise, is slightly larger than in Fig. 37: ~9% for conductor A (average 4.3%) and ~7% for conductor B (average 3.2%).

The signals from the Hall sensors in the annular arrays in the high field region (HaHF A1-6) change the most with rising magnetic field, see Fig. 39. The maximum deviation between the calculated values and the measured ones at B_{dc} = 0 T amounts to 10 %. With increasing field (or temperature), the max deviation between the experimental data at B_{dc} = 0 T and 11 T amounts to ~25% (average 13%) for conductor A and ~9% (average 5%)

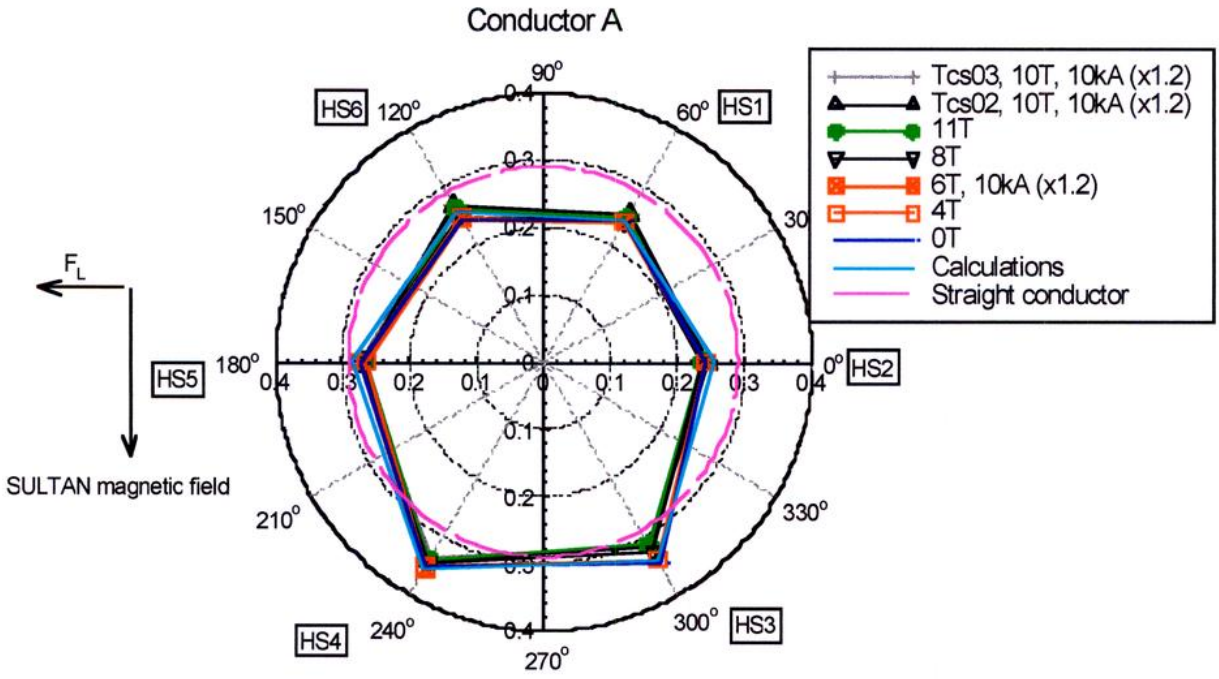

Fig. 38 Polar plot of the annular Hall sensors array close to the pulsed field, at12 kA and different background field (background field zeroed)

for conductor B. The average noise level is very high and a quantitative analysis of the results is rather speculative.

In order to calculate the unknown currents in the conductor cross section by using the

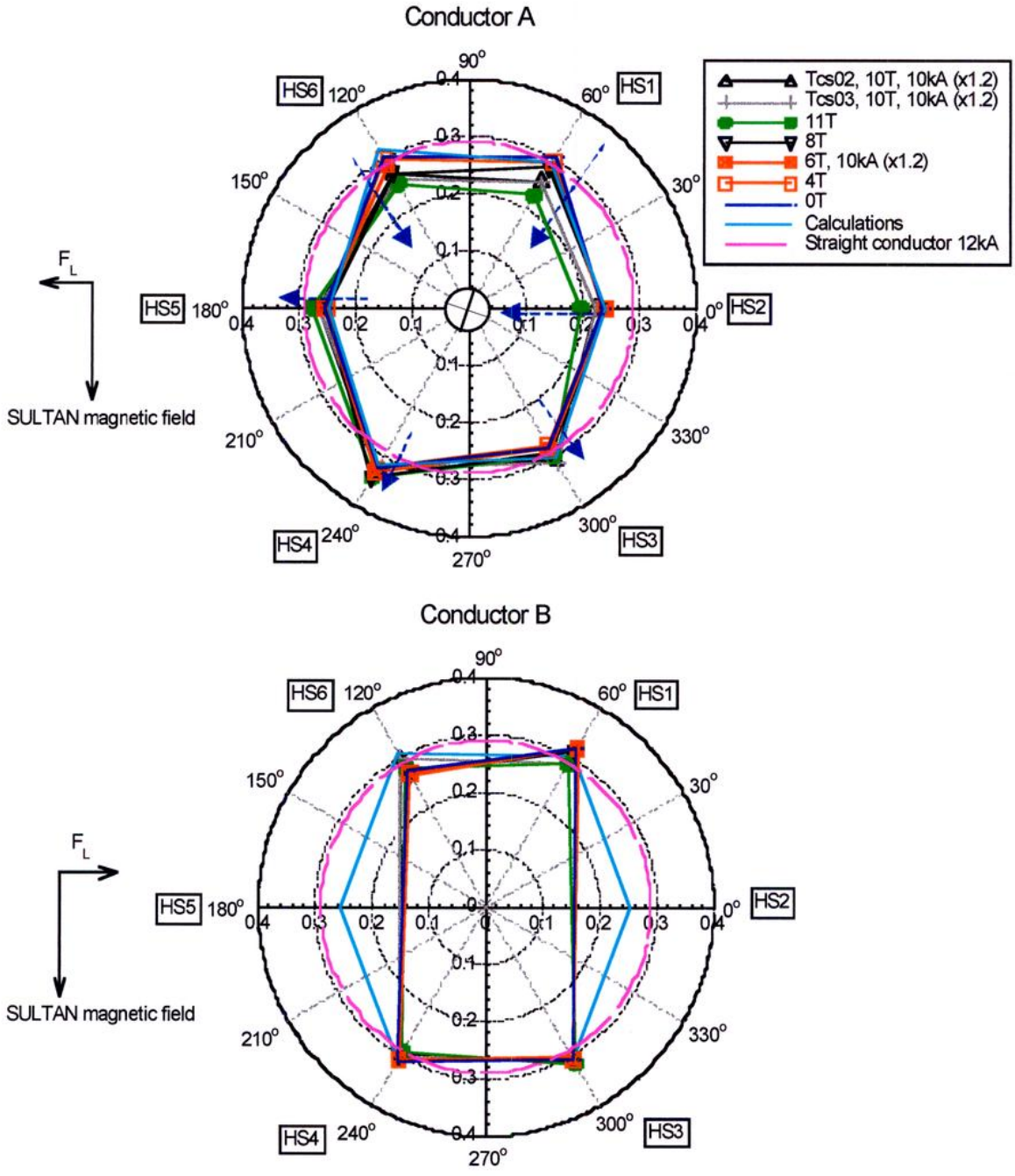

Fig. 39 Polar plot of the annular Hall sensors array at the highest field location, I_{op}= 12 kA. The arrows show the direction of the current displacement with raising background field. Two out of six sensors are missing in the array of conductor B. The larger self field changes in conductor A are well correlated with higher voltage drop in the high field region due to current sharing.

known magnetic self-field distribution around the conductor, the inverse problem must be solved. A model is assumed with six unknown currents distributed equally as identical segments in the conductor. An error of about 3% in the self-field measurements leads to 18% error in the current calculation. The experimental error in all cases is more than 3%. Hence, it is impossible to draw reliable quantitative conclusion about the degree of current unbalance in the conductor for the stationary conditions.

A qualitative analysis suggests an increase of the self-field in the direction of the Lorentz forces, F_L, at increasing field, see the arrows in Fig. 39. This is consistent with both a compression of the strand bundle to the wall of the jacket and a current displacement toward the conductor section with the lowest field, due to the locally induced current sharing. In Fig. 39, the self-field decreases at HS2, the side where the self-field adds to the background field and strand saturation occurs, and increases at HS5, where the field is minimum. The larger self-field change observed in conductor A correlates well with the voltage observed at the high field section, ten times larger than in conductor B. The earlier current sharing in conductor A for the same operating temperature (no heater) is due to the higher compressive strain (inward Lorentz forces).

A similar correlation between high field voltage drop and change of self-field signal is observed in the T_{cs} run, when the temperature is slowly increased. However, the amplitude of the change is smaller than in Fig. 39,because the initial distribution (when the temperature start to increase) is already affected by the peak field.

The response of the linear arrays is shown in Fig. 40 as a projection on a polar plot, just for graphical reasons: in fact, the sensors are not at the same conductor cross section. The SULTAN field is not sensed (within the orientation accuracy) and the field from the neighboring conductors is also identical, due to the symmetric location of the ten sensors. The maximum deviation of the calculated values from measured ones at B_{dc}=0 T is 5%. With increasing field, the maximum deviation between the experimental data becomes ~12% (average 5%). The noise level is much smaller than for the annular arrays in the "high field" region.

For all sensors the signals increase with field. This does not happens at the ring arrays, where the self-field increase of one sensor is balanced by the decrease at another sensor, to keep constant the field integral over the perimeter, i.e. the operating current. The net change of self-field in the sensors of the linear array is correlated with current displacement (transverse current sharing) over the 160 mm length of the linear array.

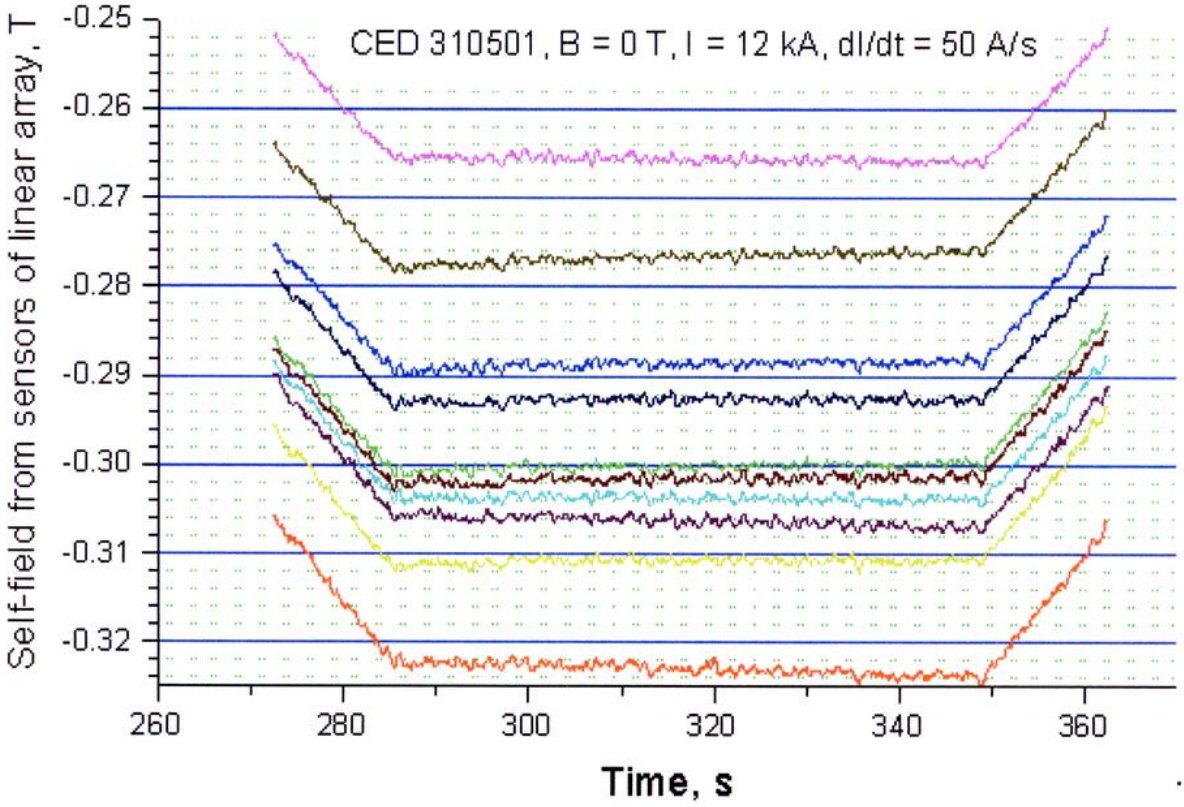

Fig. 41 Time evolution of the self-field from the ten sensors of the linear array at the flat top of a current ramp(signals smoothed by adjacent averaging, initial offset non-zeroed)

When the current is ramped in the conductor, the inductive voltage controls the current distribution among the strands. At constant current, the resistance at the joints drives the current re-distribution. This effect is at best observed at the linear array of sensors, due to the low noise level. In Fig. 41, the time evolution of the signals from the linear Hall sensors near conductor A is shown at the flat top for a run up to 12 kA at 50 A/s. The amplitude of the signal change is only ~1-2%. According to the above six sub-bundles model, this corresponds to a change in the sub bundle current of ≈ 0.2 kA. The time constant, range of 20-130 s for different Hall sensors, is characteristic of the winding sample rather than the conductor, i.e. cannot be extrapolated to other windings.

Although the sub-bundles of the cable form a loop closing at the termination, it is misleading to describe the above effect as a decay of an induced current loop. In fact, an external field change does not induce any current in such a "loop" because of the cable transposition. The overall current in the "loop" does not decay at all, but shifts from some strands to other strands with a time constant.

D. Conclusion and Implication

Experimental Methods and Instrumentation

For the dc test, the CERNOX temperature sensors provided accurate and consistent results, with error bar in the range of ±0.02 K. The time response to stepwise temperature changes is in the range of 1 s, due to the slow mass exchange in the He pocket of the sensor holder. The voltage taps are noisy, due apparently to the power supply, and a low-pass filter is needed to resolve voltage level smaller than 50 μV.

The pulsed field coil operated reliably at very high level of field rate (up to 180 T/s) in high background dc field (11 T). The very large field integral, $\int (dB/dt)^2 dt > 500\ T^2/s$, allowed to explore a broad range of transient stability. The pulsed coils location, symmetric with respect to the SULTAN coils, prevented the triggering of the quench detection voltage bridge. The cooling channels intercepted the Joule heat from the copper windings. However, at high power load, some fraction of the Joule heat may have leaked through the glass-epoxy spacers into the cable-in-conduit, affecting the accuracy of the hysteresis loss results.

The calorimetric measurement of the coupling loss was satisfactory in the range of 2 to 9 Hz. The duration of the field sweep had to be somehow longer than expected to allow the temperature sensors to achieve steady state. At lower frequency, the ac losses power is too small for calorimetric measurements. The magnetization method for ac losses failed, despite the sophisticated design of the pick-up coils, because of uncontrolled thermal voltage (from the soldered connections in the pick-up coils) overlapping to the induced voltage during the field pulse.

The Hall sensor arrays for self-field measurements performed satisfactorily. However, the data reduction indicates that a higher accuracy, much better than 1%, is required to draw useful results on current distribution. The issues of the sensor linearity at high field, the compensation of the background field, the accuracy of sensor location and the signal-to-noise ratio need to be addressed to improve the testing method.

The dc Results

At a first approach, the critical current of the strand scales correctly to the critical current and current sharing temperature of the cabled conductors. The lower slope of the voltage-current characteristic (n-factor) in the cable ($n \approx 15$) compared to strand ($n \approx 32$) is evidence of higher transverse resistance for current re-distribution. In the scaling law, the superconducting transition is sharp, with $n = \infty$, and a performance scaling with variable n-factor is not straight. The larger self-field in the cabled conductor also causes a broader transition in the E(I) and E(T) curves. It must be accounted in the design criteria that the J_c of the strand at a given criterion cannot be scaled to the same criterion in the large conductor just using the available scaling law, except for raw, first order guess.

The specification of the n-factor at the strand may be kept for generic quality assurance considerations, but has no impact on the actual n-factor of the cabled conductors.

The broad dc transition (common to all the cabled conductors) becomes an issue in the analysis of the results and in the modeling of the experiment. For thermohydraulic purposes, a smooth heat generation has been introduced in the code for analysis, by a n-power law. It is recommended always to implement this feature in the analysis and design codes.

The use and the definition of "current sharing temperature" and "critical current" must be carefully considered. Among the strand manufacturers, the electric field criterion of 10 μV/m is a solid, well-established reference. For practical cabled conductor in dc winding applications, the electric field criterion for $T_{cs}(B, I)$ should be set at the highest level sustainable in the winding, which depends on the operating current, the length of the high field section and the cooling rate. For example, in an ITER TF coil, with 60 kA and several meters per pancake exposed to the highest field, the criterion of 10 μV/m may be already too high for the CICC and 5 μV/m may be more appropriate.

The procedure to specify the strand J_c @ 10 μV/m from the T_{cs} requirement in the cabled conductor must be refined.

The issues of the n-factor in the cabled conductors and the definition of a T_{cs} threshold for windings have a large impact on the specification for the temperature margin in the design criteria. For example, the allowable highest temperature to estimate the energy margin (upper limit for the coolant enthalpy) may be much higher than T_{cs}, depending on the conductor length affected by the disturbance. For a local disturbance, a very large energy margin exists even at $\Delta T = T_{cs} - T_{op} = 0$.

The Coupling Loss Results

Despite the accuracy issue for the calorimetric measurement of the hysteresis loss, the assessment of the coupling currents loss in the range of 2 to 9 Hz is reliable. The high field coupling loss is very low, with $n\tau$ in the range of 1-1.5 ms, increasing up to $\approx$ 2.5 ms with J_{op} = 400 A/mm^2. The coupling loss is also estimated for the 15 Hz, single shot field transient. The result is about 30% smaller, in the range of 1.7 ms and has poorer accuracy compared to the 2-9 Hz steady state results. The loss decrease at higher frequency may be the effect of early screening.

The SeCRETS results agree with the three ac losses test in the ITER full size conductors in SULTAN, as well as the coil test of US-DPC and DPC-EX, all of them reporting coupling currents loss in the range of 2-5 ms. The overall picture suggests that the coupling loss in operation for Nb_3Sn, Cr plated cable-in-conduit is restricted to the interfilament loss.

This conclusion is contradicted by the short sample test at University of Twente and the CSMC coil test. The level of coupling loss from the UT test of ITER conductors under transversal load is in the range of 30 ms, measured at low frequency range, $f < 0.1$ Hz. In the CSMC, a broad range of results is quoted, from 50 to 200 ms. A way to solve the contradiction with the UT results may be to test the conductors over a broader range of frequency. A non-linearity of the loss curve, due to multiple time constants in the pattern of the strand bundle, may be the reason of different loss at different range of time scale.

Whatever the low frequency ac loss is, the excellent tolerance of transverse field transient is evidence that the coupling loss under the most crucial conditions (plasma disruption) is really very low. The transverse resistance by the Cr plating at the strand surface cuts the interstrand loss to the level of the intefilament loss. A lower interstrand resistance, e.g. by a thinner Cr plating, would be tolerable for coupling loss. Additional resistive barrier (e.g. subcable wraps) are not necessary for coupling loss reduction.

In the conductor with segregated copper the coupling loss is restricted to the superconducting strand volume. The loops of the coupling current do not close through the segregated copper.

Plasma Disruption

The field transient from plasma disruption has been applied to the SeCRETS conductor with the same shape, amplitude and time scale. The minimum temperature margin required to withstand the transient was below the operating range, i.e. < 0.3 K. This is fully consistent with the low level of coupling loss. To scale the result to a large coil, the definition of temperature margin must be adjusted according to the T_{cs} criterion (see dc results) and the conductor length affected by the transient must also be considered.

Anyway, as long as the transient coupling loss has $n\tau$ in the range of few ms and the field integral of the plasma disruption is in the range of few T^2/s with time scale of several hundred ms, the loss remains in the range of < 20 mJ/cm^3 and the required temperature margin on top of the operating temperature will stay < 0.1 K.

The margin to be allocated for plasma disruption is marginal and it is not a driving design criterion. The margin for plasma disruption is easily buried into the engineering margin, e.g. uncertainty for actual operating temperature, scattering of strand performance, etc.

Transient Stability

To investigate the transient stability, the test range has been extended into an area not relevant for fusion conductors. Very large transverse field transients, with $\int (dB/dt)^2 dt$ in the range of several hundreds T^2/s, are withstood with temperature margin smaller than 1 K. This impressive results is due partly to the low level of coupling loss and partly to the fact that the local temperature is allowed to grow above T_{cs} (see dc results) without starting a runaway.

The most conservative way to extrapolate the results is to consider a coil with very long conductor length in the highest field and a disturbance extended over the whole high field section. In this case the runaway temperature can be approximated to T_{cs}, the available enthalpy is only up to T_{cs} and the stability curve must cross the 0. After shifting the experimental stability curves, $\int (dB/dt)^2 dt$ vs. ΔT, to cross the 0, the ability to withstand field transient is still in the range of 15 T^2/s for 0.1 K temperature margin.

In the investigated range of disturbance duration (65 ms), the transient stability is a linear function of the mass flow rate, i.e. the coolant speed. With increasing Reynolds number, the boundary layer becomes thinner and the steady state heat transfer coefficient, which increases almost linearly with the coolant speed, dominates the ability to remove heat from the strand surface. The assumption that the turbulence induced by the heat removal

dominates the heat transfer coefficient has not been verified either by the experimental results or the simulations. Whenever the transient stability is an issue (probably not for the fusion conductors), the heat transfer coefficient, h, should not be fixed to an arbitrary value.

The stability, measured as a function of the operating current, did not show the inflection expected from the limiting current calculated at constant h = 1000 W/m^{2}K. The reason is that, at the selected operating conditions, the limiting current was likely higher than the critical current, as the heat transfer coefficient was actually much higher than 1000 W/m^{2}K. This apparently trivial finding has important implications for the ITER design, where the conductor layout (the amount of copper to be included in the superconducting strand) is driven by the criterion of $I_{lim} > I_{op}$. The question arises about the rationale to maintain the limiting current criterion with constant h = 1000 W/m^{2}K in the ITER conductor design. On one side the limiting current plays a role only for severe transient disturbances, which do not occur in fusion conductors. On the other hand, the limiting current value is proportional to $\sqrt{h}$, which varies broadly over the range of operating conditions.

An analysis of the results in terms of "deposited energy" shows that, within the accuracy of the procedure, the fraction of coolant enthalpy actually exploited for stability is larger at small temperature margin. This trend is also confirmed by computer simulations.

The stability comparison between short (32 ms) and long (65 ms) transients is complicated by the overlapping of pulsed and background field. The trend of the experimental results is not fully reproduced by the simulations (still in progress), where the modeling of the heat transfer coefficient does not reflect the time modulation of the deposited energy.

Current Distribution

From the analysis of the Hall sensors results, no major unbalance has been observed in the current distribution over the cable cross section, either next to the joint or at high field. Higher accuracy of the self field measurements is desirable. In the current sharing region, a small, but measurable displacement of the current centerline is observed, due to the field gradient over the cross section.

A small (1-2%), slow evolution of the Hall signal after a current ramp (transition from inductive to resistive current distribution) is observed barely above the accuracy of the measurements.

No propagation of coupling currents outside the pulsed field region has been observed, consistently with the conclusion that no relevant interstrand coupling currents occur. The fast transients also did not change the current distribution pattern.

Segregated Copper

The performance of conductors with and without segregated copper is identical as far as dc, ac losses, plasma disruption and current distribution. In extreme transient stability, far away from the fusion conductor operating range, the conductor without segregated copper has better performance. The high interstrand resistance prevents an effective current sharing among the segregated copper and the superconducting strands. Nonetheless, the Cu:non-Cu = 1 in the strands of the conductor with segregated copper is adequate to provide a stable operation, in opposition to the present design criteria for limiting current using h = 1000 W/m^{2}K.

The reduction of Cu:non-Cu ratio down to 1 is a viable, cost effective option for the Nb_3Sn ITER conductors. With the present level of interstrand resistance, the segregated copper has only a role for quench protection. Decreasing the interstrand resistance by a factor of 5 (e.g. by a thinner Cr plating) may allow to promote the segregated copper as effective stabilizer and further decrease the Cu:non-Cu ratio in the Nb_3Sn strands.

More Test on SeCRETS Conductors

To extend the range of results on SeCRETS conductors, two short samples are prepared for test in SULTAN in the first half of 2001. Among others, the following tests will be carried out to complete the database collected with the present report:

- AC losses by calorimetry and magnetization over a frequency range from 0.02 to 5 Hz, with pulsed field winding thermally de-coupled from the sample.
- Transient stability with pulsed field perpendicular to the sample *and* to the background field, with temperature margin down to 0.1 K.
- Stability vs. operating current up to 20 kA (J_{op} up to 800 A/mm^2) with variable limiting current (by varying the mass flow rate).
- DC behavior (V-I characteristic) for artificially controlled current distribution by cutting strands and variable distance between damage point and high field

Acknowledgement

The SeCRETS task is the result of the joined effort of the CRPP team. The drawer of this report is specially indebted to the professionals involved at different stages of the work, including Alexander Anghel, Albert Fuchs, Claudio Marinucci, Boris Stepanov. The technical staff of the CRPP, led by Martin Vogel, was in charge for the assembly and instrumentation of the sample, including Eric Binder, Thomas Gloor, Christian Kägi, Walter Pfister, Felix Roth. The operation of the SULTAN facility was responsibility of Martin Böhler and Pascal Erismann. The continuous support and involvement of team head, Georg Vècsey, has been essential.

The friendly collaboration with the subcontractors has been a key for the success of the task: Alexander Shikov and Alexandra Vorobieva (VNIINM, Moscow) for the Nb_3Sn strands, Victor Sytnikov (VNIIKP, Moscow) for cabling and jacketing, Bernard Oswald and Thorsten Strasser (OSWALD, Miltenberg) for the winding work, Arend Nijhuis and Niels Noordman (Univ. of Twente, Enschede) for the pulsed field coils.

The participation of scientists outside CRPP has crucially contributed in several areas to the results analysis: Arend Nijhuis and Yuri Ilyin (Univ. of Twente, Enschede) for the careful analysis of the current distribution (see also the separate EFDA report), as well as for strand and ac losses measurements, Werner Specking for the $I_c(\varepsilon)$ test at FzK, Karlsruhe, Elena Zapretilina (ITER-JCT, Naka) for the analysis of the dc results, Luca Bottura (CERN, Geneva) for the assistance with the computer simulations. The support of EFDA-CSU (Garching) and ITER-JCT (Naka) is acknowledged. The discussion and comments raised at the SeCRETS workshop in Morschach (September 2000) have also contributed to the present form of the report

Pierluigi Bruzzone

Appendix

Assumptions and methods for computer simulations

Generalities

The main features of the model used in Gandalf are described in Refs. [A.1, A.2, A.3]. The model is 1-D, and for the simulation of the SeCRETS experiment three components have been defined: the superconducting strands, the helium and the conductor jacket. The temperature is homogeneous in the cross section of the components, and can vary only along the length. Heat can be deposited in the strand cross section homogeneously.

Reference input data

The simulated conductor is 2 m long and its center (at X = 1m, where X is the one-dimensional coordinate) coincides with the center of the 30 cm heated zone. In both the conductors A and B the non-copper cross sections include the correction due to conductor twisting whereas in the conductor B the copper cross section does not include the segregated copper. The insulation is not included in the model. The heat transfer perimeter at the contact surface of the strand and bundle is the geometric value, i.e. it is not reduced by a factor 5/6. The friction in the bundle is characterized by the Katheder correlation. The extrapolated values of the helium pressure at the location of the pulsed coils (average of inlet and outlet pressure), as well as the measured mass flow rate, are given as hydraulic boundary conditions. The static mesh includes a total of 200 nodes whereas the minimum and maximum time steps are 1.0^{-6} and 1.0^{-5}, respectively. The first order method in space and time is applied for the integration. The reference input-data are given in the tables below.

Gandalf input parameters for SeCRETS

Input parameter	Symbol	Unit	Conductor	
			A	B
Hydraulic length	XLENGT	m	2.0	
Code for non-copper material data	ISC	-	-103	-104
Non-copper cross section	ASC	mm^2	30.238	29.893
Longitudinal strain at I_{op}= 12kA and B = 9.71T	EPSLON	-	-7.24977E-3	-6.35023E-3
Longitudinal strain, function of I_{op} at B = 9.71T	EPSLON	-	Next Table	Next Table
Copper cross section	AST	mm^2	45.358	29.893a
Copper RRR	RRR	-	107	95
Code for jacket material data	IJK	-	13	
Jacket cross section (AISI 316L)	AJK	mm^2	46.372	
Code for insulation material data	IIN	-	22	
Insulation cross section	AIN	mm^2	0.0	
Helium cross section (hole)	AHEH	mm^2	0.0	
Helium cross section (bundle)	AHEB	mm^2	44.074	44.513
Hydraulic diameter (hole)	DHH	mm	0.0	
Hydraulic diameter (bundle)	DHB	mm	0.47283	0.51233
Bundle void fraction	VOID	%	36.8296	37.1966
Heat transfer perimeter helium-conductor (bundle)	PHTC	m	0.37285	0.29164
Heat transfer perimeter helium-jacket	PHTJ	mm	0.29084E-1	
Heat transfer perimeter conductor-jacket	PHTCJ	mm	0.96947E-2	
Heat transfer perimeter hole-bundle	PHTHB	mm	0.0	
Perforation fraction of hole wall	PERFOR	%	0.0	
Critical temperature at zero magnetic field	TC0M	K	17.30	17.70
Upper critical magnetic field at zero temperature	BC20M	T	32.65	32.80
Fitting constant for critical current surface	C0	$AT0.5/m^2$	7.750E-9	7.515E-9
Cos(theta)	-	-	0.9840	0.9893

a Segregated copper not included

Other conductor data:

Friction factor of bundle (Katheder): $f_B = (0.25/VOID0.72)*(0.051+(19.5/Re0.88)$ where Re is the Reynolds number and VOID is the bundle void fraction.

Longitudinal strain as a function of the operating current at B = 9.71 T

Iop (A)	Conductor A		Conductor B	
	EPSLONa (-)	Tcs (K)	EPSLONb (-)	Tcs (K)
5000	-6.98740E-3	8.6928	-6.61260E-3	9.0369
6000	-7.02488E-3	8.3547	-6.57512E-3	8.7209
7000	-7.06236E-3	8.0317	-6.53764E-3	8.4212
8000	-7.09984E-3	7.7196	-6.50016E-3	8.1333
9000	-7.13733E-3	7.4155	-6.46267E-3	7.8543
10000	-7.17481E-3	7.1168	-6.42519E-3	7.5819
11000	-7.21229E-3	6.8219	-6.38771E-3	7.3143
12000	-7.24977E-3	6.5290	-6.35023E-3	7.0499
13000	-7.28725E-3	6.2368	-6.31275E-3	6.7875
a EPSLON = -0.68E-2 - 3.86E-9 * I_{op} * B b EPSLON = -0.68E-2 + 3.86E-9 * I_{op} * B				

Magnetic field and heat modulation

A sinusoidal modulation of the magnetic field is superimposed to the constant background field during the heating of duration tauq (either 0.065 or 0.032 ms), i.e. $B=(\Delta B/2)\sin(2*\pi*t/tauq)$ and $B=\Delta B\sin(\pi*t/tauq)$ for full wave and half wave heating, respectively. The heat deposited into the strands at the 0.3 m heated zone is modulated by a wave form proportional to the cosine squared.

J_c and T_{cs} fitting

The Summer coefficients from the above tables are used in the standard ITER routines to determine the Nb_3Sn properties. The deduced values of current sharing temperature and longitudinal strain (see above) match the experimental results.

Joule heat and current sharing model

The Joule heat term depends on the current carried by the cable component I_i and on the electric field E_i developed along its length. In general terms we can write that:

$$\dot{q}'_{Joule,i} = I_i E_i \qquad \text{(A.1)}$$

where, for consistency with the 1-D approximation made so far, we assume that current and electric field have the same direction. In the case of a purely resistive material there is a linear relation between the electric field and current density in the material:

$$E_i = \eta_i J_i \tag{A.2}$$

where η_i is the average electrical resistivity of the component and J_i the current density defined as:

$$J_i = \frac{I_i}{A_i} \tag{A.3}.$$

For a component containing a superconducting material in parallel with a stabilizing shunt the relation is more complex. The electric field in a superconducting strand or cable is fitted using a power law:

$$E_i = E_0 \left(\frac{I_i}{I_c} \right)^n \tag{A.4}.$$

The constant E_0 is the electric field set as the criterion to define the critical current I_c.

To obtain a general expression for the Joule heat dissipation in the composite component containing a superconductor we distinguish the superconducting cross section A_{sc} from the other (stabilizing) materials, with a total cross section A_{st}. For these last we define an equivalent resistivity η_{st}. The total current in the component I_i splits in a part through the superconductor I_{sc} and a part in the stabilizer $I_{st} = I_i - I_{sc}$ such that the longitudinal electric field in both components is identical. The split itself depends on the non-linear voltage-current relation for the superconductor, which could be different from Eq. (A.4) as the measurements used to establish it contain the contributions of both superconductor and stabilizer to the longitudinal voltage. In principle a relation of the type of Eq. (A.4) can be obtained from measurements for the superconductor only, correcting for the current sharing in the stabilizer. However it can be shown that in the range of E_0 and n parameters given above the current flowing in the stabilizer is small. Therefore we can safely assume that Eq. (A.4) is valid for the superconductor alone, substituting the total current in the component with the current in the superconductor, i.e.:

$$E_i = E_0 \left(\frac{I_{sc}}{I_c} \right)^n \tag{A.5}.$$

The longitudinal voltage equality in the superconductor and in the stabilizer can be therefore written as follows:

$$\eta_{st}\frac{I_i - I_{sc}}{A_{st}} = E_0\left(\frac{I_{sc}}{I_c}\right)^n \qquad \text{(A.6).}$$

Equation (A.6) is solved by an iterative technique to obtain I_{sc}. The longitudinal electric field is then readily obtained using Eq. (A.5), and the total Joule heat dissipation is given by Eq. (A.1). In the SeCRETS simulation the values assumed for n and E_0 are

$E_0 = 1.0^{-4}\ V/m$

$n = 15$

Heat transfer coefficient

The components (strands, jacket, helium) are thermally coupled through convection on wetted surfaces (or contact perimeters) p with a surface heat transfer coefficient h. The mutual heat exchange coefficients have been defined as follows:

$$h_{St,He} = h_{He} \qquad \text{(A.7)}$$

$$h_{Ja,He} = h_{He} \qquad \text{(A.8)}$$

$$h_{St,Ja} = 500 \qquad \text{(A.9)}$$

where h_{He} is the heat transfer coefficient to the flowing helium stream, and the heat transfer coefficient among jacket and strands has been taken as a constant. The heat transfer coefficient of the helium stream has been defined using the following expressions:

$$h_{He} = max\{h_{Ks}, h_{Kt}\} \qquad \text{(A.10)}$$

$$h_{Kt} = \frac{h_K h_t}{h_K + h_t} \qquad \text{(A.11)}$$

$$h_{Ks} = \frac{h_K h_{ss}}{h_K + h_{ss}} \qquad \text{(A.12)}$$

$$h_K = 200(T_{St} + T_{He})(T_{St}^2 + T_{He}^2) \qquad \text{(A.13)}$$

$$h_t = \sqrt{\frac{K\rho C_p}{\pi t}} \qquad \text{(A.14)}$$

$$h_{SS} = Nu\frac{K}{D_h} \qquad \text{(A.15)}$$

$$N = max\{0.023\,Re^{0.8}\,Pr^{0.4}, 8.235\} \qquad \text{(A.16)}$$

where K is the thermal conductivity of helium, ρ is its density, C_p is the specific heat at constant pressure and D_h is the hydraulic diameter. In the series of expressions above h_K is the heat transfer coefficient corresponding to the Kapitza resistance at the solid-helium interface, h_t is the heat transfer coefficient equivalent to the filling of a helium boundary

layer following a pulse in the pipe wall temperature, and h_{SS} is the heat transfer coefficient equivalent to the heat resistance of the boudnary layer for a steady state turbulent flow, with a lower laminar limit defined in terms of the Nusselt number.

To derive the equivalent h_{He} it is assumed that the Kapitza heat resistance (i.e. h_K) is in series with either the transient or the steady state heat resistance of the boundary layer. This results in two equivalent heat transfer coefficients h_{Kt} and h_{Ks} for transient and steady state conditions respectively. Switching from transient to steady state conditions corresponds to the achievement of a steady state temperature profile in the boundary layer, and is simulated taking the largest of either h_{Kt} or h_{Ks}.

The above approximation is simplified with respect to reality. During the experiment the heat flux from the strand to the helium is a strong function of time, and thus the assumption of constant temperature of the strand that is used for the calculation of the h_t fails. To give an order of magnitude of the expected variation of the heat transfer coefficient we have performed a simulation of the temperature evolution in an ideal boundary layer with constant thermophysical properties K=0.020 W/mK, r=140 Kg/m^{-3}, C_p=3500 J/Kg·K, and a constant thickness of 25 μm. One side of the boundary layer is bounded by the solid wall at variable temperature and/or heat flux condition, while the other side is kept at the bulk helium temperature. The effective heat transfer coefficient is defined as the ratio of the heat flux at the wall and the temperature difference between wall and helium. The following conditions have been examined:

- step in the wall temperature;
- step in the wall heat flux;
- $\cos^2(t)$ variation of the wall heat flux (i.e. simulating the heat deposition in the experiment).

The results of this simulation are reported in Fig. A.1. The approximation as would be generated in gandalf is reported for comparison. The approximation used for the stability simulation with gandalf is a rough average of the most realistic result from the third case above. It is clear however that the evolution of the equivalent heat transfer coefficient during the transient can be significant, and the approximation used in the gandalf simulation is not satisfactory for the description of fine details.

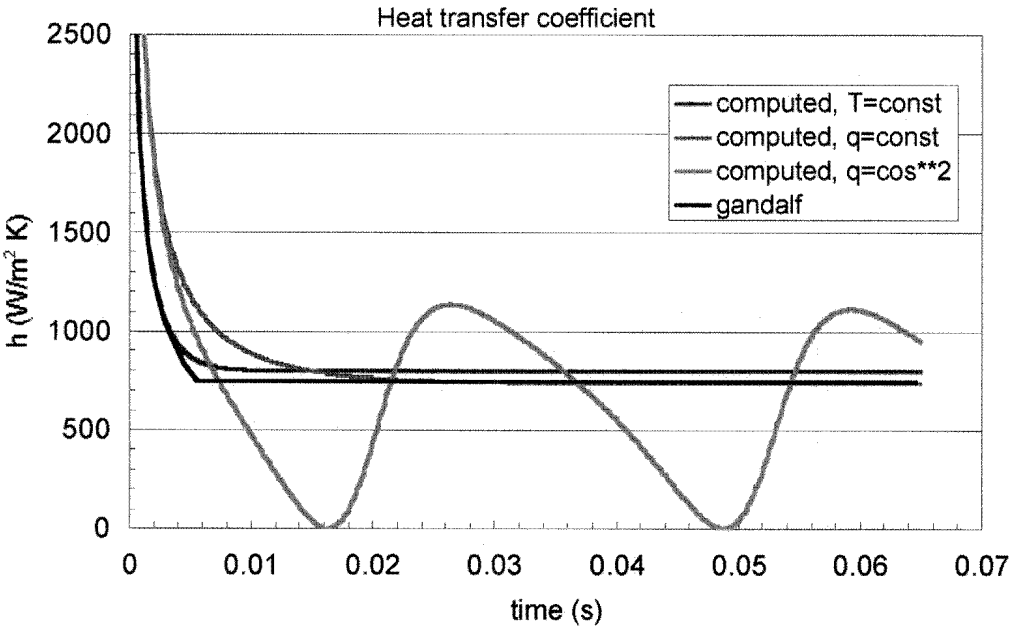

Figure A.1. Simulation of heat transfer in a helium boundary layer with constant thickness of 25 μm, constant thermophysical properties K=0.020 W/mK, ρ=140 Kg/m³, C_p=3500 J/Kg K and subjected to a step in the wall temperature, a step in the heat flux at the wall, and a time variable heat flux at the wall with a $\cos^2(t)$ dependence.

References

[A.1] L.Bottura, *A Numerical Model for the Simulation of Quench in the ITER Magnets*, Jour. Comp. Phys., **124**, (1), 1996.

[A.2] L. Bottura, *Modelling Stability in Superconducting Cables*, Physica C, **310**, 316-326, 1998.

[A.3] CryoSoft, *GANDALF. A computer code for quench analysisof dual flow CICC's*, Version 2.1, 2000.